ABSTRACT

Name: Xiaofei Song

Department: Physics

Title: The Search for Second Generation Leptoquarks at Run II DØ in the $\mu\mu jj$ Channel in $\sqrt{s}$=1.96 TeV $p\bar{p}$ Collisions

Major: Physics

Degree: Doctor of Philosophy

Approved by:

Date:

Dissertation Director

NORTHERN ILLINOIS UNIVERSITY

ABSTRACT

A search for second generation leptoquarks in $p\bar{p}$ collisions at the Fermilab Tevatron is presented using DØ data with an integrated luminosity of 370 pb^{-1} collected in Run II between September 2002 and August 2004 at a center of mass energy of $\sqrt{s}$=1.96 TeV. Leptoquarks are assumed to be pair produced, and each decays into a muon and a quark with a branching ratio of β. The number of events in data after the selection cuts is consistent with the expected Standard Model background. No evidence for leptoquark production is found; a lower limit of 247 GeV (NN based), 236 GeV (cut based) for $\beta = 1$ and 184 GeV (NN based), 174 GeV (cut based) for $\beta = 1/2$ on the leptoquark mass at the 95% confidence level is obtained.

NORTHERN ILLINOIS UNIVERSITY

THE SEARCH FOR SECOND GENERATION LEPTOQUARKS AT RUN II DØ IN THE $\mu\mu jj$ CHANNEL IN $\sqrt{s}$=1.96 TeV $p\bar{p}$ COLLISIONS

A DISSERTATION SUBMITTED TO THE GRADUATE SCHOOL
IN PARTIAL FULFILLMENT OF THE REQUIREMENTS
FOR THE DEGREE
DOCTOR OF PHILOSOPHY

DEPARTMENT OF PHYSICS

BY
XIAOFEI SONG

DEKALB, ILLINOIS
DECEMBER 2005

Certification: In accordance with departmental and Graduate School policies, this dissertation is accepted in partial fulfillment of degree requirements

Dissertation Director

Date

ACKNOWLEDGMENTS

DØ collaboration is a huge family, in which thousands of people from all over the world work together toward the same goal. It was impossible for me to finish this study without their hard work. I would like to thank all the people whose efforts have made this thesis come to fruition.

Throughout the years of my Ph.D. study, Dr. Pushpa Bhat, Dr. David Hedin, and Dr. Thomas Nunnemann were always willing to mentor, encourage and support me. Their expertise and enthusiasm in the field of high energy physics, as well as their unique insightful way of approaching problems, have been among my most valuable resources.

To all the members of the NIU DØ group, who have provided advice and comments on my analysis, thank you! I would like to thank several individuals – Gerald Blazey, Arthur Maciel, Vishnu Zutshi, Mike Eads, Sergey Uzunyan and Andriy Zatserklyaniy – for helping me in a multitude of ways.

In general, the comments and direction I received from the New Phenomena group at DØ have been a great help. I would like to thank all the people in the DØ NP group. Furthermore, I would like to thank Dr. Volker Buescher and Jean-Francois Grivaz for giving me a lot of valuable comments.

I appreciate the help provided by Dr. Herman Haggerty, Dr. Albert Ito, Dr. Dmitri Denisov, and Professor Huishun Mao, who taught me about DØ hardware.

Finally, I would like to acknowledge the U. S. Department of Education and the National Science Foundation for their financial support.

To my beloved wife Yaohui, and my son Yang and daughter Amy

TABLE OF CONTENTS

Chapter Page

Chapter Page

Chapter Page

LIST OF TABLES

LIST OF FIGURES

Figure Page

CHAPTER 1

THE STANDARD MODEL AND BEYOND

"What is the world made of? What is the smallest possible piece of matter? What are the fundamental forces of nature?" Over and over, in different ages and with different methods, people have tried to answer these questions.

The idea that the world was constructed out of small units of matter received a great boost in the late 19th century when the periodic table of the elements was established in 1872 by D. I. Mendeleev [1]. Then with the discovery of the electron by J. J. Thompson [2] in 1897, the atomic structure was determined. In 1911 Rutherford [3] made his famous α scattering experiment and found that the atom is composed of a nucleus with the electrons in orbitals around it. Later on, the discovery of protons and neutrons made it clear that the nucleus was not indivisible and hence not elementary, but was composed of two particles: the proton and neutron bound together to form the nucleus.

The advent of particle physics as a distinct field to discover the most basic building blocks of nature began in the middle of the last century. In the following decades, physicists discovered more and more particles with the help of particle accelerators, that led to the establishment of the Standard Model.

1.1 The Standard Model

The *Standard Model* [4] is a theoretical framework that describes matter particles (the elementary building blocks - quarks and leptons) and the force carriers (gauge bosons) and fundamental interactions amongst them. It is a local gauge invariant relativistic quantum field theory based on the $SU(3)_C \otimes SU(2)_L \otimes U(1)_Y$ symmetry group, where "C" refers to the color charge, "L" to the isospin and "Y" the weak hypercharge.

1.1.1 Elementary Particles in the Standard Model

The particles in the Standard Model can be categorized into two groups based on their spins - the spin 1/2 fundamental fermions obey Fermi-Dirac statistics and spin 1 gauge vector bosons obey Bose-Einstein statistics. The fundamental fermions are subdivided into two parallel classes called *leptons* and *quarks*. Experiments have demonstrated that there are six leptons and six quarks. The lepton family consists of *electron* (e), *electron neutrino* (ν_e), *muon* (μ), *muon neutrino* (ν_μ), *tau* (τ) and *tau neutrino* (ν_τ), while the quark family consists of *up* (u), *down* (d), *charm* (c), *strange* (s), *top* (t), and *bottom* (b). The quarks have an additional degree of freedom called *color* charge; each quark may exist in one of three possible color states, *red* (r), *green* (g) or *blue* (b). Both quark and lepton classes have three generations and are grouped into three sets of doublets.

$$\mathbf{Q}uarks = \begin{pmatrix} u \\ d \end{pmatrix} \begin{pmatrix} c \\ s \end{pmatrix} \begin{pmatrix} t \\ b \end{pmatrix} \quad \mathbf{L}eptons = \begin{pmatrix} \nu_e \\ e \end{pmatrix} \begin{pmatrix} \nu_\mu \\ \mu \end{pmatrix} \begin{pmatrix} \nu_\tau \\ \tau \end{pmatrix} \tag{1.1}$$

Figure 1.1 shows the Standard Model elementary particles. Tables 1.1 and 1.2 list the properties of the fundamental fermions of the Standard Model. Each particle

in the table also has an associated anti-particle, therefore, there are 24 fermions in total.

Table 1.1

The Standard Model leptons

Generation	Particle Name	Symbol	Mass (MeV/c^2)	Charge (e)
1	Electron	e	0.511	-1
	Electron Neutrino	ν_e	< 3 eV	0
2	Muon	μ	106	-1
	Muon Neutrino	ν_μ	< 0.19	0
3	Tau	τ	1777	-1
	Tau Neutrino	ν_τ	< 18.2	0

Table 1.2

The Standard Model quarks

Generation	Particle Name	Symbol	Mass	Charge (e)
1	up	u	$1.5 \sim 4$ MeV	$2/3$
	down	d	$4 \sim 8$ MeV	$-1/3$
2	charm	c	$1.15 \sim 1.35$ GeV	$2/3$
	strange	s	$80 \sim 130$ MeV	$-1/3$
3	top	t	174 ± 5 GeV	$2/3$
	bottom	b	$4.1 \sim 4.4$ GeV	$-1/3$

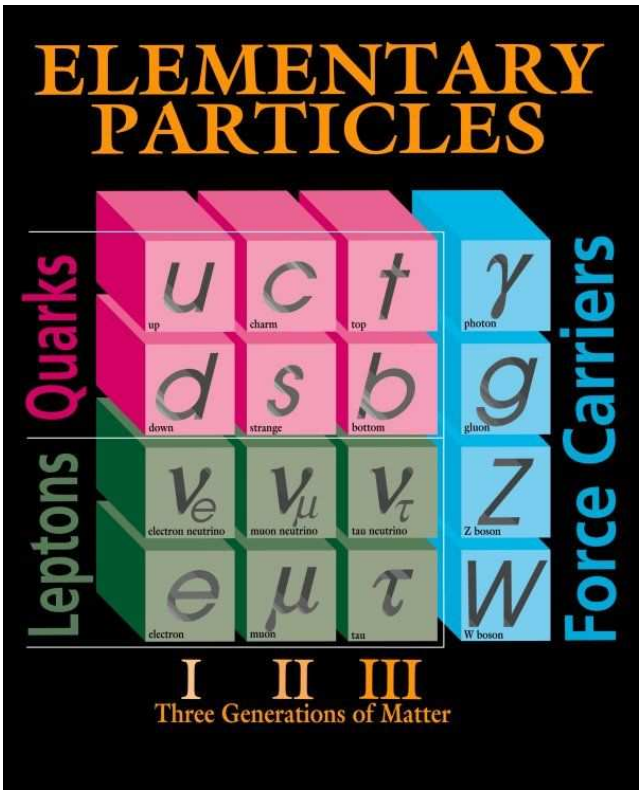

Figure 1.1. Standard Model elementary particles.

1.1.2 The Interactions Between the Elementary Particles

The interactions between the elementary particles are mediated by the gauge vector bosons. As mentioned before, the gauge transformations, which are responsible for the interactions between the elementary particles, follow the group structure $SU(3)_C \otimes SU(2)_L \otimes U(1)_Y$. Three foundmental forces for elementary particle interaction are incorporated into the Standard Model. They are the strong, electromagnetic, and weak forces. The fourth physical force, gravity, is not contained in the framework of the Standard Model. The $SU(3)_C$ component of the group structure describes the strong interactions which bind quarks together. Strong interactions within the Standard Model are mediated by massless particles called gluons. $SU(2)_L$

is the weak isospin group which is responsible for the weak nuclear interactions mediated by $W^{\pm}$ and Z bosons. $U(1)_Y$ is the hypercharge group; at low energies, the $SU(2)_L \otimes U(1)_Y$ symmetry is broken into $U(1)_{em}$ group describing the electromagnetic interactions whose gauge boson is the massless photon. Table 1.3 lists the properties of the Standard Model interactions and the gauge boson mediators.

Table 1.3

The Standard Model elementary interactions

Force	Carrier	Strength	Range	Mass (GeV)	Charge (e)	Spin
Strong	Gluon (g)	1	10^{-13}	0	0	1
EM	Photon (γ)	10^{-2}	infinite	0	0	1
Weak	$W^{\pm}$	10^{-6}	10^{-16}	80.4	± 1	1
	Z^0			91.2	0	1

The electroweak sector of the Standard Model is a gauge theory that unites the weak and electromagnetic interaction. The gauge group $SU(2)_L \otimes U(1)_Y$ requires 4 massless gauge vector bosons. However, in order to describe weak interaction phenomenology, it is required that the vector bosons mediating the weak force acquire a non-zero mass. This is accomplished through the process of spontaneous symmetry breaking [5], which is implemented via the Higgs Mechanism [6]. The Higgs Mechanism requires the introduction of complex scalar fields. By allowing the scalar field to acquire a non-zero value, 3 of the 4 gauge vector bosons acquire non-zero mass and are identified with the $W^{\pm}$, Z^0. The remaining massless gauge vector boson is identified with the photon γ. The remaining neutral scalar field, called the *Higgs* field, is associated with the Higgs boson. However, the Higgs boson has not been experimentally observed yet, and will be searched for at the Fermilab Tevatron and the Large Hadron Collider at CERN.

1.2 Beyond the Standard Model

The Standard Model has been proven to be a remarkably successful theory. It has been tested repeatedly and found to be in good agreement with experimental evidence. One striking example is the prediction of the W and Z bosons as well as their masses, which were experimentally verified by the UA1 and UA2 Collaboration at CERN in 1983 [7]. Another example of the success of the Standard Model is the prediction of the existence of the top quark, which was experimentally discovered by the DØ and CDF collaborations at Fermilab in the mid-1990s [8]. But despite all its success, the Standard Model is unlikely to be the final theory. Perhaps the most obvious flaw with the Standard Model is that it does not include gravity, which governs our daily life. The gravitational interaction is sufficiently weak that it plays no role in fundamental particle interactions. Nonetheless, a theory which does not include all the four forces of physics is not likely to be a fundamental theory. Most physicists believe that the four forces are just different aspects of a single unified force at sufficiently high energy scale. Also, the Standard Model is an *ad hoc* choice of the gauge groups and particle multiplets; it contains no explanation for the apparent symmetry between the quark and lepton sectors (*i.e.* the similarity between the family and generation structure shown in Figure 1.1, Table 1.1 and 1.2). There are also many arbitary parameters included in the Standard Model by hand. These issues and unsolved questions make physicists believe that a new theory is required which goes beyond the Standard Model, and motivates, for example, the existence of hypothesized leptoquarks.

1.2.1 Grand Unified Theories (GUT)

Grand Unified Theories [9] propose a single interaction to describe the electromagnetic, weak, and strong interactions with a unique intrinsic coupling at some

unification energy $M_{GUT} \approx 10^{16}$ GeV. GUT theories treat the Standard Model gauge symmetry group $SU(3)_C \otimes SU(2)_L \otimes U(1)_Y$ as a sub-group, and predict transitions between quarks and leptons.

1.2.2 Supersymmetry

The most popular theories beyond the Standard Model are supersymmetric theories called *SUSY* [10] which postulate a relation between the bosons and the fermions in the Standard Model. Each Standard Model particle has a supersymmetric partner refered to as a sparticle with spin differing by 1/2, but with the other quantum number being the same. Thus the Standard Model bosons have superpartner fermions and the Standard Model fermions acquire superpartner bosons. In its R-parity violating models, the superpartners of quarks might possess leptoquark-like decay modes [11].

1.3 Thesis Overview

The fact that the Standard Model contains no further explanation for the observed symmetry between lepton and quark families motivates the existence of the leptoquarks. This thesis describes details of the search for the scalar second generation leptoquarks in the dimuon channel. Chapter 2 gives an overview of the leptoquark theory and phenomenology. Chapter 3 outlines the experimental apparatus used to perform the analysis. Chapter 4 describes the event reconstruction at DØ. Chapter 5 and 6 discuss muon and jet reconstruction in more detail. Chapter 7 will go over the search for the scalar second generation leptoquarks. Conclusions and summary are given in Chapter 8. In this analysis, it is assumed that $\hbar = c = 1$; thus all mass, momentum, and energy variables will be expressed in units of GeV.

CHAPTER 2

INTRODUCTION TO LEPTOQUARKS

The Standard Model has been proven repeatedly to be in good agreement with the experimental evidence. However, to the apparent symmetry between quark and lepton sectors, i.e., the similarity between the family and generational structure shown in Figure 1.1 and Tables 1.1, and 1.2, the Standard Model gives no further explanation. There is no explanation within the Standard Model framework for the number of generations. The existence of such a symmetry motivates a possible relation between quark and lepton families of fundamental particles at the fundamental level. Many Standard Model extensions attempt to incorporate this symmetry and predict the existence of some kind of leptoquarks [12].

2.1 Leptoquarks in Standard Model Extensions

Leptoquarks are hypothetical particles that carry both lepton and baryon quantum numbers, couple to both leptons and quarks and offer a possible explanation for the observed symmetry between quark and lepton sectors. Particles carrying both lepton and baryon quantum numbers are not allowed within the framework of the Standard Model, thus any search for the leptoquarks is necessarily a search beyond the Standard model. Leptoquarks are color triplet bosons under $SU(3)_C$, could be either scalar (spin=0) or vector (spin=1), and can carry fractional electric charge. In models where lepton and baryon numbers are separately conserved, leptoquarks

could have masses of the order of the electricweak scale ($m_W \approx 80$ GeV) and still avoid conflict with proton decay results [13]. Depending on the particular model, leptoquarks may have spin 0, 1, or 2; isospin 0, $\frac{1}{2}$ or 1; electric charge $-\frac{4}{3}$, $-\frac{1}{3}$, $\frac{2}{3}$ or $\frac{5}{3}$; baryon number $\pm\frac{1}{3}$ and lepton number ± 1.

2.1.1 Leptoquarks in Grand Unified Theory

The aim of Grand Unified Theories is to find a super gauge group to describe all known Standard Model interactions with a single coupling constant. In Grand Unified Theories, a leptoquark induces the transformation of a quark into a lepton, resulting in a strong similarity between the leptons and the quarks as a naturally arising consequence of the unification. One of its models, $SO(10)$ GUT model, provides complete unification with one universal coupling constant. Its maximal breaking pattern, $SO(10) \rightarrow SU(4)_C \otimes SU(2)_L \otimes SU(2)_R$, leading to the Pati-Salam GUT model [14] which treats the lepton sector as a fourth color, predicts the existence of leptoquarks which carry both lepton and baryon quantum numbers. Another interesting GUT model is Superstring Inspired E_6 [15]. The Superstring Inspired E_6 model contains a large number of particles in addition to those present in the Standard Model: superpartners of the Standard Model fermions and gauge bosons, scalor leptoquarks, extended gauge and Higgs bosons and new exotic quarks and leptons [15, 16].

2.1.2 Leptoquarks in Supersymmetry

SUSY model breaking can be divided into two categories, conserving or violating R-parity, where R is defined as $R = (-1)^{3B+L+2S}$, B, L are the baryon and lepton numbers, and S denotes the spin of the particles. The Standard Model particles have R=+1, and R=-1 is assigned to their superpartners. If R-parity is required,

supersymmetric particles could only be created in pairs of a SUSY particle and a SUSY antiparticle, while in R-parity violating models, squarks might possess leptoquark-like decay modes through Yukawa coupling.

2.2 Leptoquark Production and Decay

In $p\bar{p}$ collisions at the Fermilab Tevatron, leptoquarks can be produced either singly or in pairs. The cross-section for single production is model-dependent and relies on the size of the unknown Yukawa coupling of the leptoquark. Pair production, which proceeds through QCD interactions, depends only on the leptoquark spin and on the fact that it is a color triplet field and will be the dominant production mechanism in $p\bar{p}$ collisions [17].

Michael Krämer et al. [18] have provided a tool to calculate the leading order and next-to-leading order cross section for the pair production of scalar leptoquarks of arbitrary mass at the certer-of-mass $\sqrt{s} = 1.96$ TeV. The results are used to translate the cross section limit, determined in this analysis, into the lower mass limit of the scalar leptoquarks. Figure 2.1 shows leptoquark pair production cross section as a function of the leptoquark mass in $p\bar{p}$ collisions at the certer-of-mass $\sqrt{s} = 1.96$ TeV, Figure 2.2 and 2.3 show the leading order and next-to-leading order Feymann diagrams for pair production of leptoquarks in $p\bar{p}$ collisions, and Figure 2.4 gives an example Feymann diagram for the single leptoquark production via t-channel.

Leptoquarks with universal coupling to all leptons and quarks will give rise to flavor-changing neutral currents and therefore are severely constrained [19]. By assuming that there are three distinct generations of leptoquarks and each leptoquark couples only to the corresponding generation of quarks and leptons, experimental constraints can be satisfied without requiring large leptoquark mass. Under these

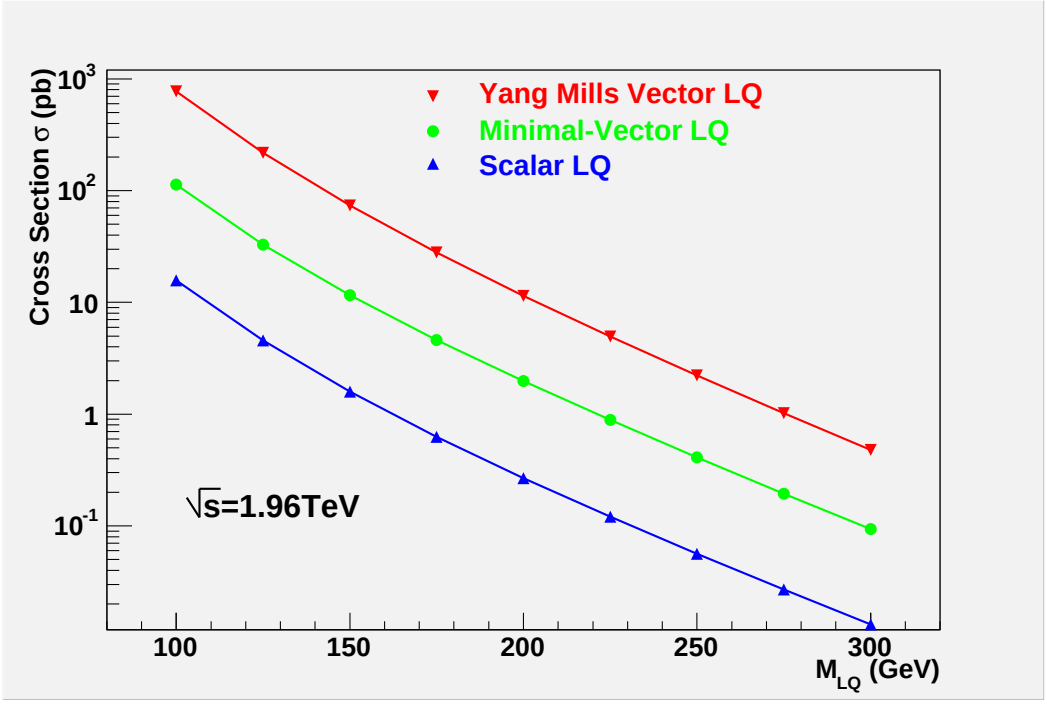

Figure 2.1. Leptoquark pair production cross section as a function of the leptoquark mass in $p\bar{p}$ collisions at the center-of-mass energy of $\sqrt{s} = 1.96$ TeV.

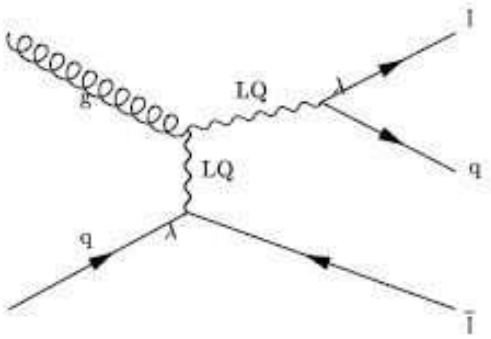

Figure 2.2. Example of single leptoquark production via t-channel in $p\bar{p}$ collisions.

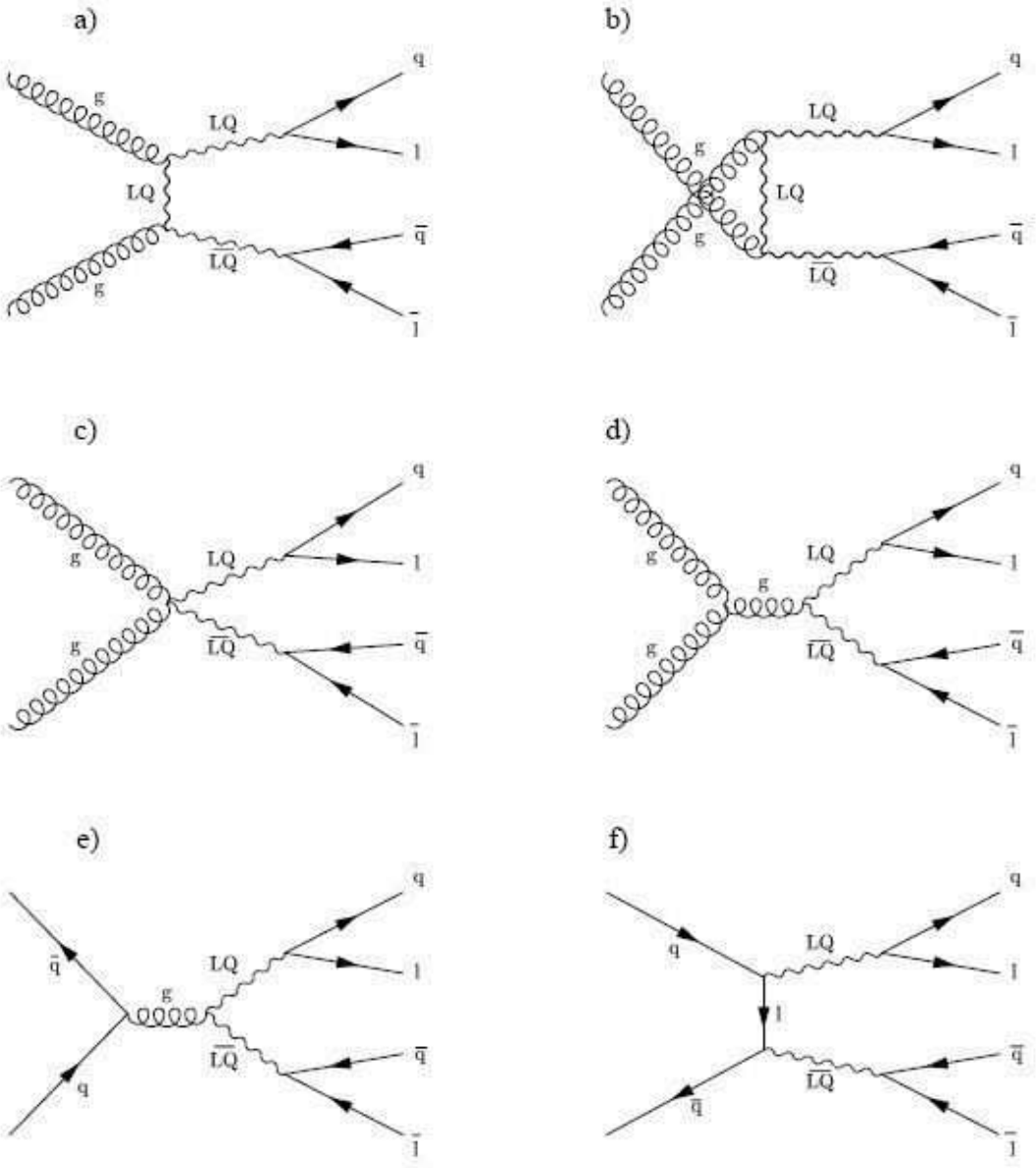

Figure 2.3. Leading order Feymann diagrams for leptoquark pair production in $p\bar{p}$ collisions: a)-d) gluon-gluon "fusion", e) quark-antiquark annihilation, f) pair production via LQ-q-l vertices.

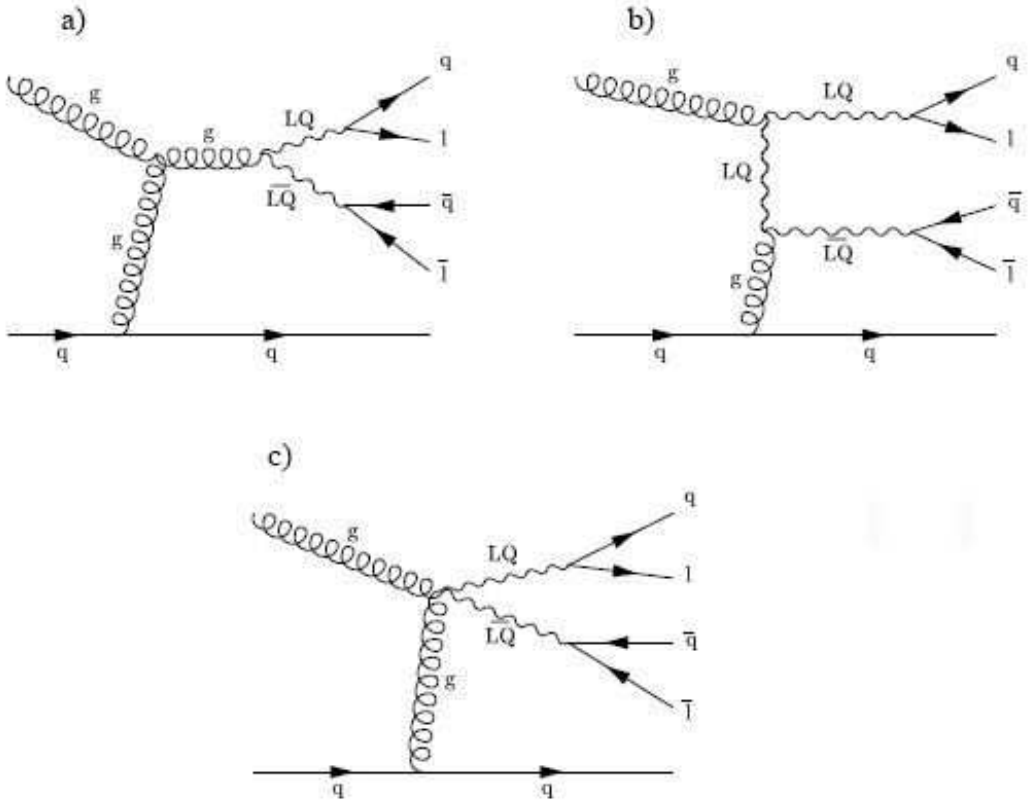

Figure 2.4. Examples of next-to-leading order Feymann diagrams for leptoquark pair production in gluon-quark subprocess in $p\bar{p}$ collisions.

conditions, the decays of leptoquark pairs would be expected to yield one of three possible final states: $l^+l^-q\bar{q}$, $l^{\pm}\nu q\bar{q}$ and $\nu\bar{\nu}q\bar{q}$. If the branching ratio of a leptoquark decaying into a charged lepton and a quark is defined as β, then the decay fractions of a leptoquark pair in the $l^+l^-q\bar{q}$, $l^{\pm}\nu q\bar{q}$ and $\nu\bar{\nu}q\bar{q}$ final states are β^2, $2\beta(1-\beta)$ and $(1-\beta^2)$, respectively. In this analysis, a search for the scalar second generation leptoquark with the final states of $\mu^+\mu^-q\bar{q}$ is presented.

2.3 Run I Experimental Results

Much theoretical and experimental work has been done since the first prediction of leptoquarks. Although direct searches for leptoquarks were also performed in e^+e^- collisions, the stringent limits come from $p\bar{p}$ and $e^{\pm}p$ collider experiments. At the Fermilab Tevatron, all three generation leptoquarks have been searched by both DØ and CDF experiments during Run I [11, 20, 21, 22]. Table 2.1 lists the previous mass limits for all three generation leptoquarks.

Table 2.1

Run I mass limits for all three generation scalar and vector leptoquarks in $p\bar{p}$ collisions at $\sqrt{s} = 1.8$ TeV

Generation (1, 2, 3)	β Br(LQ$\rightarrow l^{\pm}q$)	Scalar LQ (GeV)	Vector LQ (GeV)	
			Minimal	Yang-Mills
1	1	225	292	345
	1/2	204	282	337
	0	98	238	298
2	1	202	275	325
	1/2	180	260	310
	0	98	238	298
3	1	99	170	225
	0	94	148	216

CHAPTER 3

FERMILAB, TEVATRON, AND DØ

Fermilab, originally named the National Accelerator Laboratory, located about 50 km west of Chicago, was founded in 1967. It is a US Department of Energy Laboratory and is operated by the Universities Research Association (URA) since its founding. In 1974, the laboratory was renamed in honor of Nobel Prize-winning physicist Enrico Fermi [23]. Figure 3.1 shows an aerial view of the Fermilab Tevatron Accelerator Complex.

Fermilab has played an important role in the field of high energy physics since it was founded. Two major components of the Standard Model fundamental particles and forces were discovered at Fermilab: the bottom quark (May-June 1977) and the top quark (February 1995). In July 2000, Fermilab experimenters announced the first direct observation of the tau neutrino, the last fundamental fermion to be observed [24].

3.1 The Fermilab Tevatron Accelerator Complex

The Fermilab Tevatron, six kilometers in circumference, is the world's highest-energy particle accelerator [25]. It delivers proton and anti-proton beams each with energies of 0.98 TeV. The accelerated protons and anti-protons, moving in opposite directions in the synchrotron ring, collide with a center-of-mass energy of 1.96 TeV. The collisions take place at the two interaction regions of BØ and DØ which are

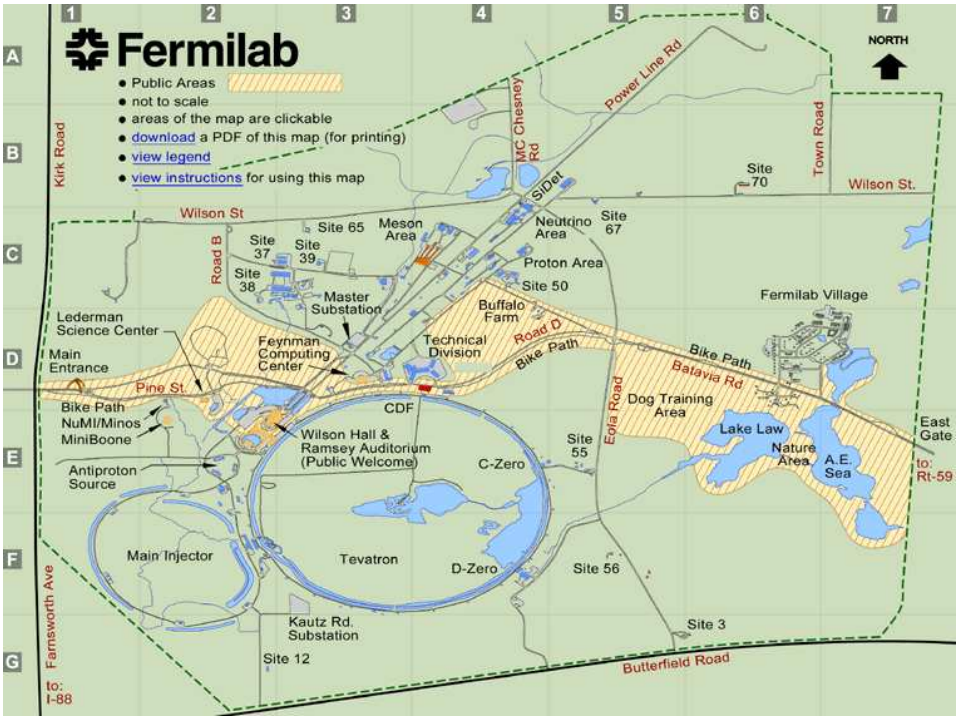

Figure 3.1. Schematic of the aerial view of the Fermilab Complex near Chicago.

surrounded by the CDF and DØ detectors, respectively.

In general, collision experiments take place in three different steps: the initial production and injection of the particles, followed by chains of successive acceleration and finally the collisions. Figure 3.2 shows a schematic diagram of the Fermilab Tevatron Accelerator Complex.

3.1.1 The Preaccelerator

The accelerating processes begin with the preaccelerator. The hydrogen gas is released into a magnetron surface-plasma source. An electric field produced by the magnetron strips off the electron from the hydrogen atom. The free protons are then attracted to the cathode, where they collect electrons and are subsequently disengaged by the stream of bombarding atoms. If the released protons happen to

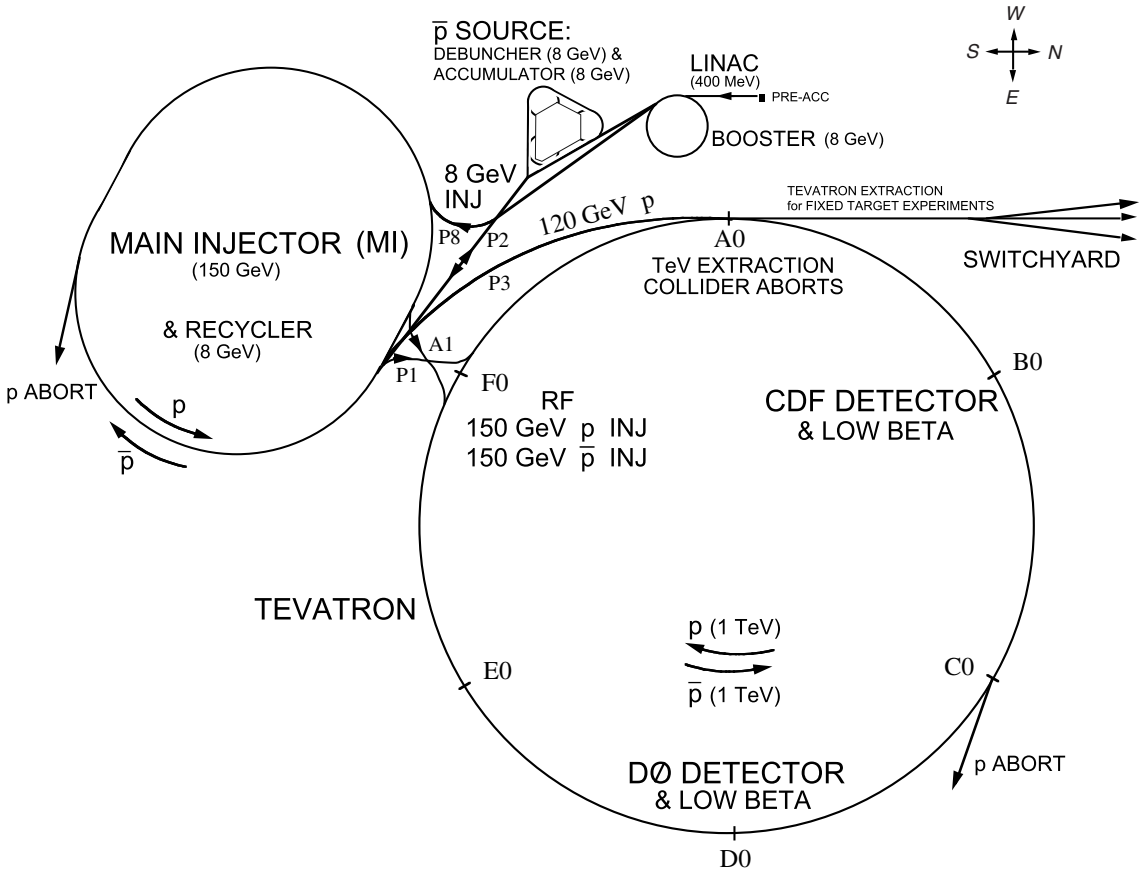

Figure 3.2. Schematic diagram of the Fermilab Tevatron accelerator complex.

capture two electrons, they become H^- ions and a magnetic field causes them to spiral out the opposite side of the magnetron source. An extractor plate accelerates the ions to a kinetic energy of 18 keV, and then the ions are further accelerated by a electrostatic Cockroft-Walton accelerator to an energy of 750 keV.

3.1.2 The Linac

The next stage of acceleration is performed by the Linac, a linear accelerator, illustrated in Figure 3.3. The H^- ions are injected into a 150-meter-long Linac accelerator by an electric field; they then enter a shielded region, meanwhile the polarity of the electric field is reversed to prevent more ions from entering, thus

creating a localized bunch of ions. Upon exiting the shielded region the electric field is reversed again, giving the ions another boost of acceleration. This is done several times over a 150-meter-long distance, and the ions are accelerated to the energies of 400 MeV. After leaving the Linac, a debuncher is applied to the H^- ion beams to reduce momentum spread, then the electrons of the H^- ions are stripped off by passing through a thin carbon foil, and the protons are injected into the Booster.

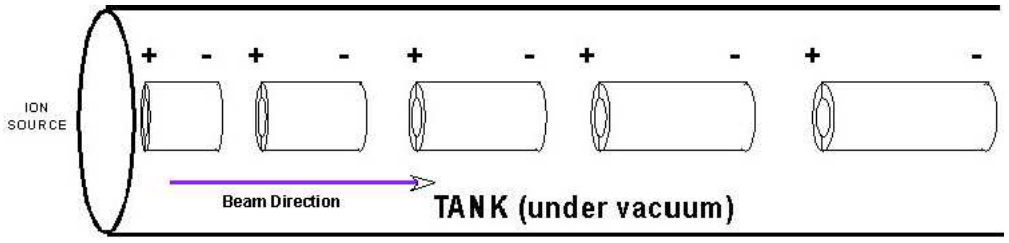

Figure 3.3. Illustration of the 150-meter-long Linac of the Fermilab Trvatron.

3.1.3 The Booster Synchrotron

The Booster is a 150-meter-diameter synchrotron. The protons coming from the Linac are constrained to a circular orbit by bending magnets. Quadrapole focusing fields from the magnets keep the beam from diverging. A set of radio frequency (RF) cavities steadily increases the momentum of the proton beam as it revolves around the ring. To maintain the same circular orbit with increasing beam momentum, both the RF frequency and the magnetic field strength are increased in a synchronous manner. The proton beam is injected into the Main Injector after it attains an energy of 8 GeV.

3.1.4 The Main Injector

The Main Injector is a rapid cycling synchrotron with a 3 kilometer circumference. It receives the 8 GeV proton beam from the Booster, accelerates and delivers it to the Tevatron with the energy of 150 GeV while simultaneously delivering a 120 GeV proton beam to the anti-proton facility, for the production of anti-protons. After a sufficient number of anti-proton are produced, stored and cooled, the Main Injector is used to accelerate both protons and anti-protons to 150 GeV and then inject them into the Tevatron, for collider stores.

3.1.5 The Anti-proton Source

Anti-protons are produced by bombarding a stainless steel target with a 120 GeV proton beam extracted from the Main Injector. The secondary particles from the proton interactions with the target nuclei contain anti-protons. Immediately downstream from the stainless steel target is a lithium collection lens, which produces an azimuthal magnetic field to focus the anti-protons. An illustration of the setup used is shown in Figure 3.4. Following the collection lens is a pulsed dipole magnet that selects 8 GeV anti-protons out of the secondary particles and transports them to the Debuncher.

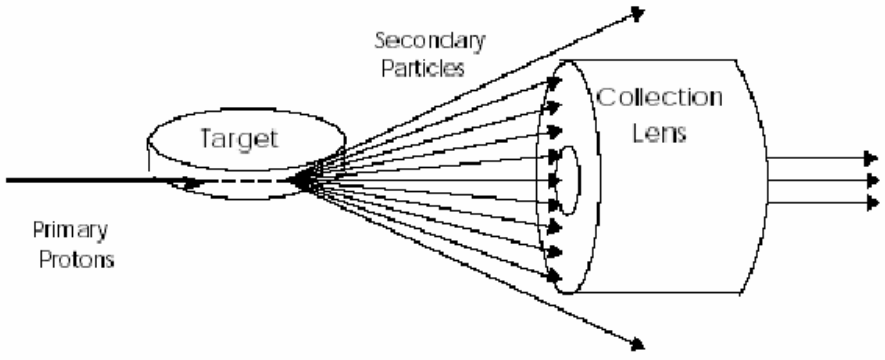

Figure 3.4. An illustration of the anti-proton production and collection.

3.1.6 The Debuncher and Accumulator

The Debuncher is an 8 GeV storage ring in which the bunches of anti-protons are reduced in momentum spread and increased in longitudinal distance spread. Anti-protons from the Debuncher are transfered to the Accumulator, another 8 GeV storage ring, where they are cooled and accumulated. Once a sufficient amount of particles is collected in the Accumulator, the bunches are transfered to the Main Injector, which accelerates them to the energies of 150 GeV and delivers them to the Tevatron, where they move in the opposite direction to that of the protons.

3.1.7 The Tevatron

The Tevatron is a 6-kilometer-circumference synchrotron ring where the final stage of acceleration occurs. Using superconducting magnets, the 150 GeV proton and anti-proton beams delivered from the Main Injector are accelerated up to an energy of 980 GeV and collided at two regions surrounded by DØ and CDF detectors. The Tevatron is filled with 36×36 bunches of protons and anti-protons with a 396 ns collision interval. The collider stores may last for up to 20 hours. The initial peak luminosity of the stores has recently reached a record of $\sim 1.3\times10^{32}$ cm^{-2}sec^{-1}, and total integrated luminosity delivered, up to May 2005, reached $\sim$ 940 pb^{-1}.

3.2 The DØ Detector

The DØ detector [26] is a general purpose detector designed to detect all the possible interactions taking place in high energy p$\bar{\text{p}}$ collisions with a geometrical accepance of nearly the full solid angle of 4π. It weights 5500 tons and measures 17 (length) $\times$ 11 (width) $\times$ 13 (height) m^3. The initial operation started in 1992 with Run I of the Tevatron accelerator; approximately 100 pb^{-1} of p$\bar{\text{p}}$ collisions were recorded between 1993 and 1996, then the DØ detector went through a major up-

grade for Run II. The upgraded DØ detector consists of three primary sub-detector systems. From inner to outer are inner tracking system, calorimeter systems and muon systems. A schemetic view of the Run II DØ detector is shown in Figure 3.5. From inner to outer are the Inner Tracking system, Calorimeter system and Muon system.

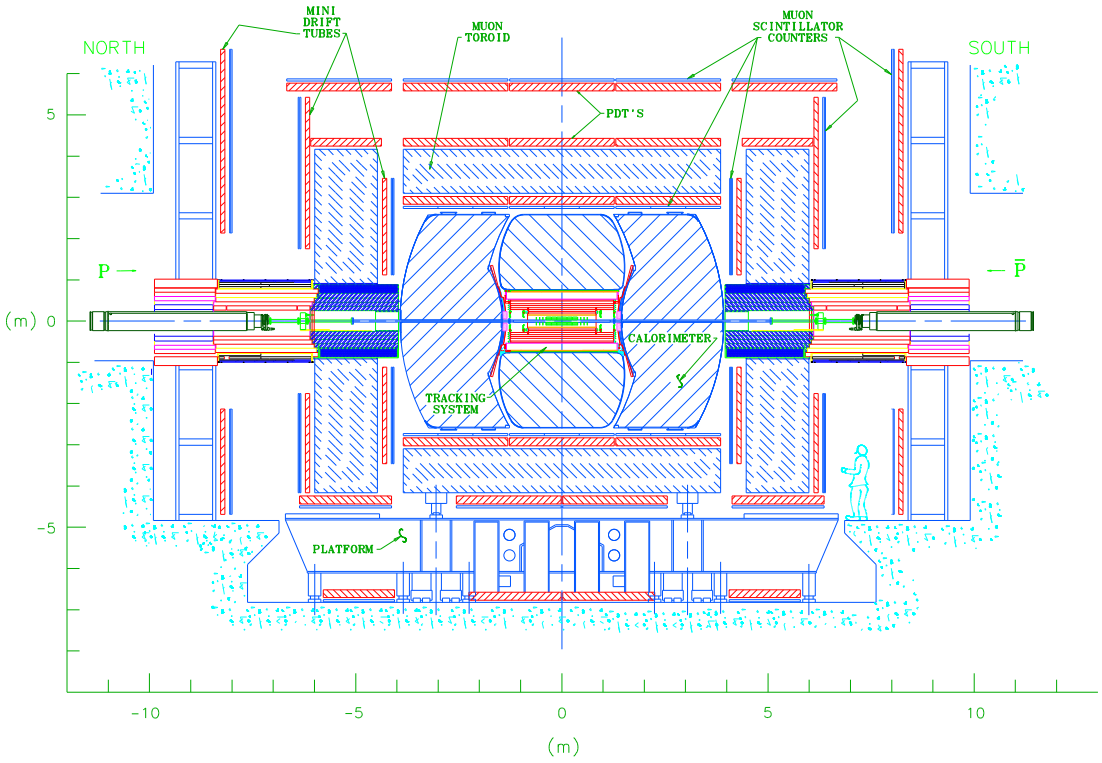

Figure 3.5. A schematic view of the Run II DØ detector as seen from the side.

3.2.1 The DØ Coordinate System

The Cartesian coordinate frame of DØ is defined with its origin at the nominal interaction point and the z axis coinciding with the proton beam, y axis pointing upwards, and the x axis pointing radially outward from the certer of the Tevatron ring determined by the right-hand rule. Based on the Cartesian coordinates, the azimuthal ϕ and the polar angle θ as well as the r coordinate of the spherical coordinates are also defined: r corresponds to the perpendicular distance from the

z axis, ϕ is the angle around the z axis with $\phi = 0$ being the x direction and θ is the angle from the z axis. In this analysis, the polar direction of particles is often related to η, the pseudo-rapidity, defined as

$$\eta = -\ln\left(\tan\frac{\theta}{2}\right) \tag{3.1}$$

which is an approximation of the rapidity y

$$y = \frac{1}{2}\ln\frac{E + p_z}{E - p_z} \tag{3.2}$$

in the limit that $m \ll E$, where E is the energy and m is the rest mass of the particle. Figure 3.6 shows the DØ coordinate system.

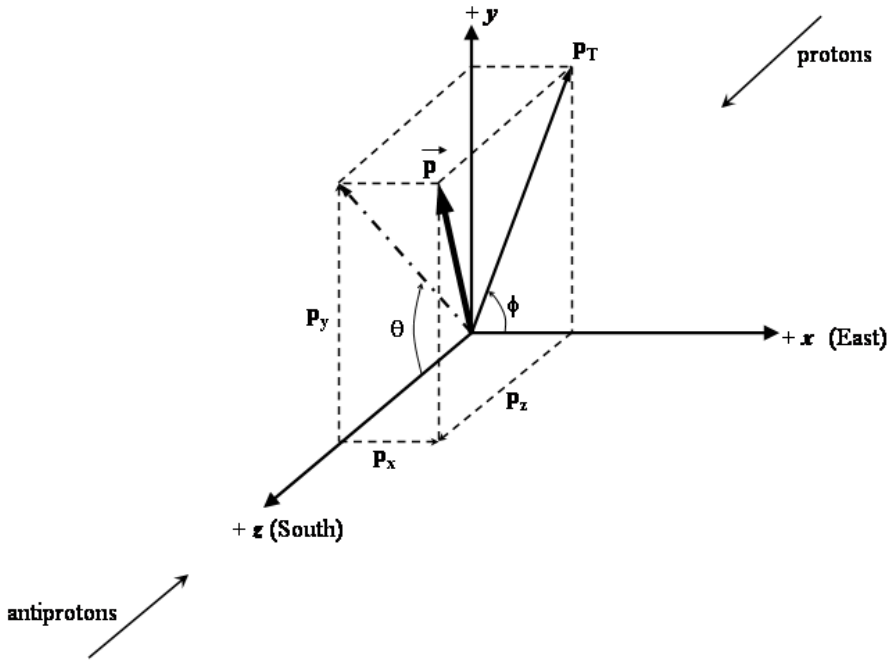

Figure 3.6. Illustration of DØ coordinate system and components of the momentum.

The commonly used kinematic variables are the transverse energy $E_T = E \sin\theta$ and the transverse momentum $p_T = p \sin\theta$. The motivation for using these quantities is because in $p\bar{p}$ collisions the center of mass energy is not fixed due to the parton structure of the nucleon being collided. The partons carry only a fraction of the total beam energy; thus the total energy balance cannot be used. However, the transverse energy balance can be used since it is known to be zero before the collision and the detectors are specifically built to measure nearly all of the transverse energy from the collision.

3.2.2 The Central Tracking System

The central tracking system consists of two subsystems: the Silicon Microstrip Tracker (SMT) [27] and the Central Fiber Tracker (CFT) [28]. Surrounding these subsystems is a superconducting solenoid magnet [29], which provides a field of 2 Tesla parallel to the beam direction. The goals of the tracking system are to reconstruct the trajectories of charged particles from the $p\bar{p}$ collisions. The central tracking system is an essential component to the search for a pair of secondary leptoquarks which decay into two highly energetic muons and two quarks. Figure 3.7 shows the DØ central tracking system which covers a large range in $|\eta| \leq 3$. From inner to outer are the Silicon Microstrip Tracker, the Central Fiber Tracker, and the Superconducting Solenoid Magnet.

3.2.2.1 The Silicon Microstrip Tracker

The innermost part of the tracking system, the Silicon Microstrip Tracker (SMT), is designed as a hybrid system consisting of *barrel* detectors measuring primary $r - \phi$ coordinates and *disk* detectors measuring $r - z$ coordinates as well as $r - \phi$ coordinates. This design geometry is motivated by the fact that the interaction point

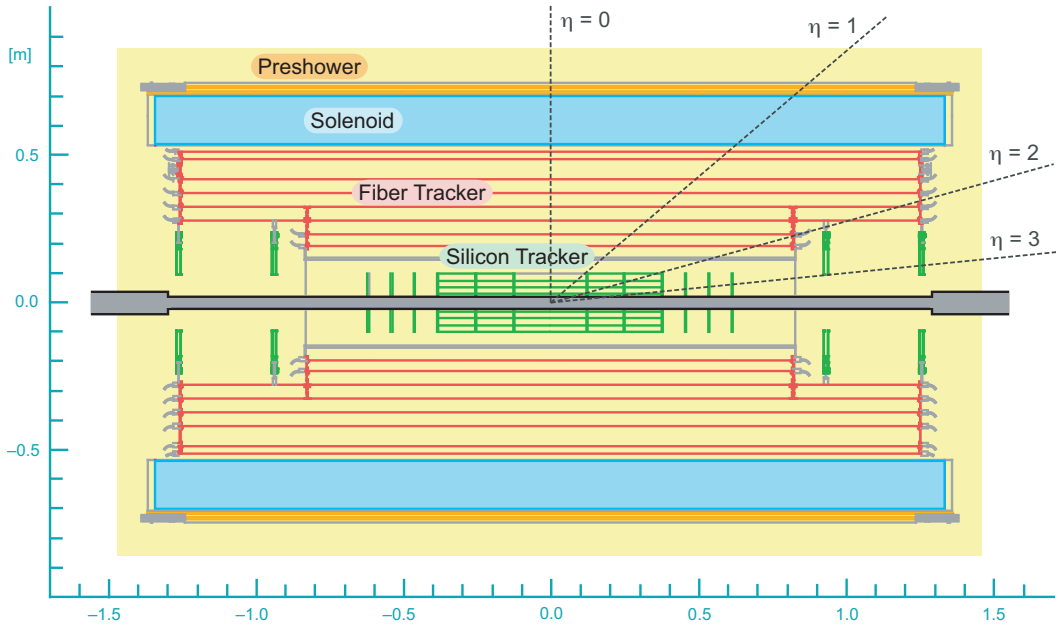

Figure 3.7. Side view of the DØ Central Tracking system. From inner to outer are the Silicon Microstrip Tracker, the Central Fiber Tracker, and the Superconducting Solenoid Magnet.

is distributed over the z coordinate with a $\sigma_z \approx 25$ cm. In this hybrid design, high η tracks are primarily reconstructed by the disks, while low η tracks are reconstructed by barrels. The Silicon Microstrip Tracker consists of six barrel modules where silicon sensors are parallel to the beam line, twelve small disks called "F-disks" and four large disks called "H-disks" where silicons sensors are normal to the beamline. Figure 3.8 gives a three-dimensional view of the Silicon Microstrip Tracker. Each barrel is 12 cm in length and consists of four concentric detector layers starting at a radius of 3 cm and extending out to a radius of 10 cm. Four of the F-disks are sandwiched in the four 8 mm gaps between barrel segments, and the remaining eight F-disks are symmetrically located on each side of the central barrels. The four H-disks are located at $|z| = 110$ and 120 cm. The SMT detector has approximately 800k electronic readout channels with a $r - \phi$ hit resolution of approxmately 10 μm.

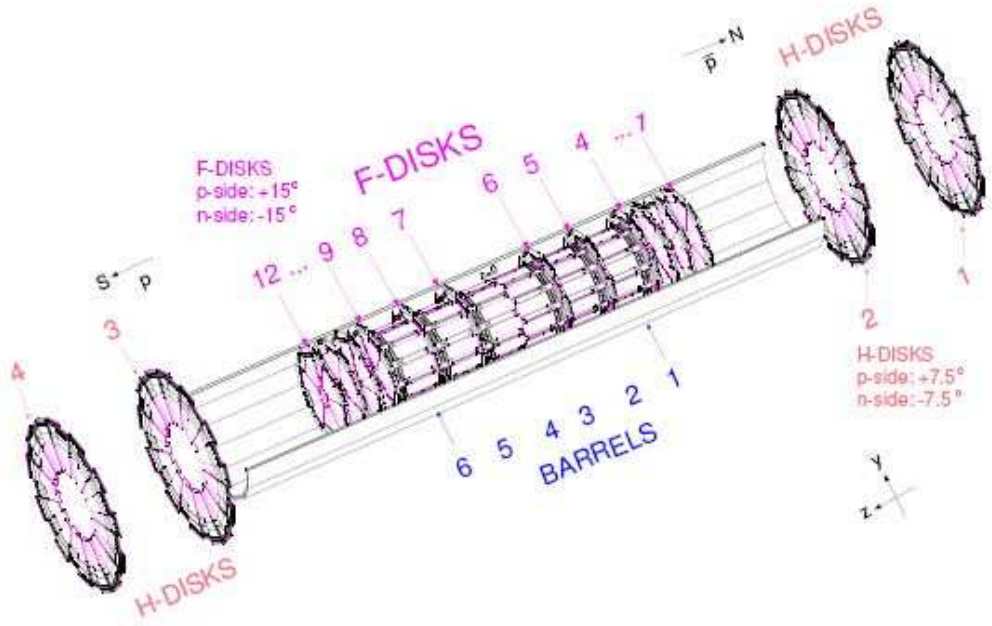

Figure 3.8. Three-dimensional view of the DØ Silicon Microstrip Tracker (SMT).

3.2.2.2 The Central Fiber Tracker

The Central Fiber Tracker (CFT) surrounds the Silicon Microstrip Tracker (SMT) in eight concentric cylinders and consists of about 77000 scintillating fibers at a distance from the z axis of between 20 cm and 51 cm. The inner two cylinders are 1.7 meters long while the outer six are 2.5 meters long. Differences in length accommodate the silicon H-disk detectors located at high η. Each cylinder is covered by two doublet layers of scintillating fibers. A double layer consists of two mono-layers of fibers placed together such that one mono-layer is offset by one half of the fiber spacing with respect to its partner. This configuration compensates for geometric gaps between adjacent fibers in a mono-layer and provides a detection efficient per doublet layer of nearly 100 percent. The inner doublet layer on each cylinder is mounted along the axial direction; on top of the axial layer another doublet layer is mounted at alternating u or v stereo angles of approxmately 3 degrees. From the

innermost to outermost barrel, the orientations for the layers follow the pattern of $xu{-}xv{-}xu{-}xv{-}xu{-}xv{-}xu{-}xv$. The geometrical acceptance of the Central Tracker Fiber reaches out into the forward direction up to $|\eta| \approx 1.5$. Figure 3.9 shows a view of the CFT as well as an illustration of the doublet layer configuration.

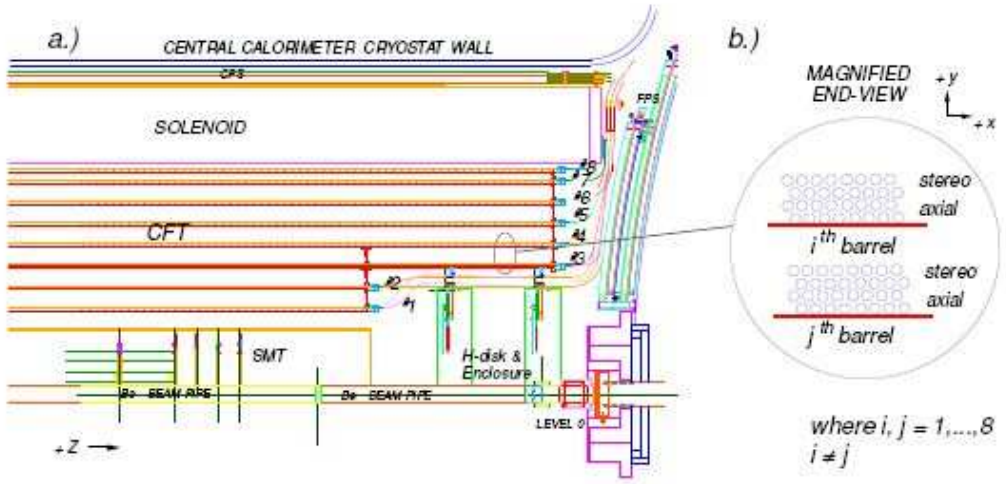

Figure 3.9. A quarter side view of the DØ Central Fiber Tracker (CFT) and doublet layer configuration.

When a charged particle travels through a fiber, the scintillator emits light which is internally reflected down the length of the fiber. The light is guided to a set of devices called Visible Light Photon Counters (VLPC), a silicon-avalanche based photon detector, where the scintillation light from the CFT is converted into an electrical signal and sent to front-end electronics for digitization and readout.

3.2.3 The Solenoid

Surrounding the central tracking system is a superconducting solenoid magnet which provides a magnetic field of 2 Tesla along the z axis. By measuring the curvature of a track, the central tracking system, i.e., the SMT and CFT together, can provide a momentum resolution of $\Delta p_T/(p_T)^2 = 0.002$ GeV^{-1} for highly energetic charged particles.

3.2.4 The Calorimeter System

One of the strengths of the DØ detector is its calorimeter system [26] due to its fine granularity and excellent coverage and uniformity. The calorimeter system measures the energy and position of incident particles and distinguishes particle types by their energy deposition patterns.

3.2.4.1 The Preshower Detectors

The preshower detectors, which are mounted to the outside of the magnetic solenoid, serve to enhance the electron and photon identification by providing an additional calorimetric measurement. The preshower detectors consist of the Central Preshower detectors (CPS) [30] and the Foward Preshower detectors (FPS) [31]. Their spatial resolution of 1-2 mm transverse to the particle direction helps to distinguish electron, photon, and pion showers and even allows a precise extrapolation of electro-magnetic showers back to the interaction region up to $|\eta| \approx 2.5$.

The Central Preshower detector, located in the 51 mm gap between the solenoid and the central calorimeter cryostat at a radius of 72 cm, consists of three layers of scintillating strips with wavelength-shifting (WLS) fiber readout, and covers the pseudorapidity region $|\eta| < 1.2$. The inner layer is an axially arranged layer, while the two outer layers are stereo layers (u and v layers) with stereo angles of

±23 degrees. Figure 3.11 shows the side and end view of the Central Preshower detector.

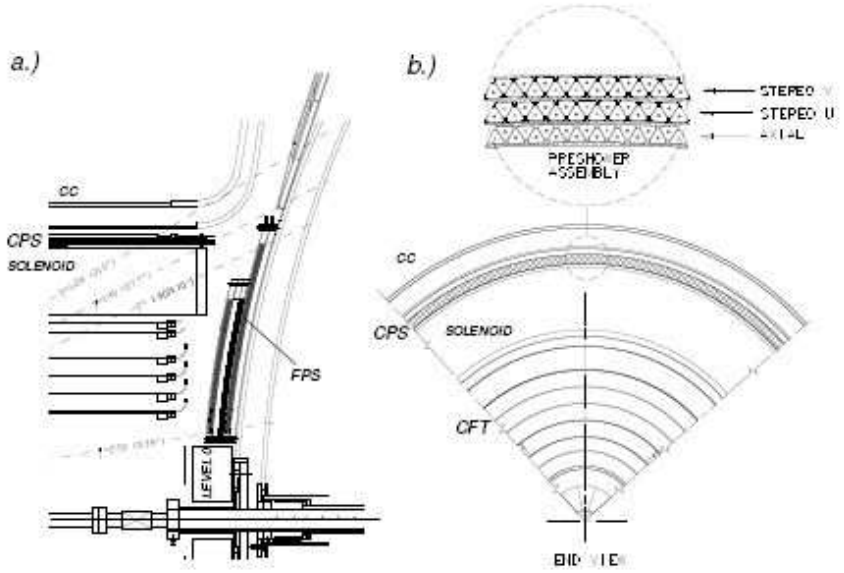

Figure 3.10. a) Semi-quarter side and b) End view of DØ Central Preshower detector (CPS).

The Forward Preshower detectors (FPS) consist of two domes mounted on the inner face of the end-cap calorimeter cryostat and cover the pseudorapidity range $1.5 < |\eta| < 2.5$. Similar to the CPS, the FPS utilizes two scintillation planes, with each plane consisting of one u and one v sub-layer, as shown in Figure 3.11.

3.2.4.2 The Calorimeter

The calorimeter system [32] of the DØ detector is comprised of successive layers of passive uranium and liquid argon. The central part of the calorimeter, located around the preshower and the solenoid, occupies the space between 75 - 222 cm in radial direction from the center of the beam pipe. Together with the forward calorimeter system, the calorimeter system covers the pseudorapidity η up to 4.0. Figure 3.12 shows a schematic cut view of the DØ calorimeter system.

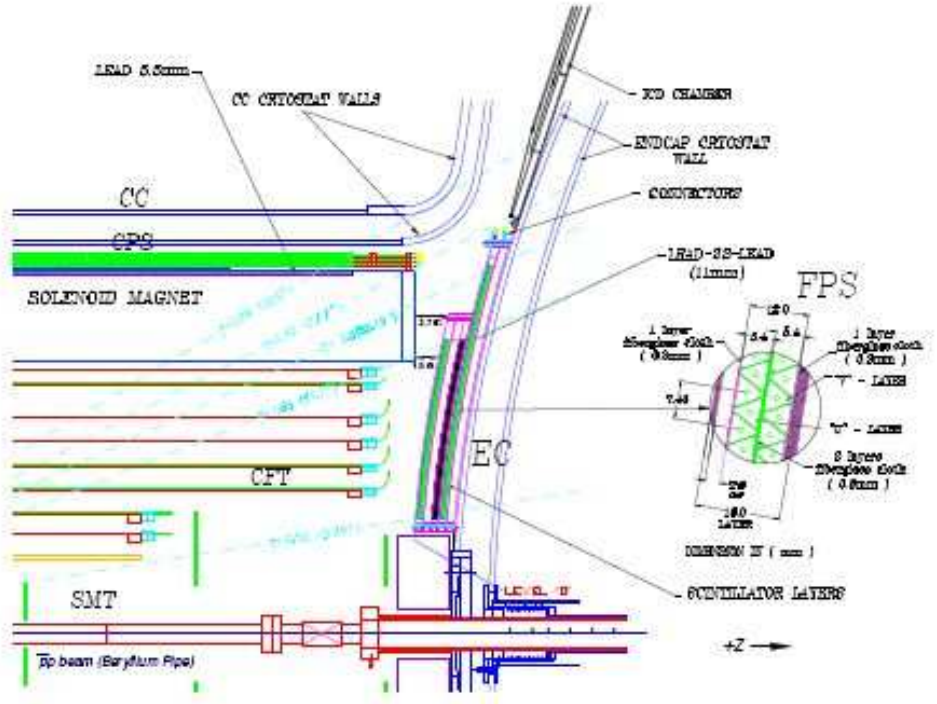

Figure 3.11. Quarter side view of DØ Forward Preshower detector (FPS) and the u v scintillator layers.

The calorimeter measures energy and position of electromagnetic (electrons, photons) and hadronic (pions, jets) objects, and provides the identification of these objects by utilizing the different shower patterns they create in the calorimeter. Eletromagnetic (EM) objects interact primaiily with the uranium via $\gamma \rightarrow e^+e^-$ and $e \rightarrow e\gamma$ processes. For each successive interaction the number of secondary particles increases while the average energy per particle decreases exponentially according to $E(x) = E_0 e^{x/X_0}$ until the energies are exhausted, E_0 is the original energy of the particle, x is the distance traveled and X_0 is the radiation length of the material being passed through. On the other hand, hadronic objects interact with uranium through inelastic collisions. The interactions produce secondary hadron, which in turn undergo inelastic collisions. The process will continue until all particles have either been stopped by ionization losses or absorbed by nuclear processes.

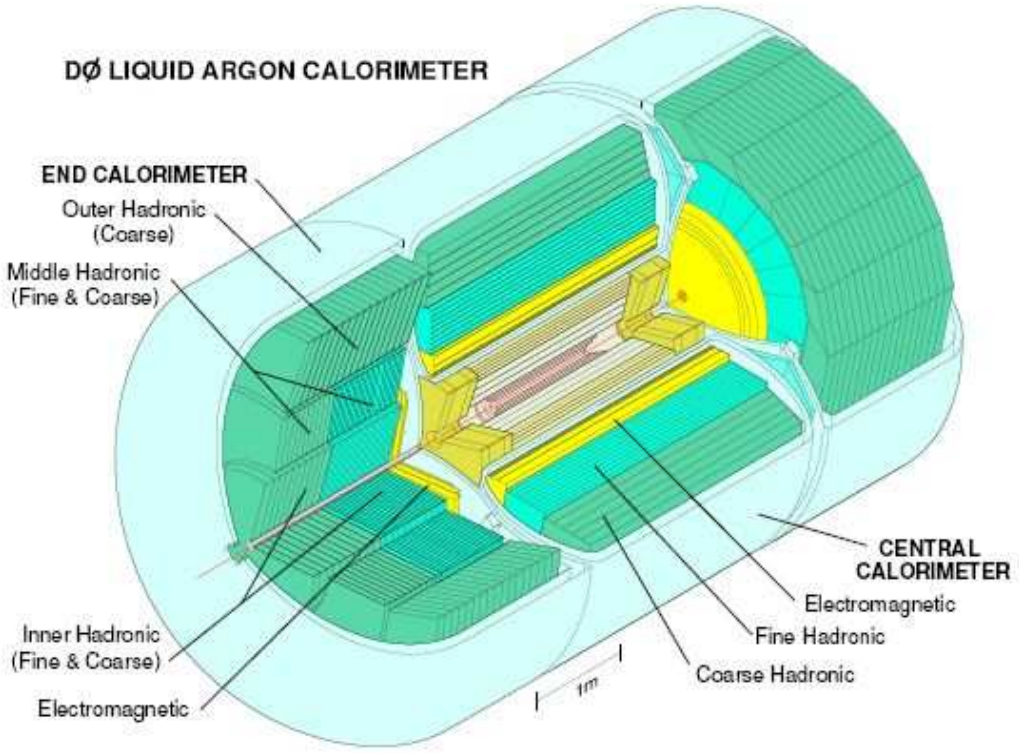

Figure 3.12. A three-dimensional cutaway view of the DØ Calorimeter system.

The DØ calorimeter is a compensating sampling calorimeter, using liquid argon as active medium and depleted uranium as well as copper and steel as absorber material. To allow access to the central detector regions the calorimeter is contained in three vessels or cryostats: the Central Calorimeter (CC) and a pair of End-Cap Calorimeters (EC). The central calorimeter covers a region of about $|\eta| < 1.2$ and the end-cap calorimeters extend detector coverage out to $|\eta| \approx 4.5$.

The central calorimeter (CC) is composed of three concentric cylindrical shells. The innermost ring contains electromagnetic modules (EM) segmented into four layers, the coarse hadronic modules are located in the outermost ring, and three layers of fine hadronic modules reside between the electromagnetic and coarse hadronic rings.

The End-cap Calorimeters (EC), on either side of CC, contain one EM module and three hadronic modules. The EM module contains four layers, the inner hadronic module consists of four fine hadronic layers followed by middle hadronic module which has four fine hadronic and an additional coarse hadronic layers, while the outermost hadronic module consists of three coarse hadronic layers.

Due to the structure and support system of the calorimeter cryostats there exists a gap between the central and end-cap calorimeter. The Inner Cryostat Detector (ICD) is used in this region to supplement the coverage. The ICD consists of scintillation counter arrays positioned on the inner wall of the EC cryostat to provide energy sampling in this region, which improves the calorimeter performance.

The calorimeter is highly modular and finely segmented in the transverse and longitudinal shower directions. Each module consists of a row of interleaved absorber plates and signal readout boards. The gap separating adjacent absorber plates and signal boards is filled with liquid argon as the active medium. Different absorber plate materials are used in different locations. The electromagnetic modules use uranium plates, the fine hadronic modules have uranium-niobium alloy plates, and the coarse hadronic modules contain plates of either copper or stainless steel. Figure 3.13 shows the side view of the calorimeter system and cell patterns.

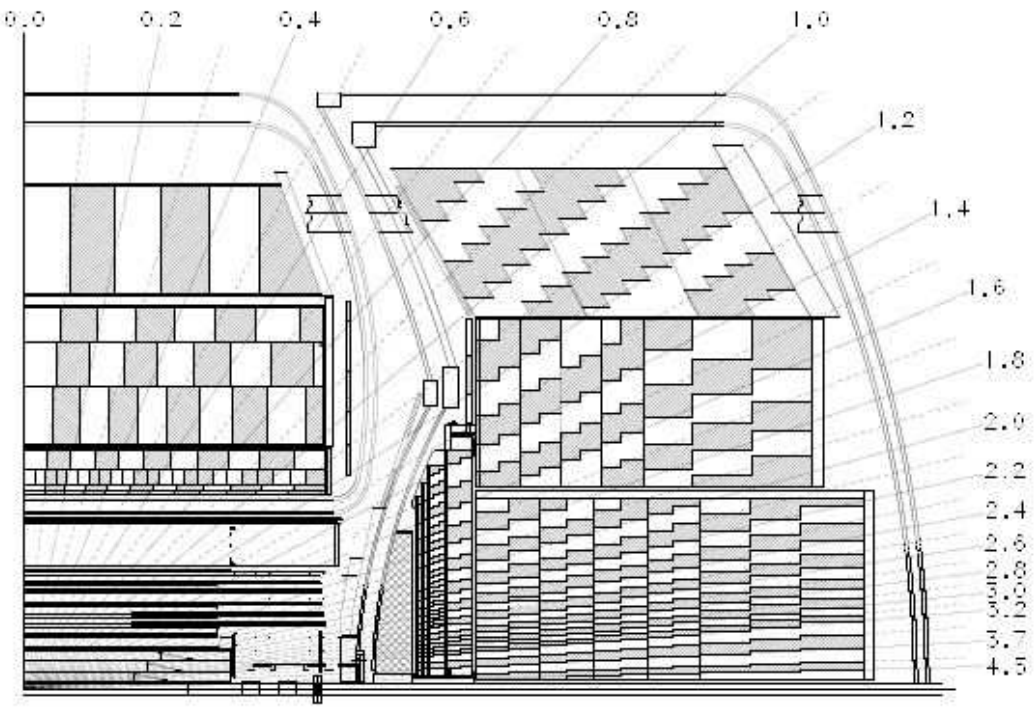

Figure 3.13. A quarter side view of the DØ Calorimeter system, with pseudorapidity plotted; the shading pattern indicates Calorimeter cells.

3.2.5 The Muon System

The muon detection strategy relies on the penetration power of muons. Muons are minimum ionizing particles which only deposit a small amount of their energy in the calorimeter. Therefore muons above a certain energy threshold ($\sim$3 GeV) will pass through the entire detector. This property determines the muon system is typically the outermost sub-detector in high energy physics experiments.

Surrounding the calorimeter system, the outermost and physically largest sub-detector of DØ detector is the Muon System [33]. The muon system is designed to identify muons and perform an independent measurement of their momenta. The three major components making up the DØ muon system are: the Central Muon detector, also called Wide Angle MUon Spectrometer (WAMUS) covering a range of $|\eta| < 1$; the Forward Muon detector, also called Forward Angle MUon Spectrometer (FAMUS) covering a range of $1 < |\eta| < 2$; and a solenoid iron toroid magnet producing a field strength of approximately 2 Tesla. The central and forward muon systems are made up of either proportional drift tube (PDT) [34] chambers or mini drift tube (MDT) [35] sections and a set of scintillation counters [36]. Figure 3.14 shows an illustration of the muon system, and Figures 3.15 and 3.16 show the schematic diagram of PDT/MDT and scintillation counter patterns.

The central muon system consists of a toroid magnet, large drift chambers of the *WAMUS* system, the *Cosmic Cap* and *Cosmic Bottom* scintillation counters, and $A-\phi$ scintillation counters. The system is comprised of three detection layers, increasing radially outward and labeled with the convention A, B, and C layer. Layer A resides between the calorimeter and the toroid magnet, while the B and C layers are positioned outside the toroid. A combination of proportional drift tube chambers and scintillators [37] make up each layer of the central muon system. Each chamber consists of three to four staggered decks of tubes, four decks for the A layer

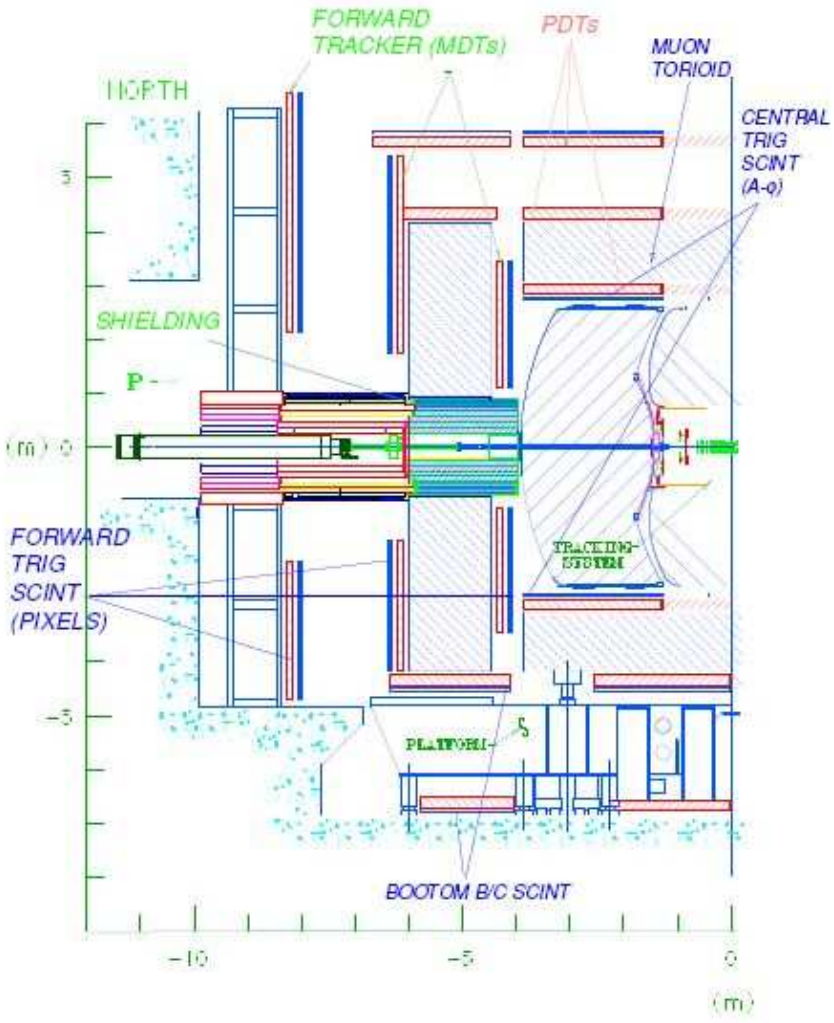

Figure 3.14. A schematic half side view of the DØ Muon system and its components.

except in the bottom A layer which has three decks, and three decks for the B and C layers. The geometry of deck and drift cells is shown in Figure 3.17. A layer scintillators called $A-\phi$ counters are located on the inner side of PDTs, while B and C layer scintillators (cosmic-cap) are mounted on the outer side of PDTs. The fast responding property of scintillator is used not only for triggering, but also for rejecting out-of-time muons from cosmic rays and back scattered particles from the forward region. Tables 3.1 and 3.2 list the number of drift chamber and scintillator of the muon system.

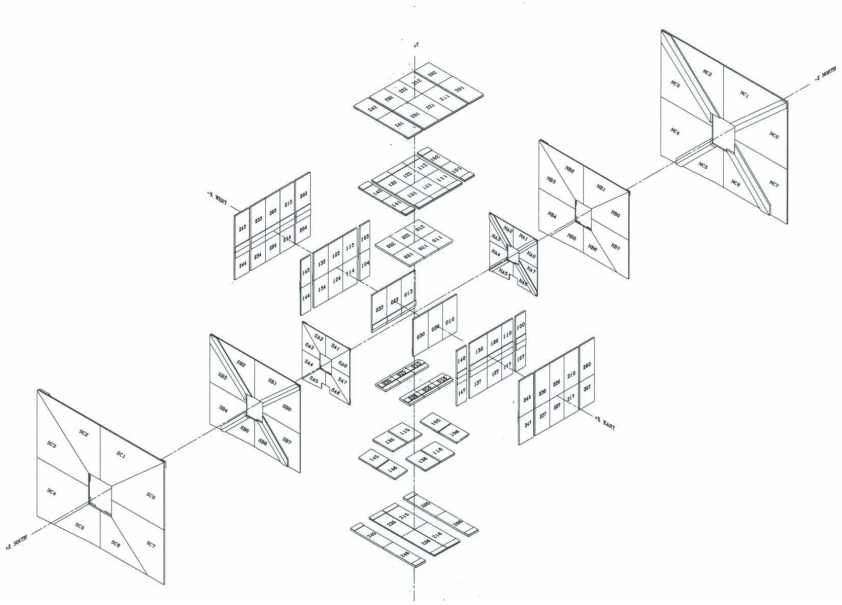

Figure 3.15. Diagram of Proportional Drift Tube (PDT) / Mini-Drift Tube (MDT) arrangement of the DØ Muon system.

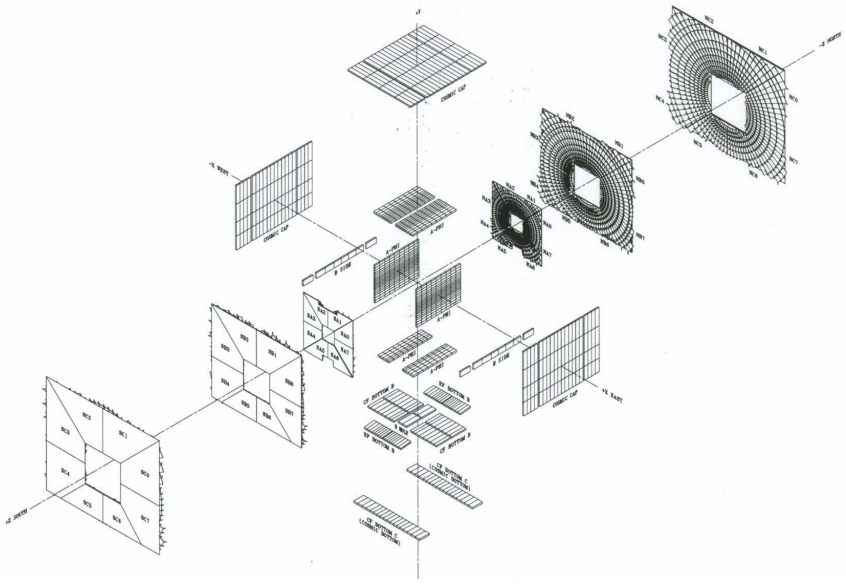

Figure 3.16. Diagram of Scintillation Counter arrangement of the DØ Muon system.

Table 3.1

Central Muon system (PDTs & PMTs)

Number of PDTs / PMTs	Layer			Total PDTs / MDTs
	A	B	C	
WAMUS PDTs	18	38	38	94
Cosmic Cap Counters (PMTs)	-	16	240	256
Cosmic Bottom Counters (PMTs)	-	80	36	116
A-ϕ Counters (PMTs)	630	-	-	630

Table 3.2

Forward Muon system (MDTs / Readout channels)

Number of MDTs / Readout Channels	Layer		
	A	B	C
Number of MDTs	2048	1944	2088
Number of Readout Channels	16384	15552	16704

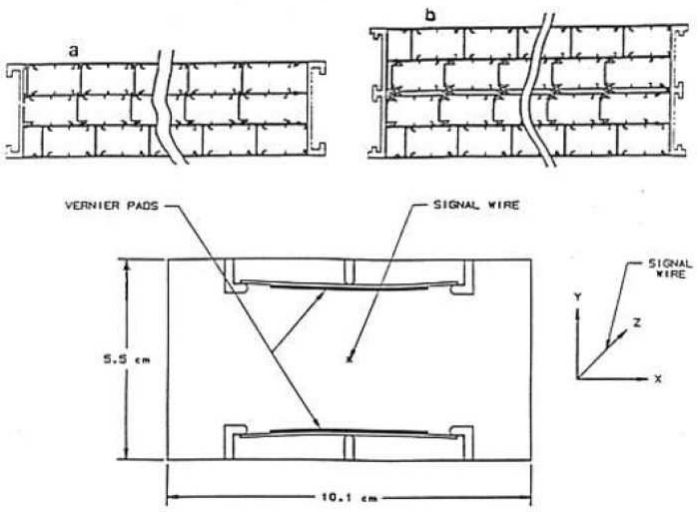

Figure 3.17. Geometry of the PDT deck (top) and cell (bottom) of the DØ Central Muon system.

Similar to the central muon system, the forward muon system also consists of a toroid magnet, three planes of $mini-drift$ tubes and scintillation counters ($Pixels$). One plane in front of, and two planes behind the forward toroid magnet, are called the A, B and C layer. Each layer is made up of a combination of mini-tube sections and scintillation pixel counters [38] which are mounted on the inner side (layer A and C) or outer side (layer B) of MDTs. The MDT sections contain three to four planes of tubes, four planes for A layer and three planes for B and C layers. Figure 3.18 illustrates two pixel counter octants of the DØ forward muon system, and Figure 3.19 shows a plane of forward muon MDTs.

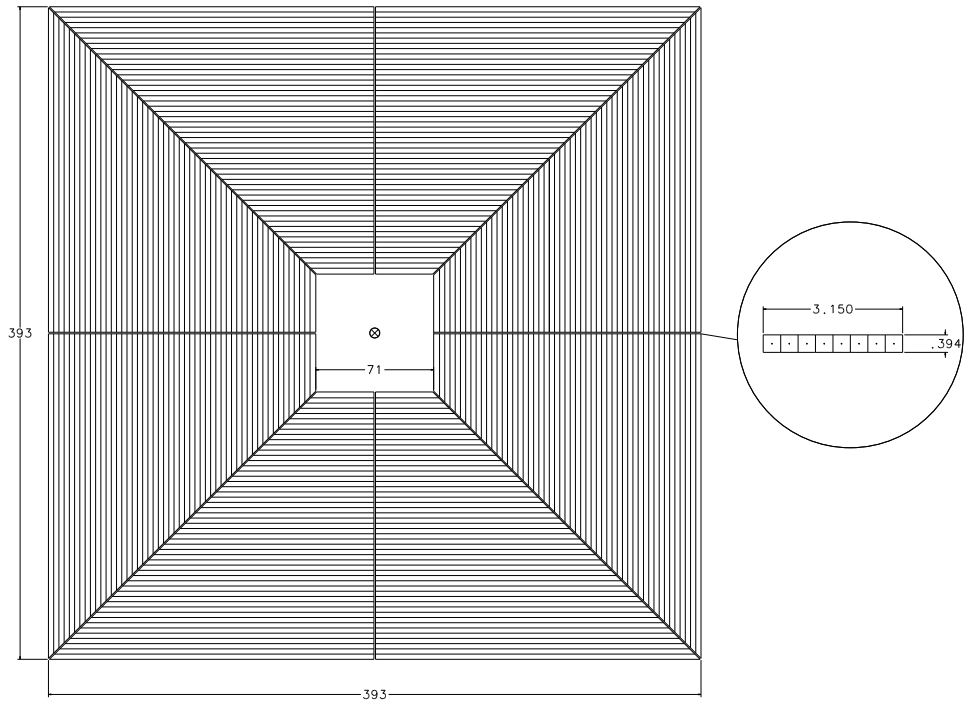

Figure 3.18. Forward Muon MDT plane. The octant boundaries are shown.

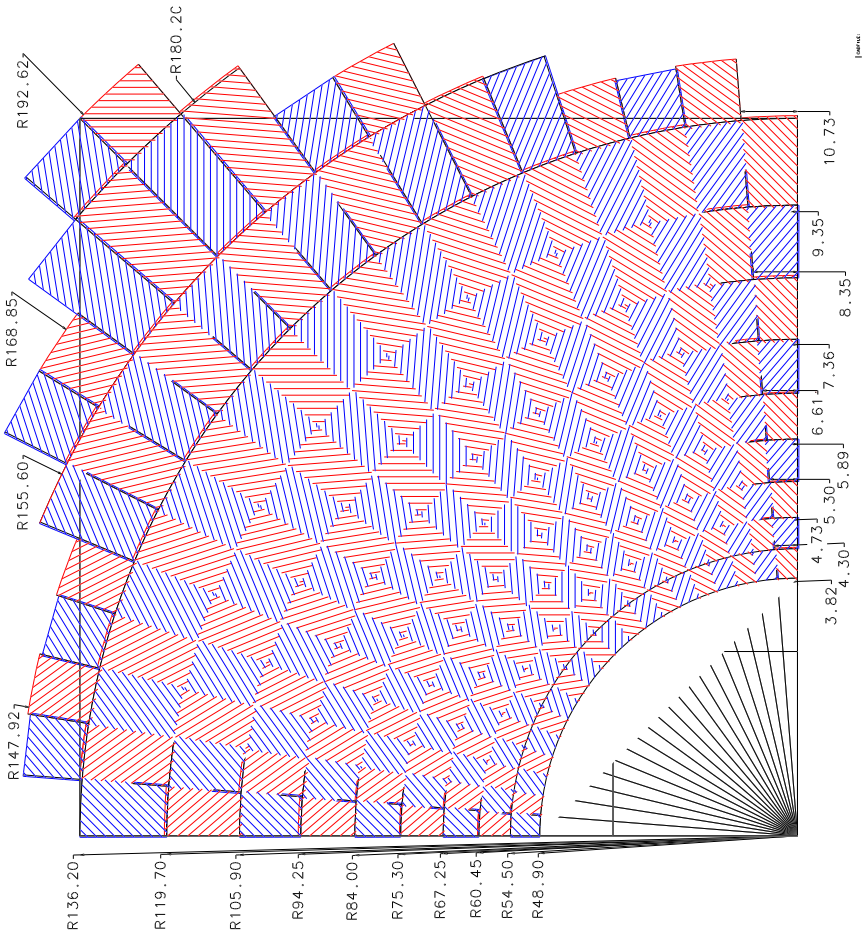

Figure 3.19. Side view of the Scintillator Pixel Counters of the Forward Muon system.

3.2.6 The Luminosity Monitor

The DØ Luminosity Monitor [39] consists of two arrays of plastic scintillation counters located on the inner surface of the endcap cryostats and arranged symmetrically around the beam pipe. The detector is placed at $|z| \approx 135$ cm and covers the region $2.7 < |\eta| < 4.4$. When an interaction occurs, the remnants of the incident proton and anti-proton give a pair of time correlated hits in the scintillators. The scintillation counter detects such non-diffractive inelastic collisions and the rate of collisions is used to determine the luminosity. Figure 3.20 shows a schematic view of the DØ luminosity system.

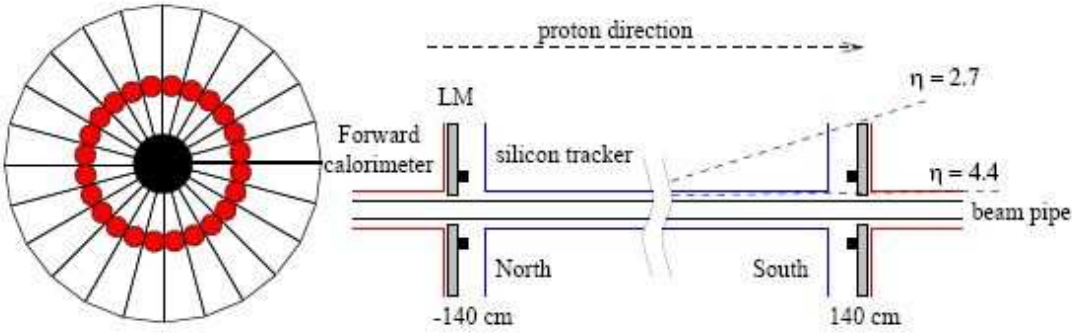

Figure 3.20. DØ Luminosity Monitor layout. Left: $r - \phi$ view, Right: $r - z$ view.

3.2.7 The Trigger and Data Acquisition System

At a hadron collider experiment such as the Tevatron roughly a few collisions out of a million are of physics interest; most of them are non-diffractive $p\bar{p}$ scattering and parton scattering which have no values to physicists. In addition, the total collision rate is far higher than can be processed and recorded. So it is necessary to find a solution to pick only the interesting events and discard the rest. Generally, the decision must be made quickly and according to a specific pattern corresponding

to some particular types of events, and it also should be flexible enough to recognize and accept events that may contain new physics. The DØ trigger system is a combination of both hardware and software elements designed to pick up a relatively few interesting collisions from high rate background and is organized into three main levels named level 1 (L1), level 2 (L2) and level 3 (L3). With each progressive trigger level, event selection is done in a increasingly sophisticated manner with a corresponding decreased output rate. A block diagram of the DØ trigger framework is shown in Figure 3.21.

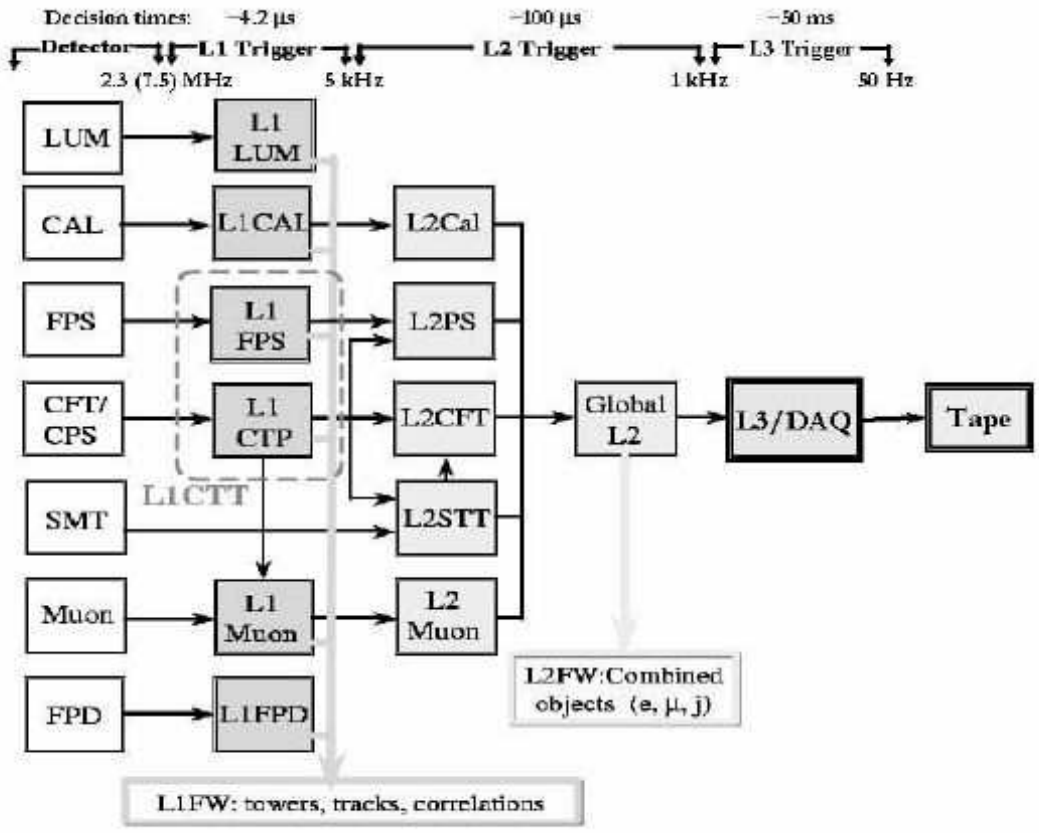

Figure 3.21. A block diagram of the DØ Trigger system and typical trigger rate.

The Level 1 trigger system is a hardware system based on simple algorithms implemented in Field Programmable Gate Arrays (FPGAs), including the central fiber tracker, the central and forward preshower, the calorimeter, and the muon detectors. The central fiber tracker, preshower and calorimeter provide electron triggering within $|\eta| < 2.5$. The CFT and the muon system provide muon triggering in the region $|\eta| < 2.0$. The L1 trigger subsystems process raw information from specific subdetectors and report their findings to the L1 trigger framework. If the criteria of the L1 trigger framework is satisfied, the L1 trigger framework issues an accept and the event information is digitized and moved from the pipeline to a series of buffers to wait a L2 trigger decision.

The Level 2 trigger system can be categorized into two stages. The preprocessor stage refines L1 information from individual sub-detectors for the second stage. The global processor stage combines and correlates information from the preprocessor stage and sends a decision to the Level 3 trigger system.

The third-level trigger is often described as an event filter. It is a software-based system characterized by parallel data paths which transfer data from the detector front-end crates to a farm of processors. When the L2 trigger system issues an accept, the Level 3 Trigger System and Data Acquisition System go into action. Information from the various sub-detector readout crates is collected by L3. The L3 trigger system combines and partially reconstructs data for each event which will be analyzed by a L3 filtering process. If any of the L3 criteria is satisfied, the event will be recorded by the data acquisition system.

CHAPTER 4

EVENT RECONSTRUCTION

The events recorded by the data acquisition system are in a raw data format which contains information such as hits in the central tracking system, digitized counts in the calorimeter cells, and timing information in the muon system, etc. The raw data need to be converted into physics objects such as photons, electrons, jets, muons, etc. before they can be used for physics analysis. The tasks are performed offline by a process called "event reconstruction" [40]. At DØ, the executable of the whole process is called "D0Reco", which performs four major tasks:

- **Hit Finding.** The digitized signals from the tracking detectors are converted into spatial locations of hits, while signals from calorimeter cells are converted to energies.

- **Tracking and Clustering.** The hits in the tracking detectors are combined to form tracks. The calorimeter energy depositions in the cells are grouped to form clusters.

- **Vertexing.** The location of the $p\bar{p}$ interaction is calculated using tracks in the central track system for the determination of various kinematic quantities.

- **Particle Identification.** The tracking and calorimeter information are combined together to form candidates of electrons, muons, photons, jets, etc.

4.1 Vertex Reconstruction

The ability to reconstruct vertices is of crucial importance for a modern high energy physics experiment. The vertex position is a fundamental quantity of every event and must be reconstructed with high precision to allow the precise determination of many physical quantities. At DØ, the vertices are reconstructed from tracks. The track-finding algorithm takes the hit information from the different layers of the central tracking system to build tracks. The process begins with the reconstruction of track segments in each layer. The segments in the first few layers are used to build a "seed" track, then the seed track is extrapolated to the remaining layers, and the propagation takes into account the effects of magnetic fileds, multiple scattering and energy loss in materials [41]. A fit of a track and a segment is performed to determine whether to add or reject the segment depending on the fitting χ^2.

4.1.1 Primary Vertex

The primary vertex refers to the hard-scattering vertex that triggered the event (i.e., the interaction point) or the vertex where additional interactions occurred. The position of the primary vertex is used to precisely calculate many physical quantities such as the transverse momenta of tracks and the transverse energies of jets. Primary vertex finding starts from a set of good quality tracks, and uses an iterative procedure to find the primary vertex. Figure 4.1 shows the simulated SMT hits for some typical $p\bar{p} \rightarrow t\bar{t}$ event at DØ.

- Fit a vertex from a set of tracks (N_{trk}) and compute $\chi^2(N_{trk})$.
- Compute the contribution to χ^2 from each track: $\Delta = \chi^2(N_{trk}) - \chi^2(N_{trk} - 1)$.
- Search for the track with maximum contribution Δ_{max} among the Δ.
- Exclude the track from valid set if $\Delta_{max} > \Delta_{threshold}$.
- Repeat the procedure while there are tracks with $\Delta_{max} > \Delta_{threshold}$.

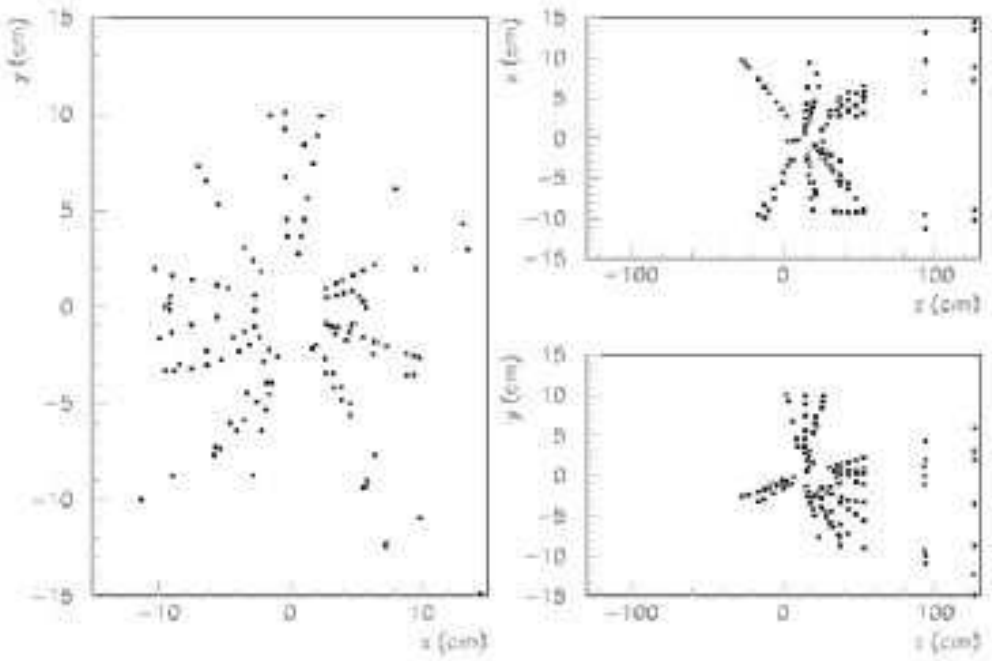

Figure 4.1. Simulated SMT hits for some typical $p\bar{p} \rightarrow t\bar{t}$ events at DØ.

This algorithm procedure can also handle events due to multiple interactions by storing the rejected tracks into a separate set and reusing this set for vertex finding. A minimum of two tracks is required to fit a vertex candidate.

4.1.2 Secondary Vertex

The secondary vertices are the displaced vertices that arise from the decay of long-lived particles, e.g., B and D mesons, as shown in Figure 4.2. The search for secondary vertices uses displaced tracks with respect to the primary vertex with the following procedure:

- Form a secondary vertex with two tracks not belonging to the primayr vertex or other secondary vertices.
- Fit the vertex from the set of valid tracks (N_{trk}) and compute $\chi^2(N_{trk})$.

- Loop over the other tracks and compute contribution to χ^2 when a track is added to the vertex: $\Delta = \chi^2(N_{trk}+1) - \chi^2(N_{trk})$.
- Search for minimum contribution Δ_{min} among the Δ.
- Add the good track to the set if $\Delta_{min} < \Delta_{threshold}$.
- Go back to step 2 and repeat the procedure until there are no more good tracks.

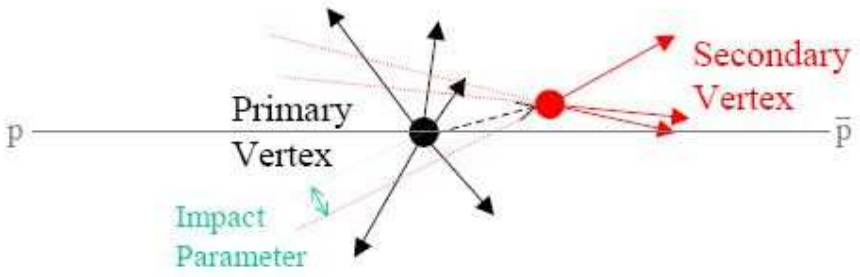

Figure 4.2. The schematic diagram of the primary vertex and the secondary vertex.

4.2 Electron Reconstruction

EM objects such as electrons and photons have similar shower shapes in the calorimeter and deposit the majority of their energy in the electromagnetic layers of the calorimeter. A hit-finding algorithm converts the raw information of digitized counts from each cell to energy. Corrections are applied to account for cell-by-cell variations and pedestals. The cell energies are then converted to the transverse energies by using the position of the interaction primary vertex. Cells with the same η and ϕ are grouped together to form EM towers which will be used for electron, photon, and jet identification. An initial EM cluster should pass the crude selection criteria as follows:

- Transverse energy $E_T > 1.5$ GeV.

- The fraction of the total energy deposited in electromagnetic calorimeter layers to the total energy deposited in all calorimeter layers, $EMfraction > 0.9$.

- Fulfill the isolation criteria, which are defined as $\frac{E^{0.4}_{total} - E^{0.2}_{EM}}{E^{0.2}_{EM}} < 0.2$, where $E^{0.4}_{total}$ is the total energy in the towers within a cone of radius 0.4 in the $r - \phi$ space around the center of the cluster and $E^{0.2}_{EM}$ is the energy deposited in the EM layers of the calorimeter within a cone of radius 0.2 around the center of the cluster. Small values of isolation correspond to the situation that most of the energy is deposited in a narrow region of the EM layers in the calorimeter which is a characteristic of an electron or a photon.

4.3 Muon Reconstruction

Reconstruction of the muon [42] starts with the conversion of the raw hits and time information into three-dimensional position information. After the individual hits are found, track segments in each layer are formed by fitting groups of hits to a straight line. The tracking is done separately for segments before and after the toroid magnet. The segments are then matched and the momentum is determined from the bend of the track while it passes through the magnetized iron. The muon tracks are then extended to the point of closest approach to the beam and their parameters are compared with those of central tracks by performing a global fit. The momentum is corrected for the loss of energy in the calorimeter by matching tracks in the central tracking system to those in the muon system. The combined results of the object reconstruction in the muon system with the information provided by the central tracking system and the calorimeter system are used to construct a global muon object suitable for physics analysis.

The momentum resolution of the muon system has been studied using reconstructed muons for which a central track was associated. The momentum resolution

for muons as measured by the muon system, $\sigma(p_T)/p_T$, varies between 0.1 for low momentum muons and 0.5 for muons with p_T >50 GeV [43]. The overall muon momentum resolution with a transverse momentum of 100 GeV, including information from central tracking system, is approximately 15% [44].

4.4 Jet Reconstruction and Missing E_T

The QCD theory implies that colored particles are always confined by the strong force and cannot exist alone. When an energetic parton is produced in a $p\bar{p}$ collision and moving away from other partons, the potential of the strong force field between the partons grows as the distance increases until the energy is large enough to create a parton-antiparton pair out of the vacuum. Such processes take place as more particles are generated until the energy is too low to permit the creation of parton pairs. This *hadronization* process produces a group of hadrons moving in about the same direction of the original parton and depositing a cluster of energy in the calorimeter to form a *jet*. In the DØ calorimeter, jets are reconstructed from the energy depositions in the calorimeter cells with a cone algorithm which will be further described in more detail in Chapter 6.

The missing transverse energy $\not\!\!E_T$ is a simple inclusive variable that can be the signature of particles escaping from the detector without interacting in it. These particles can be either neutrinoes or particles emitted at very low angles along the beam pipe, or new particles as predicted, for instance, in supersymmetric theories. $\not\!\!E_T$ shows the momentum imbalance of an event. It is the opposite vector to the vector sum of transverse energies of all measured particles. In measurement, the transverse energies of all calorimeter cells are added vectorially except "hot cells" and cells with a high level of noise. Since muons are minimum ionizing particles, the transverse momentum of each muon in an event is subtracted from $\not\!\!E_T$.

4.5 Monte Carlo Simulation

The Monte Carlo simulation [45] constitute an extremely important and commonly used class of tools utilized by high energy particle physics. The term "Monte Carlo" refers to numerical simulation of processes characterized by sets of random numbers. These variables assume values in accordance with predescribed probability distributions and may be used to simulate the collision of interesting hadrons and to model the observation of the scattered collision products within an appropriately designed detector. In general, the simulation proceeds in two steps: event generation and detector response simulation.

4.5.1 Event Generation

Event generators [45] are programs that generate the physics events of a $p\bar{p}$ interaction. Their output is usually just a list of vertices and particles that come out of these vertices. The commonly used event generator at DØ is the PYTHIA [46] event generator. The event generator has been carefully deveoped to simulate the properties of $p\bar{p}$ collisions in both average behavior and the fluctuations, including hard and soft subprocesses, parton distributions, initial and final parton showers, beam remnants and underlying events, fragmentation and decays, etc.

Another event generator used by DØ is the ALPGEN [47] event generator. ALPGEN simulates the leading order matrix elements for $2 \rightarrow n$ (where n can be greater than 4) multiparton processes, while PYTHIA mainly simulates the $2 \rightarrow 2$ and $2 \rightarrow 1 \rightarrow 2$ processes. So ALPGEN is especially well suited for simulating $boson(s) + jet(s)$ production.

4.5.2 Detector Simulation

The purpose of the detector simulation is to compute the detector response to the simulated events. The typical full simulation is based on the GEANT [48] program from CERN. GEANT is a program that can describe the true geometry of a detector by building it up from a library of known shapes. It also has extensive knowledge of the interaction of particles with materials, and simulates the behavior of particles passing through a detector. The output events of the full simulation are in the same format as the raw data, and are passed to the event reconstruction programs.

CHAPTER 5

MUON IDENTIFICATION

As described in the previous chapter, the muon system consists of drift tubes and scintillation counters. Muon reconstruction begins with unpacking the electronic signal information from these tubes and counters into physical quantities such as wire hits and drift time. Then muon hits, segments and local muon tracks are reconstructed, and a matching between a local muon and a charged particle detected by the central tracking system is done, followed by a global track fitting. Information from all these stages is used for muon identification and quality classification for a muon candidate.

5.1 Muon Hit Reconstruction

The muon spectrometer is made up of three kinds of detector: Proportional Drift Tube in the central region, Mini-Drift Tube in the forward region, and Muon Scintillation Counter in both central anf forward region, corresponding to three types of muon hit reconstruction: PDT, MDT and MSC hit reconstruction [49].

5.1.1 PDT Hit Reconstruction

The central muon system has 94 proportional drift tube chambers; each chamber contains many cells and each cell has a wire in the center of the tube and can be

read out from both ends. Both drift time (the time it takes the signal to reach the wire) and axial time (the time it takes the signal to reach the clock from the place where it first hit the wire) are measured. The hit map can be reconstructed according to the time-to-distance relationship.

5.1.2 MDT Hit Reconstruction

6080 mini drift tubes reside in the forward region. Each tube contains one wire. Unlike the PDT, the wire can only be read out from one end. The stored readout time is the sum of the drift time and the axial time. It is impossible to know where the hit occured along the wire. The hit is assumed to have occured at the middle of the wire. This position can be more precisely measured when combined with the scintillator information.

5.1.3 MSC Hit Reconstruction

Scintillators provide timing information for muon triggering and positioning, as well as cosmic ray rejecting. The position of a hit is assumed to have occurred in the middle of the scintillator, and the position resolution is equal to half the relevant dimension of the scintillator. The time resolution is about 1-3 ns according to the size of the individual scintillator.

5.2 Muon Segment Reconstruction

Muon segment reconstruction [50] is a part of the muon reconstruction where the pattern recognition is performed. Hits in the muon chambers are combined, and a straight line segment is fitted through the hits. The algorithm can be divided into the following steps:

- Transformation of “global” hits to “local hits.”

- Creation of links between hits.
- Matching of links into local segments.
- Fitting of local segments.
- Applying vertex constraint for A-layer segment if applicable.
- Matching of local segments.
- Applying chisquare cut.
- Filtting of local segments and transforming back to global segments.

5.3 Muon Track Reconstruction

Muon tracks are reconstructed at the local muon system first, then a matching between the local muon system and the central tracking system is performed and a global muon track is reconstructed.

5.3.1 Local Track Reconstruction

The purpose of the muon local track reconstruction [51] is to identify and determine the momentum of the muon tracks. The fitting algorithm is used to reconstruct a muon track from a pair of segments (two segments respectively in A and B-C layers) by taking into account the propagation of the track in the toroidal magnetic field, multiple Coulomb scattering and the energy loss in the toroid, then the muon momentum can be estimated according to the track bending between the A and B-C layers.

5.3.2 Local Central Match

The muon momentum determined by the local muon system is not as precise as that measured with the central tracking system. The combination of local muon information with that of the central tracking system will greatly improve the measurement of muons. At DØ, the track matching between the local muon system and central tracking system is performed by using error matrix propagation [52] taking into account the magnetic field in both solenoid and toroid, as well as multiple Coulomb scattering and energy loss in the magnet and calorimeter. The error matrix of the local muon is propagated through the toroid and the calorimeter, then the central tracking information is combined at the distance of closest approach to the beam axis (*dca*) to obtain the final track parameters. Figure 5.1 illustrates a match of a local muon track with a central track.

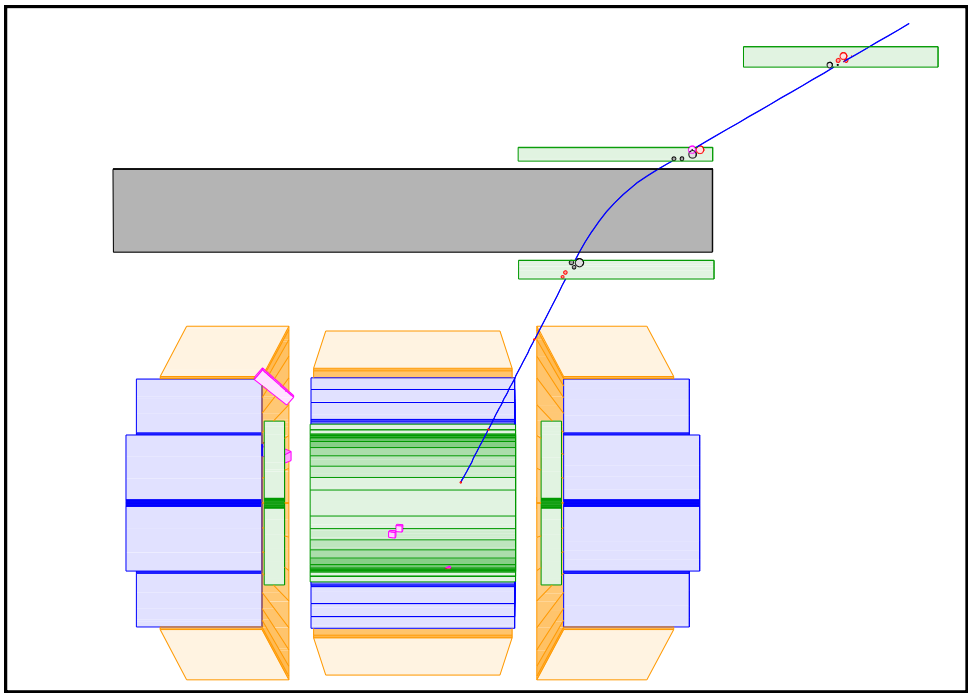

Figure 5.1. Track matching between Local Muon and Central Tracking system.

5.4 Muon Identification

The offline muon identification [53] is based on a match between a charged particle detected in the central tracking system. Reconstructed muons are classified using two parameters: muon *type* and muon *quality* [54]. The definition of the muon *type* and *quality* can be different for the different release versions of DØ offline software packages [55].

5.4.1 Muon Type

The status of a match between a local muon and a central charged particle is reflected by the muon *type* given by a variable called **nseg**:

- Track Match (**nseg=3**)

  A muon with nseg=3 consists of an A and a BC segment (a local muon track) matched to a central track. The local muon track and the central track are combined to give the 4-vector of the muon.

- Segment Match (**nseg=2, 1**)

  A muon with nseg=2 consists of a BC segment matched to a central track. In this case the 4-vector of the muon are directly coming from the central track. A muon with nseg=1 consists of an A segment matched to a central track. In this case the central track and the A segment are combined to give the muon 4-vector.

- Hit Match (**nseg=0**)

  A muon with nseg=0 does not have any muon segment. It is either a central track matched to a muon hit or to a calorimeter muon (MTC). The 4-vector of the muon are directly coming from the central track.

- Segment Only (**nseg=-1, -2**)

  A muon with nseg=-1 consists of an A segment only, not matched to a central track. In this case the 4-vector should not be used because no momentum measurement is provided.

  A muon with nseg=-2 consists of a BC segment only, not matched to a central track. The transverse momentum and the 4-vector of the muon are estimated from the direction of the BC segment with respect to the center of the detector.

- Local Track (**nseg=-3**)

  For a muon with nseg=-3, a first estimation of the transverse momentum is made from the curvature between A and BC segments. A fit of the A and BC segments into a local muon track is made. If the fit is successful the momentum of the fitted local muon track becomes the momentum of the muon. Otherwise the initial momentum estimation is kept.

5.4.2 Muon Quality

The muon *quality* is based on the quality of the track information reconstructed in the muon system. The muon quality can be "*Loose*", "*Medium*" or "*Tight*" [54].

5.4.2.1 Muon Quality in p13

In p13, muon qualities are defined by the following criteria:

- **Tight Muon**

  At least two wire hits in the A layer (inside the toroid), $whits\_a > 1$.

  At least one matching scintillator hit in the A layer, $shits\_a > 0$.

  At least three wire hits in the B/C layers (outside the toroid), $whits\_bc > 2$.

  At least one matching scintillator hit in the B/C layers, $shits\_bc > 0$.

  A successful fit, $chi2 > 0$.

- **Medium Muon**

  At least two wire hits in the A layer (inside the toroid), $whits\_a > 1$.

  At least one matching scintillator hit in the A layer, $shits\_a > 0$.

  At least two wire hits in the B/C layers (outside the toroid), $whits\_bc > 1$.

  At least one matching scintillator hit in the B/C layers, $shits\_bc > 0$.

- **Loose Muon**

  A "loose" muon is defined as a "medium" muon but allows one of the above tests to fail, with the $shits\_a$ and $whits\_a$ treated as one test.

The efficiency of p13 muon quality is not as good as expected due to tight definition criteria. In the p13 *DØReco* version, out of muons detected by the local muon system, only 85% can be recognized as of medium quality. That meant 13% muons were lost from loose to medium quality, so it is necessary to optimize the muon quality definitions to make them reasonable.

The p13 muon qualities were carefully studied by adding each cut in their definitions. The samples used in the studies include:

- **All Muons (data):** All muons detected by local muon system without any cut.

- $J/\psi \rightarrow \mu\mu$ **(data):** The muon pair is required to have opposite sign, both muons are required to have transverse momentum p_T<15 GeV, and the invariant mass of two muons must be in the vicinity of the J/ψ resonance, i.e., 2.8 GeV< $M_{\mu\mu}$ <3.4 GeV.

- Z $\rightarrow \mu\mu$ **(Monte Carlo):** The muon pair is required to have opposite sign, both muons are required to have transverse momentum p_T >15 GeV, and the

invariant mass of two muons must be in the vicinity of the Z resonance, i.e., 70 GeV$< M_{\mu\mu} <$110 GeV.

For simplicity, we redefine the cuts in the muon quality definitions:

$S_a \equiv shits\_a > 0$, $W_a \equiv whits\_a > 1$, $S_a W_a \equiv (shits\_a > 0$ and $whits\_a > 1)$.

$S_{bc} \equiv shits\_bc > 0$, $W_{bc} \equiv whits\_bc > 1$, $S_{bc} W_{bc} \equiv (shits\_bc > 0$ and $whits\_bc > 1)$.

$S_{abc} \equiv (shits\_a > 0$ and $shits\_bc > 0)$, $W_{abc} \equiv (whits\_a > 1$ and $whits\_bc > 1)$.

$S_{abc} W_a \equiv (shits\_a > 0$ and $shits\_bc > 0$ and $whits\_a > 1)$.

$S_a W_{abc} \equiv (shits\_a > 0$ and $whits\_a > 1$ and $whits\_bc > 1)$.

$W_{bc2} \equiv whits\_bc > 2$, $Chi2 \equiv chi2 > 0$.

Then the p13 muon quality criteria become:

- **Tight Muon:** S_{abc} and W_a and W_{bc2} and $Chi2$.
- **Medium Muon:** ($S_a W_a$ and $S_{bc} W_{bc}$) or (S_{abc} and W_{abc}).
- **Loose Muon:** (S_{abc} and W_a) or (S_a and W_{abc}) or (S_{bc} and W_{bc}).

The study algorithm begins with *loose* muon. Muons in each sample are treated as 100, then each cut (or a combination of cuts) in the muon quality criteria is applied to the samples to obtain the remaining fraction after each cut until the *medium* muon criteria is reached. The procedure is repeated from *medium* to *tight* muon criteria. Table 5.1 shows the remaining fraction for *loose*, *medium* and *tight* muons, Table 5.2 lists the inefficiency contribution to the central region of each cut, while Figures 5.2, 5.3, and 5.4 illustrate the relative fraction after each cut for the "all muon (data)", "J/ψ muon (data)" and "Z muon (Monte Carlo)" samples respectively.

As shown in the tables and figures, from loose to medium muons, the most inefficient cut is "S_{bc}", i.e., $shits\_bc > 0$ for all samples, especially in the central

Table 5.1

Treat all local muons as 100, this table list relative fraction of loose, medium and tight muons

Sample	Local Muons	Loose Muons	Medium Muons	Tight Muons
all muons (data)	100	97.8	85.0	77.5
$J/\psi \rightarrow \mu\mu$ (data)	100	99.3	88.8	83.9
$Z \rightarrow \mu\mu$ (MC)	100	99.1	90.8	89.4

Table 5.2

Inefficiency contribution of each cut to muon quality (central region $\eta < 1.0$)

Muon Samples	Inefficiency Contribution (Central Region)					
	Medium				Tight	
	S_a	W_a	S_{bc}	W_{bc}	W_{bc2}	$Chi2$
All Muons (data)	1.2	2.9	6.9	1.9	1.3	6.4
J/ψ Muons (data)	0.4	2.4	4.9	2.8	1.1	3.8
Z muons (Monte Carlo)	0.7	2.1	5.2	0.2	0.6	0.9

region. $\eta - \phi$ distributions (Figure 5.5) show that almost all muons without $shits\_bc$ hits are located in the central region, indicating that the central muon scintillators are not efficient enough; however, this is because of the geometry acceptance of the central muon scintillator, and the muon quality criteria need to be optimized in this region for future physics analysis.

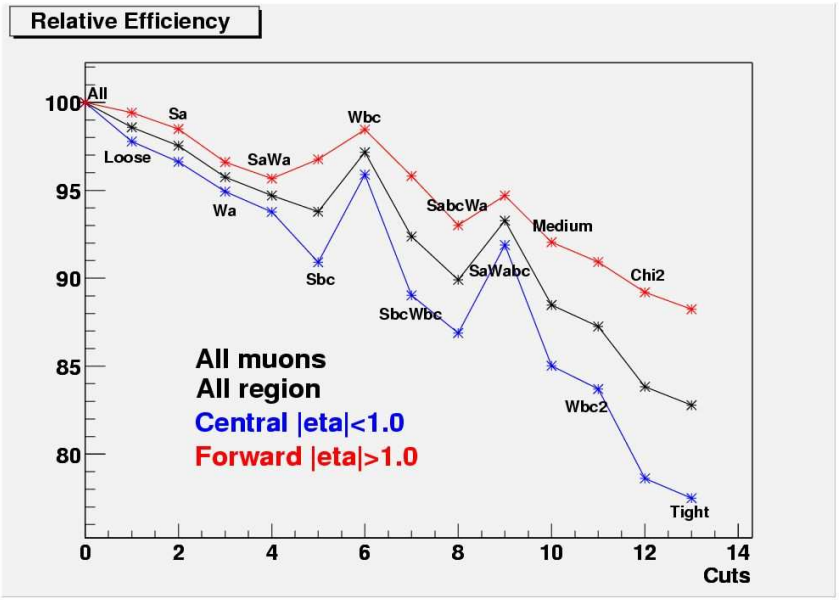

Figure 5.2. Relative efficiency of each cut in muon quality criteria for "All Muon" sample (Data).

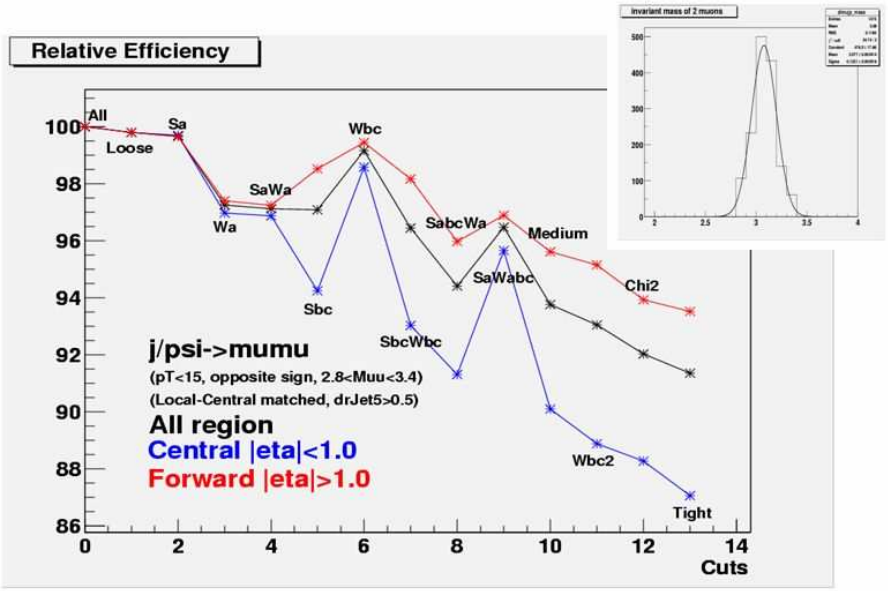

Figure 5.3. Relative efficiency of each cut in muon quality criteria for "J/ψ muon" sample (Data); upper right is the invariant mass of two muons.

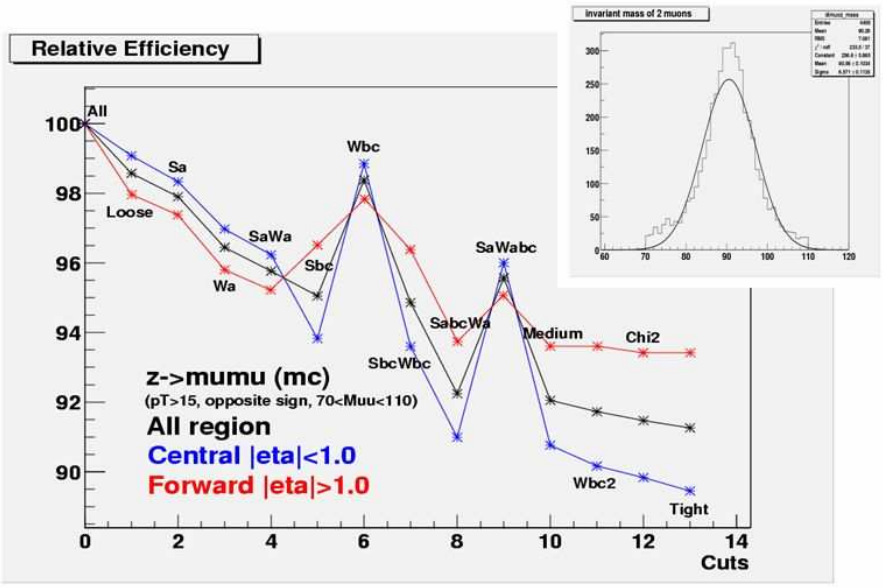

Figure 5.4. Relative efficiency of each cut in muon quality criteria for "Z Muon" sample (Monte Carlo); upper right is the invariant mass of two muons.

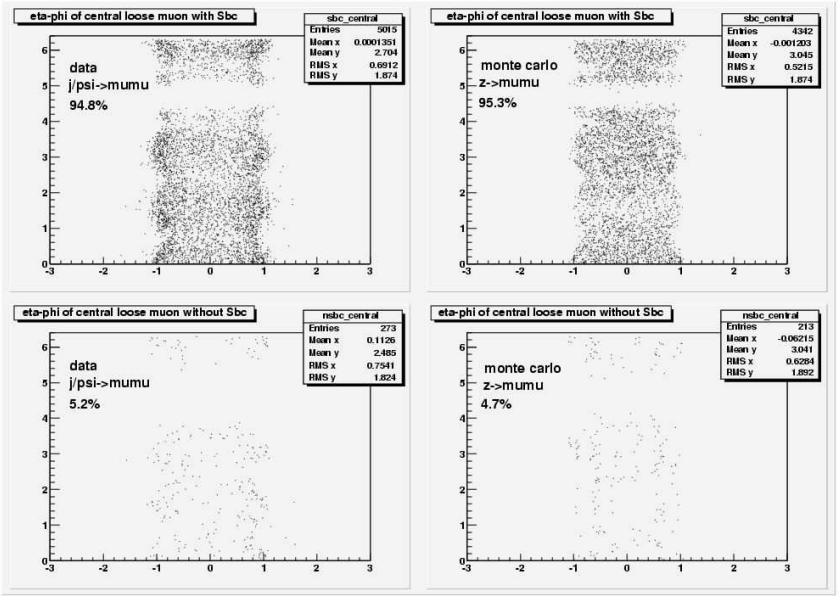

Figure 5.5. $\eta - \phi$ Distribition of muon samples. Upper: Muons with *shits_bc* hits; Lower: Muons without *shits_bc* hits; Left: J/ψ muons (Data); Right: Z muons (MC).

5.4.2.2 Muon Quality in p14 and Later

The Tight muon defnition has remained unchanged since p10. The Medium and Loose muon effciencies were optimized by loosening the requirements on the local muon in regions with reduced acceptance and by instead requiring in these regions a confirmation from the central tracking system. The resulting p14 Loose and Medium muon criteria are more efficient and provide muon_id performance less sensitive to the detailed geometry of the muon detector. The definitions for Tight, Medium, and Loose muon are given below.

- **Tight Muon**

  At least two wire hits in the A layer (inside the toroid), $whits\_a > 1$.

  At least a matching scintillator hit in the A layer, $shits\_a > 0$.

  At least three wire hits in the B/C layers (outside the toroid), $whits\_bc > 2$.

  At least one matching scintillator hit in the B/C layers, $shits\_bc > 0$.

  A converged local fit, $\chi^2_{local} > 0$.

- **|nseg|=3 Medium/Loose muons**

  When an |nseg|=3 muon candidate fails the Tight muon criteria it might still be a Medium or Loose muon.

  An |nseg|=3 muon is a Medium muon if it has:

  1. At least two wire hits in the A layer.
  2. At least a matching scintillator hit in the A layer.
  3. At least two wire hits in the B/C layers.
  4. At least one matching scintillator hit in the B/C layers except for central muons with less than four BC wire hits.

  An |nseg|=3 Loose muon is defined as a Medium muon but allowing one of the above tests to fail, with the A wire and scintillator requirement treated as one test and requiring always at least one scintillator.

- **nseg=2 Loose/Medium muons**

  Muons with |nseg| <3 can only be Loose or Medium if they are matched to a central track.

  An nseg=2 muon is a Loose muon if it has:

  1. At least two wire hits in the B/C layers.

  2. At least one matching scintillator hit in the B/C layers.

  An nseg=2 muon is defined as Medium muon if it fullfills the above requirements and if it is located in the bottom part of the detector (octant 5 and 6 with $|\eta| < 1.6$).

- **nseg=1 Loose/Medium muons**

  An nseg=1 muon is a Loose muon if it has:

  1. At least two wire hits in the A layer.

  2. At least a matching scintillator hit in the A layer.

  An nseg=1 muon is defined as Medium if it fullfills the above requirements and if it is located in the bottom part of the detector (octant 5 and 6 with $|\eta| < 1.6$). Low momentum nseg=1 muons are also defined as Medium muons. An nseg=1 muon is qualified as a low momentum muon if its probability to reach the BC layer is less than 0.7.

CHAPTER 6

JET IDENTIFICATION

Hadronic particles interacting with the calorimeter result in a shower of hadronic particles which has typically the shape of a cone, and are reconstructed as jets in the calorimeter. The ideal jet algorithm should reconstruct the kinematic properties of the initial hadronic particle. At DØ cone jet algotithm is used for the reconstruction of jets.

6.1 Cone Jet Algorithm

Cone algorithms [56] form jets by associating together particles whose trajectories lie within a circle of specific radius R in $\eta - \phi$ space. This 2-dimensional space is natural in $p\bar{p}$ collisions where the dynamics are spread out in the longitudinal direction. Starting with a trial geometric center (or axis) for a cone in $\eta - \phi$ space, the energy-weighted centroid is calculated including contributions from all particles within the cone. This new point in $\eta - \phi$ is then used as the center for a new trial cone. As this calculation is iterated the cone center "flows" until a "stable" solution is found, i.e., until the centroid of the energy of the energy deposition within the cone is aligned with the geometric axis of the cone. Detailed cone algorithm procedures are listed below:

- **Preclustering.** The calorimeter towers are ordered in E_T. Starting from the highest E_T tower, for every tower with $E_T > 1$ GeV, a precluster is constructed of adjacent towers within $\Delta\eta < 0.3$ and $\Delta\phi < 0.3$. The process continues until all towers are assigned to a precluster.

- **Cone Clustering.** The axis of a corresponding candidate jet is defined by the E_T weighted centroid of each precluster. From it, all towers within a specific radius ($\Delta R = \sqrt{(\Delta\eta)^2 + (\Delta\eta)^2}$=0.5 or 0.7) in $\eta - \phi$ space are assigned to the cluster. The process is repeated until the jet is stable.

- **Merging and Splitting.** If two jets share some towers, the fraction of total energy that is shared between them is examined. If it is more than 50% of the E_T for the lower E_T jet, the two jets are merged and the jet axis is recalculated. Otherwise, they are split into two jets with each tower being assigned to the closest jet.

- **Suppress Noise Fluctuations.** The E_T threshold of a jet is $E_T > 8$ GeV.

6.2 Jet Identification

Once jets are clustered following the cone algorithm, further quality selection cuts [57] are applied to each jet to remove fake jets which are not reconstructed from hardronic particles via hard interactions.

- To remove isolated electromagnetic particles, a cut on the energy fraction, deposited in the electromagnetic section of the calorimeter (**EMfraction**), is applied at $0.05 < EMfraction < 0.95$.

- To remove jets which predominantly deposit their energy in the coarse hadronic section of the calorimeter, a cut on the fraction of the jet energy deposited

in the coarse hadronic section of the calorimeter (**CHfraction**) is applied at $CHfraction$<0.4. This cut is essentially aimed at removing those jets which are clustered around noise in the coarse hadronic section of the calorimeter.

- To remove jets clustered from hot cells, a cut on the ratio of the highest to the next-to-highest energy cell in the calorimeter (**Hotfraction**) is applied at $Hotfraction$<10.0.

- To remove those jets clustered from a single hot tower, the number of calorimeter towers containing 90% of the jet energy (N_{90}) is required to be $N_{90}>1$.

- Level 1 jet verification:

  $\frac{\text{L1set}}{\text{E}_\text{T}^\text{reco}\times(1-\text{CHfraction})} > 0.4$ in central "CC" and end-cap "EC" calorimeter region

  or

  $\frac{\text{L1set}}{\text{E}_\text{T}^\text{reco}\times(1-\text{CHfraction})} > 0.2$ in the inner-cryostat "ICD" calorimeter region.

  where "L1set" is a new variable defined as the scalar sum of the trigger towers E_T inside the cone for a given jet, and is demonstrated to be powerful discriminant against calorimeter noise.

6.3 Jet Energy Scale

The energy of a reconstructed jet is the sum of the energies in all calorimeter towers within the jet cone. The calorimeter is very effective at absorbing the hadronic energy of the jet. However there are several mechanisms, such as *Calorimeter Response*, *Energy Offest*, and *Showering Correction*, which cause the energy of the cells clustered into a jet to deviate from the energy of the initial parton.

- **Calorimeter Response (R)**

  Hadronic showers may lose energy in ways which do not leave any ionization; electromagnetic and hadronic particles may therefore be imbalanced. Furthermore, the measured jet energy can be distorted due to a different response of the calorimeter to different particles, a non-linear response of the calorimeter to the particles energies, un-instrumented regions of the detector or dead materials. The calorimeter response R is determined by examining photon+jets events. The energy of the photon is purely electromagnetic and its electromagnetic energy scale can be calibrated independently by using well known $Z \rightarrow e^+e^-$ events. The transverse energy of the jets should therefore balance the transverse energy of the photon.

- **Energy Offest (E_{offest})**

  Energy in the clustered cells which is due to the underlying event, multiple interactions, energy pile-up, electronis noise and noise from the Uranium absorber can provide an offest to the jet energy. Energy Offest E_{offest} is measured from the transverse energy density in *minimum bias* events as a function of detector pseudorapidity η_{det}, where *minimum bias* events are enents triggered when a minimum activity in the luminosity monitor is reported.

- **Showering Correction (S)**

  Due to the fixed radius in the cone jet algorithm, the energy of particles showering outside the cone is not included in the energy measurement. The shower profile of the jet in photon+jet events is measured as the average energy density as a function of the distance from the jet center. The showering correction S is calculated as the ratio of the energy contained within the algorithm cone to the energy contained in a much larger cone where the energy density decreases to zero at the edge of the larger cone.

The Jet Energy Scale (JES) [58] corrections attempt to correct the reconstructed jet energy, E_{jet}^{reco}, back to the particle level energy, $E_{jet}^{particle}$, as it would have been before interacting with the calorimeter. Taking into account above correction factors, the correction may be written as

$$E_{jet}^{particle} = \frac{E_{jet}^{reco} - E_{offset}}{R \cdot S} \tag{6.1}$$

Since the Monte Carlo may not model all these effects accurately, there can be a difference in the scale of jets in data versus those in Monte Carlo. The uncertainties assigned to the jet energy scale comprise both the statistical and the systematic uncertainties on the data and the Monte Carlo measurements, and can be expressed as:

$$\sigma = \sqrt{(\sigma_{data}^{stat})^2 + (\sigma_{data}^{syst})^2 + (\sigma_{MC}^{stat})^2 + (\sigma_{MC}^{syst})^2} \tag{6.2}$$

Figures 6.1 and 6.2 show the jet transverse energy before and after JES correction, as well as the associated statistical and systematic errors in data and Monte Carlo, respectively.

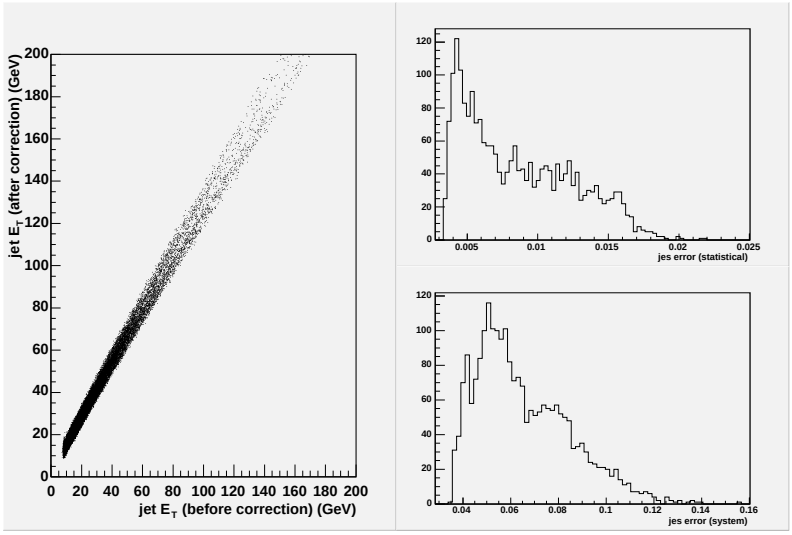

Figure 6.1. Jet E_T (Data) before and after JES correction (left), as well as the associated statistical (upper right) and systematic (lower right) errors.

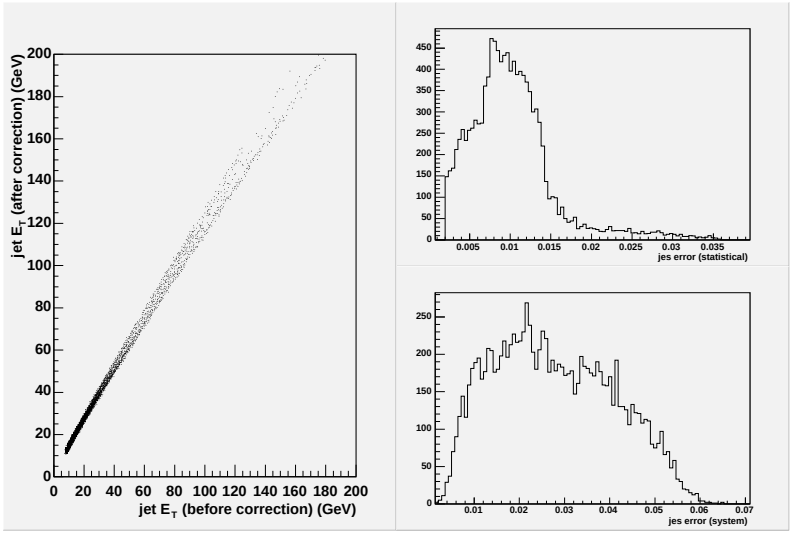

Figure 6.2. Jet E_T (Monte Carlo) before and after JES correction (left), as well as the associated statistical (upper right) and systematic (lower right) errors.

CHAPTER 7

THE SEARCH FOR SECOND GENERATION LEPTOQUARKS IN THE $\mu\mu jj$ CHANNEL

As introduced in Chapter 2, leptoquarks would mainly be produced in pairs at the Fermilab Tevatron collider. Assuming the branching fraction for a leptoquark decaying into a highly energetic muon and a highly energetic jet is $\beta = Br(LQ_2 \rightarrow \mu j) = 100\%$, this chapter describes the search for the scalar second generation leptoquarks in the $\mu j + \mu j$ final state based on an integrated luminosity of 370 pb^{-1} collected by Run II DØ detector between September 2002 and August 2004.

7.1 Data Sample

The raw data events recorded by DØ data acquisition system are converted into physics objects via DØ event reconstruction process ($D0Reco$) and are further skimmed by Common Sample Group (CSG) into different samples according to different physics requirements. For the decay of a pair of scalar second generation leptoquarks into charged leptons and jets, the event selection requires the evidence of a pair of oppositely charged, highly energetic muons and two highly energetic jets; thus the $2MUhighpt$ [59] skim is used for searching scalar second generation leptoquarks, while all the efficiencies are derived from $1MUloose$ skim to prevent introducing bias. The $2MUhighpt$ skim requires at least 2 *loose* muons with transverse momentum, measured by the central tracking system, greater than 15 GeV,

while the criteria of $1MUloose$ [59] skim are at least 1 *loose* muon with transverse momentum greater than 8 GeV.

7.1.1 Data Quality Selection

Of the data delivered by the Tevatron, only a fraction is recorded by the DØ detector. Out of this data only the fraction for which all detector systems are functioning well is considered for the data analysis. Finally, only the fraction of data which is reconstructed by the reconstruction software package ($D0Reco$) is actually used for the data analysis presented.

The data quality monitoring is performed on two levels, online and offline. It is crucial for a high data-taking efficiency to catch the malfunction of detector components, of the readout or the triggering electronics as early as possible. Online data quality monitoring guarantees immediate reaction and thus maximizes the online data quality.

However, there are data quality issues which cannot be recognized online. The remaining deficient data is eliminated by offline data quality monitoring. The idea is to compare basic distribution of physics objects or other variables that describe the detector performance of the data taken with canonical distributions. In a second step a list of possible data corruption methods is identified, quality measures are defined with a maximum discrimination power between usable and unusable data, and criteria are defined to classify the data quality.

The data quality selection is broken down into run based. The good run selection is based on the information stored in DØ's Run Quality Database [60]. In this analysis, to guarantee that no hardware fails, the run qualities are required to be of "*not bad*" and "*not special*" quality for SMT, CFT, calorimeter and muon subsystems. If a run is reconstructed more than one time, only the latest reconstruction

version is used. Moreover, if some events are reconstructed more than once, only consider the most recently reconstructed to avoid any duplications.

7.1.2 Integrated Luminosity

Similar to the run quality selection, in integrated luminosity calculation, the runs are also required to be of "*not bad*" and "*not special*" quality for SMT, CFT, calorimeter and muon sub-systems. Since some triggers may not exist or be prescaled in a specific trigger list version, the runs are broken down into sub-groups according to trigger list version, the integrated luminosity of each sub-group is calculated separately by using un-prescaled trigger(s), then the integraged luminosities of each sub-group are combine together to give out total integrated luminosity. This analysis is based on the data collected between September 2002 and August 2004 with an integrated luminosity of 370 pb^{-1} excluding "*bad*" and "*special*" SMT, CFT, calorimeter and muon runs.

7.2 Monte Carlo Simulation

The study of the signature of the signal and background processes, the optimization of the event selection, as well as the accurate measurement of selection efficiencies require the Monte Carlo simulation of data events.

7.2.1 Backgrounds

The dominant backgrounds in the search for the scalar second generation leptoquarks in the dimuon channel are Drell-Yan $Z/\gamma^* + jets \rightarrow \mu\mu + jets$ processes. In addition, small contributions come from $W^+W^- + jets \rightarrow \mu\nu\mu\nu + jets$ and top quark production $t\bar{t} + jets \rightarrow W^+W^- + jets \rightarrow \mu\nu\mu\nu + jets$.

7.2.2 Signal

Leptoquark signal simulations are used to compare leptoquark theory to experimental results, and to extract leptoquark mass limit. Leptoquark signal samples of 9 mass points are used in this analysis, starting from 140 GeV to 300 GeV with steps of 20 GeV.

7.2.3 Monte Carlo Samples

In order to compare the recorded data with simulated events, Monte Carlo samples for both signal and background are produced with the PYTHIA event generator. CTEQ5L [61] has been used as the leading-order parton density function (PDF) for both background and signal samples. Table 7.1 shows all the Monte Carlo samples used in this analysis. The signal samples consists of the scalar leptoquark pair production in $p\bar{p}$ collisiona at the Fermilab Tevatron collider. The ALPGEN samples are used for the estimation of the systematic errors only. The cross sections shown at the table are the leading order cross sections from PYTHIA. However, in this analysis, the cross sections for the signal samples are not the cross sections calculated by PYTHIA, but calculated with a tool provided by Krämer, et al. based on the latest CTEQ6.1, and the mass-dependent cross sections for Drell-Yan Monte Carlo samples are defined by:

$$\sigma_{NNLO}\left(M_{Z/\gamma^*}\right) = \sigma_{LO}^{CTEQ5L} \cdot k_{NNLO}^{CTEQ5M}\left(M_{Z/\gamma^*}\right) \cdot \frac{\sigma_{NNLO}^{CTEQ6.1M}}{\sigma_{NNLO}^{CTEQ5M}}, \tag{7.1}$$

where σ_{LO}^{CTEQ5L} is the leading order cross section from PYTHIA Drell-Yan Monte Carlo samples, k_{NNLO}^{CTEQ5M} is the mass dependent k factor, σ_{NNLO}^{CTEQ5M} and $\sigma_{NNLO}^{CTEQ6.1M}$ are NNLO cross section at Z resonance for PDF CTEQ5M and CTEQ6.1M respectively [62]. All the simulated events are passed through a full GEANT simulation of the DØ detector and then reconstructed like the data.

Table 7.1

Monte Carlo samples

Process	Mass (GeV)	Generator	$\sigma \times$BR (pb)	Gen.Evts
$Z/\gamma^* \to \mu\mu + (\text{jets})$	$2 < M_{Z/\gamma^*} < 15$	PYTHIA	194×10^2	20000
$Z/\gamma^* \to \mu\mu + (\text{jets})$	$15 < M_{Z/\gamma^*} < 60$	PYTHIA	327	19250
$Z/\gamma^* \to \mu\mu + (\text{jets})$	$60 < M_{Z/\gamma^*} < 130$	PYTHIA	182	460000
$Z/\gamma^* \to \mu\mu + (\text{jets})$	$130 < M_{Z/\gamma^*} < 250$	PYTHIA	1.37	10000
$Z/\gamma^* \to \mu\mu + (\text{jets})$	$250 < M_{Z/\gamma^*} < 500$	PYTHIA	0.115	18500
$Z/\gamma^* \to \mu\mu + (\text{jets})$	$M_{Z/\gamma^*} > 500$	PYTHIA	0.00462	9500
$Z/\gamma^* + j \to \mu\mu + j$	$60 < M_{Z/\gamma^*} < 130$	ALPGEN		148000
$Z/\gamma^* + jj \to \mu\mu + jj$	$60 < M_{Z/\gamma^*} < 130$	ALPGEN		142000
$t\bar{t} \to \mu\nu\mu\nu + (\text{jets})$	$M_{top} = 175$	PYTHIA	0.0678	22000
$WW \to \mu\nu\mu\nu + (\text{jets})$		PYTHIA	0.0947	20750
$LQ_2\overline{LQ}_2 \to \mu j \mu j$	$M_{LQ_2} = 140$	PYTHIA	1.69	8500
$LQ_2\overline{LQ}_2 \to \mu j \mu j$	$M_{LQ_2} = 160$	PYTHIA	0.797	6750
$LQ_2\overline{LQ}_2 \to \mu j \mu j$	$M_{LQ_2} = 180$	PYTHIA	0.400	7750
$LQ_2\overline{LQ}_2 \to \mu j \mu j$	$M_{LQ_2} = 200$	PYTHIA	0.211	8000
$LQ_2\overline{LQ}_2 \to \mu j \mu j$	$M_{LQ_2} = 220$	PYTHIA	0.114	7250
$LQ_2\overline{LQ}_2 \to \mu j \mu j$	$M_{LQ_2} = 240$	PYTHIA	0.0630	8250
$LQ_2\overline{LQ}_2 \to \mu j \mu j$	$M_{LQ_2} = 260$	PYTHIA	0.0352	8500
$LQ_2\overline{LQ}_2 \to \mu j \mu j$	$M_{LQ_2} = 280$	PYTHIA	0.0199	10000
$LQ_2\overline{LQ}_2 \to \mu j \mu j$	$M_{LQ_2} = 300$	PYTHIA	0.0113	10000

To correct the worse muon momentum resolution observed in data as compared to that of simulated events, the muon transverse momentum for Monte Carlo samples is smeared with a resolution function:

$$\sigma_{smear}\left(\frac{1}{p}\right) = \frac{\sqrt{\left(S\sqrt{\cosh(\eta)}\right)^2 + (Cp)^2}}{p} \text{ [63]}, \tag{7.2}$$

where S and C are Gaussian random distribution with their mean at zero. S accounts for multiple scattering, while C accounts for the overestimated position resolution of the tracking system. The hyperbolic cosine term accounts for more

material the muon must pass through at higher η. For an ideal DØ detector the widths of terms S and C should have values of 0.0136 and 0.00162, but in reality these factors need to be adjusted to account for the materials in the tracking system, as well as the misalignments that exist in the real detector as opposed to the ideal simulation.

By comparing dimuon mass spectra from data and PYTHIA Drell-Yan Monte Carlo samples between Z-mass window 70 GeV and 110 GeV, the parameters in the Monte Carlo muon transverse momentum smearing turns out to be σ_S=0.01458, σ_C = 0.002572, and the final transverse momentum of muons in the Monte Carlo samples is illustrated as:

$$p_T(final) = F_{scale} \times p_T(smeared) \tag{7.3}$$

where the scale factor F_{scale}=0.9936, and the systemic uncertainty related to the muon transverse momentum smearing can be obtained by varying the smear factor by $\pm\sigma$.

As expected, the PYTHIA Drell-Yan Z/γ^* process underestimates the jet multiplicity observed in data due to modeling simulation; it is necessary to apply a correction of the jet multiplicity in Drell-Yan simulated events generated by PYTHIA so that their jet multiplicity reflects that measured in data. This can be done by weighting Drell-Yan $Z \rightarrow \mu\mu$ events with a scaling factor of $(1.136 \pm 0.013)^{N_{jet25}}$ so that their jet multiplicity reflects that measured in data for dimuon events within Z mass window between 60 GeV and 125 GeV, where N_{jet25} is the number of jet with $E_T > 25$ GeV in the dimuon events. The scaling factor was determined from the ratios of the exponential fit to the jet multiplicity of data and Drell-Yan Monte Carlo sample. The corresponding systematic uncertainty associated with the weighting of PYTHIA Drell-Yan background events is determined by the comparison with the

difference of the number of predicted background events from the weighted PYTHIA Drell-Yan samples and that from the ALPGEN $Z + jj$ samples after the final cut. Figure 7.1 shows the dimuon invariant mass and jet multiplicity of data as well as Drell-Yan Monte Carlo samples before and after correction. The ALPGEN $Z + j(j)$ samples are normalized to the same entries as the weighted PYTHIA Drell-Yan samples at $N_{jet} \geq 1(2)$.

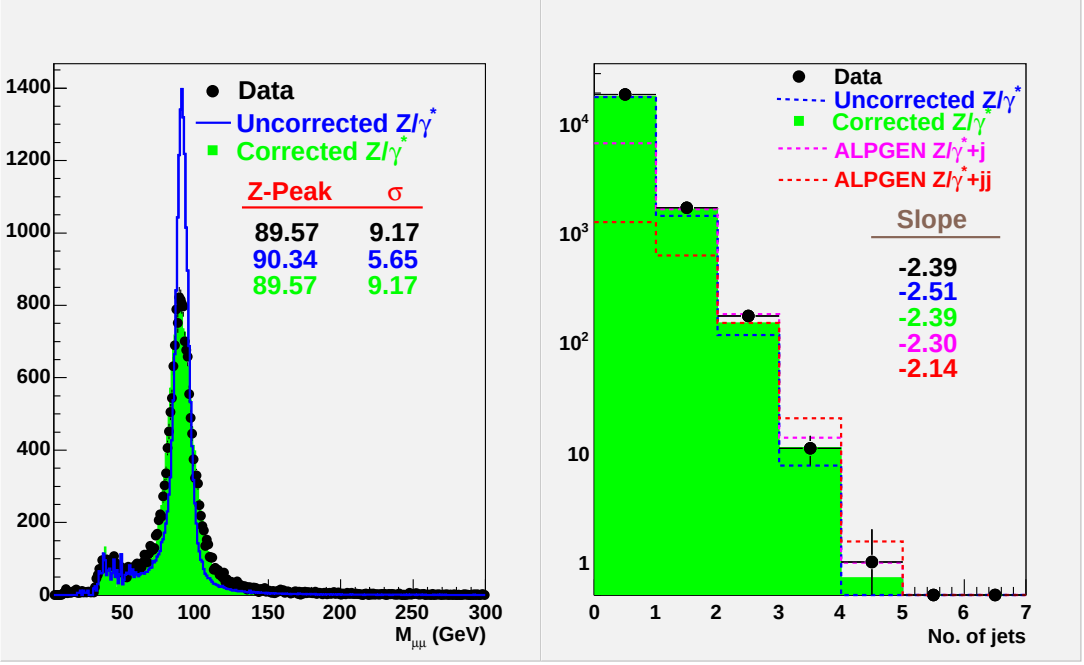

Figure 7.1. MC sample correction: Dimuon mass (left) and jet multiplicity (right).

7.3 Luminosity and Monte Carlo Normalization

After removing runs designated as of "*bad*" or "*special*" quality by Muon, Jet, SMT and CFT subdetectors, the integrated luminosity, which is measured by the DØ luminosity system, is 370 ± 24 pb^{-1}. The normalization of Monte Carlo samples to data has been done using two approaches. The first one is called $Z-window$ normalization, which is done by fitting dimuon mass spectra of the weighted Drell-Yan

Z/γ^* samples to that of data; the other approach, which is called *Luminosity* normalization, is determined by the integrated luminosity measured by the luminosity system and the different efficiencies between Monte Carlo samples and data. In this analysis, both approaches are used to achieve the final results.

7.3.1 Trigger and Reconstruction Efficiencies

The data samples used in this analysis are $2MUhighpt$ data samples skimmed by the Common Sample Group (CSG). However, to prevent introducing bias, all efficiencies described below were obtained from a clean set of $Z \rightarrow \mu\mu$ events selected from $1MUloose$ data samples. Due to the gap in muon system at the bottom region, where the muons have a low detection efficiency, muons falling into the bottom gap, which is defined to be $4.25 < \phi < 5.15$, are not considered in the efficiency study. The event selection requires evidence that a pair of high p_T muons with opposite charge is produced. Both muons are required to lie within a nominal geometrical acceptance of the muon chamber that is defined to be $|\eta| < 1.8$. To reduce the background from cosmic ray muons traversing the detector, cuts are made on the times measured by the muon scintillators and on the *dca* of the muon tracks, where *dca* is the distance of the closest approach of the muon track to the beam spot position in the $r-\phi$ plane. The transverse momentum of both muons, either measured by central tracking or local muon system, must be greater than 15 GeV. The invariant mass of the muon pair is required to be in the vicinity of the Z resonance, i.e., 70 GeV$< M_{\mu\mu} <$110 GeV. The errors on the efficiencies presented in this section are the *binomial* errors from the statistical uncertainties only; systematic errors on the efficiencies have not been estimated. The statistical errors are determined assuming *binomial* statistics

following the formula

$$\sigma_{efficiency} = \sqrt{\frac{\epsilon\,(1-\epsilon)}{N_{tot}}} \tag{7.4}$$

where ϵ is the efficiency and N_{tot} is the total number of $Z \rightarrow \mu\mu$ events selected from $1MUloose$ data samples.

7.3.1.1 Trigger Efficiency

In this analysis, the selected events are required to pass at least one of the following single-muon or di-muon triggers: MU_A_L2M3_TRK10, MUW_W_L2M3_TRK10, 2MU_A_L2M0, 2MU_A_L2ETAPHI, and 2MU_A_L2M0_L3L6. The first two triggers are single-muon triggers with the restriction to the "all muon/wide region" based on muon scintillator only at level 1 and the additional requirement of a medium muon with a minimum transverse momentum of 3 GeV at level 2. At the third trigger level, these two triggers require additional track in the central tracker with the momentum greater than 10 GeV. The dimuon triggers are restricted to the "all muon region" and are based on muon scintillator only at level 1. At level 2, at least one medium muon is required. 2MU_A_L2ETAPHI requires an additional muon of at least loose quality and that the two muons must be separated by at least 0.15 in η and 13.5° in ϕ. 2MU_A_L2M0_L3L6 requires at least one muon with transverse momentum greater than 6 GeV at the third trigger level [64].

A clean set of $Z \rightarrow \mu\mu$ events was selected from $1MUloose$ data sample skimmed by Common Sample Group with the requirement of at least one of the EM or JT triggers being fired. The tagging triggers used are those having names begin with 'E1_' to 'E9_' or 'EM_' or 'JT_'. Both muons are required to be of at least loose quality with an associated central track, and must be isolated in both the calorimeter and central detector. The overall trigger efficiency is obtained from the events

passing any of the five triggers listed above divided by total $Z \rightarrow \mu\mu$ events passed tagging triggers,

$$\epsilon_{trigger} = \frac{N(\mu \; or \; \mu\mu \; triggers)}{N(Z \rightarrow \mu\mu)} = (90.7 \pm 1.7)\% \tag{7.5}$$

7.3.1.2 Loose Muon Efficiency

$Z \rightarrow \mu\mu$ events selected from $1MUloose$ data sample skimmed by Common Sample Group were required to fire at least one of the single-muon triggers. Both muons are required to be isolated in both calorimeter and central detector. The "control" muon, which must be of at least medium quality with an associated central track, is required to have transverse momentum greater than 30 GeV, while the "test" muon is required to have an associated central track, and must be identified by a minimum ionizing particle (MIP) in the calorimeter, and the two muons must be separated by $\Delta\phi > 2.5$. The loose muon efficiency is then defined as the ratio of the number of events for which the "test" muon has also been identified in the muon system with at least loose quality:

$$\epsilon_{loose}^{Data} = \frac{N(test \; \mu \; with \; loose \; quality)}{N(test \; \mu)} = (88.3 \pm 0.7)\%, \; \epsilon_{loose}^{MC} = (89.8 \pm 0.2)\% \tag{7.6}$$

7.3.1.3 Tracking Efficiency

$Z \rightarrow \mu\mu$ events were required to fire at least one of the single or dimuon triggers. The requirement of the "control" muon is the same as that in the calculation of loose muon efficiency. The "test" muon is required to be of at least loose quality in the muon system, and the two muons must be separated by $\Delta\phi > 2.5$. The tracking efficiency is determined from the ratio of the number of events where the "test"

muon also has a central matched track to the total number of $Z \rightarrow \mu\mu$ events:

$$\epsilon_{track}^{Data} = \frac{N(test\ \mu\ with\ central\ track)}{N(test\ \mu)} = (95.9 \pm 0.2)\%,\ \epsilon_{track}^{MC} = (98.0 \pm 0.1)\% \quad (7.7)$$

7.3.1.4 Isolation Efficiency

The requirements of $Z \rightarrow \mu\mu$ events and the "control" muon are the same as that for tracking efficiency. The "test" muon is required to be of at least loose quality and has an associated central track, then is tested to fulfill the isolation criteria [65]:

$$\epsilon_{isolation}^{Data} = \frac{N(test\ \mu\ isolated)}{N(test\ \mu)} = (82.1 \pm 0.3)\%,\ \epsilon_{isolation}^{MC} = (88.5 \pm 0.1)\% \quad (7.8)$$

7.3.1.5 Efficiency Correction for Monte Carlo Samples

The data and the simulated events are reconstructed in the same way; however, the reconstruction efficiencies are different between them. Figure 7.2 shows the muon efficiencies with respect to η and ϕ for data (black dots) and Monte carlo (green lines). The correction factor applied to the Monte Carlo events can be defined as:

$$\epsilon_{Corr}^{MC} = \epsilon_{trigger} \cdot \left(\frac{\epsilon_{loose}^{Data}}{\epsilon_{loose}^{MC}}\right)^2 \cdot \left(\frac{\epsilon_{track}^{Data}}{\epsilon_{track}^{MC}}\right)^2 \cdot \left(\frac{\epsilon_{isolation}^{Data}}{\epsilon_{isolation}^{MC}}\right)^2 = 0.72 \pm 0.02 \quad (7.9)$$

7.3.2 $Z - window$ normalization

The integrated luminosity measured by DØ luminosity system is 370 ± 24 pb^{-1}. Since this analysis depends only on the product of the lumiosity, NLO cross section, acceptance and data selection efficiencies, a technique of *effective luminosity* can be used to normalize Monte Carlo samples to the data. In contrast to early reconstruction versions (p13 or earlier) which have larger systematic error on luminosity

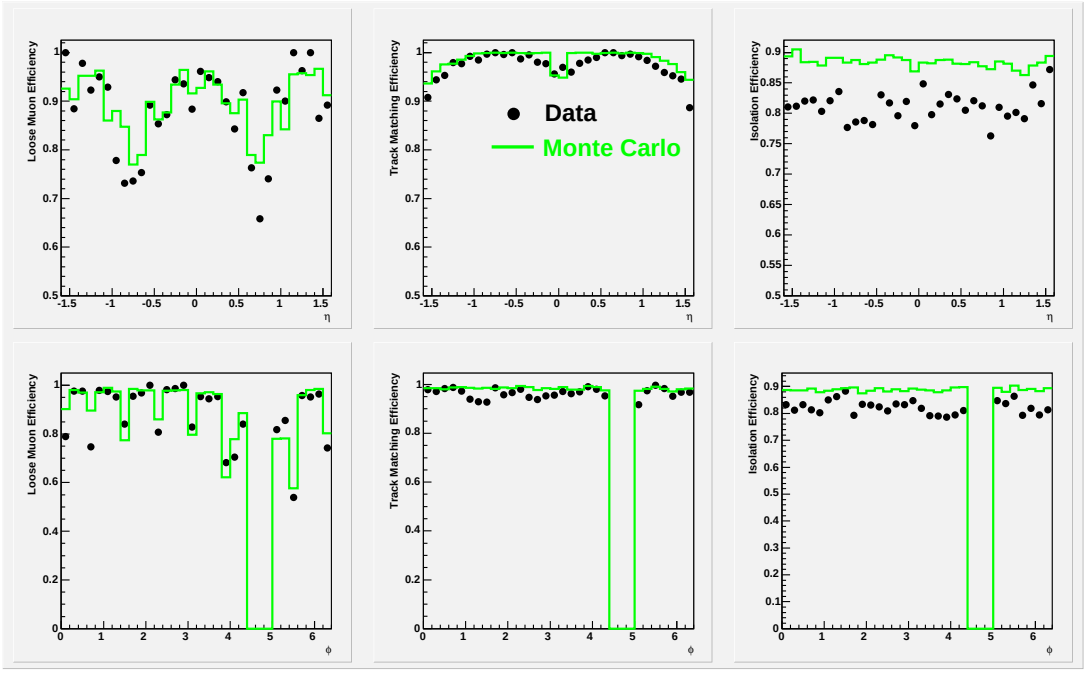

Figure 7.2. Muon efficiencies with respect to η and ϕ for data (black dots) and Monte carlo (green lines).

measurement, this technique gives a smaller systematic error for the normalization factor than would be attained by adding in quadrature the errors from the luminosity system and all the efficiencies separately.

7.3.2.1 Effective Luminosity [66]

The Standard Model background, which is dominated by Drell-Yan Z/γ^* process, is normalized to the data to the same area in the dimuon mass spectra between 70 GeV and 110 GeV. The criteria of dimuon event selection are described in the following section. The corresponding systematic uncertainty is obtained by comparing the results when varying the normalization window by ± 5 GeV. Then the effective

luminosity becomes:

$$\tilde{L} = \frac{N_{Z/\gamma^*}^{generated} \cdot F_{Z/\gamma^*}}{\sigma_{Z\to\mu\mu}} = (275 \pm 16)\ \text{pb}^{-1} \tag{7.10}$$

where $N_{Z/\gamma^*}^{generated}$ is the total number of generated Drell-Yan Monte Carlo events, F_{Z/γ^*} is the normalization factor, $\sigma_{Z\to\mu\mu} = 241.6^{+3.6\%}_{-3.2\%}$ pb [67] is the cross section of $Z \to \mu\mu$. Then the integrated luminosity can be derived by:

$$L = \frac{\tilde{L}}{\epsilon_{Corr}^{MC}} = (381 \pm 24)\ \text{pb}^{-1} \tag{7.11}$$

consistent with the integrated luminosity $[(370 \pm 24)\ \text{pb}^{-1}]$ measured with the luminosity system.

7.3.2.2 Uncertainties in the Effective Luminosity

The uncertainties contributing to the effective luminosity arise from statistical errors, theoretical uncertainty in $Z \to \mu\mu$ cross section [67], muon efficiencies and momentum smearing, additional background from QCD and fake muons [68], and the choice of dimuon mass window.

- Statistical error, which is 0.7%, is determined from the square root of the number of data events in the normalization window.
- Theoretical uncertainty of $Z \to \mu\mu$ cross section contributes 3.6%.
- The error from muon efficiencies, defined in section 7.3.1.5, is 2.6%.
- The error contributed by muon momentum smearing is 1.8%, determined by varying the smearing factor by $\pm\sigma$.
- The uncertainty coming from the choice of normalization window, 2.6%, is obtained by varying the normalization window interval by ±5GeV.

- The contribution of QCD and fake muons was estimated to be less than 2%.

Adding above errors in quadrature, the overall error on effective luminosity turns out to be 5.8%.

7.3.3 *Luminosity* normalization

The *Luminosity* normalization uses the integrated luminosity measured by the luminosity system and the different efficiencies between data and Drell-Yan Monte Carlo samples determined in section 7.3.1.5 to derive the normalization factor. The uncertainly of the normalization factor is obtained by adding individual error sources in quadrature, and the normalization factor will be applied to all Monte Carlo samples.

7.4 Event Selection

A scalar second generation leptoquark pair is expected to decay into two highly energetic muons and two highly energetic jets; thus the event selection requires evidence of a pair of oppositely charged, highly energetic muons and two highly energetic jets. Muon and jet reconstructions have already been described in previous chapters; this section will describe the event selection.

7.4.1 Muon Selection

Muons are identified by the muon system. In order to ensure at least moderate trigger and reconstruction efficiencies, the muons, reconstructed from hits in the scintillator counters and the proportional drift tubes, are required to lie within a nominal geometrical acceptance of the muon chamber that is defined to be $|\eta| < 1.8$. In addition, muons are required to be at least of loose quality with an associated central track, which is required with at least 9 hits in the central fiber tracker.

Tracks with "axial only" information are not taken into account. Isolation cuts are applied to reject background from muons originating mainly from semi-leptotonic decays. To reduce the background from cosmic ray muons traversing the detector, cuts are made on the times measured by the muon scintillators and on the *dca* of the muon tracks, where *dca* is the distance of the closest approach of the muon track to the beam spot position in the $r-\phi$ plane [69].

- Two muons of at least loose quality are required with opposite charge.
- To reduce cosmic ray muons, require $|\Delta t| < 13$ ns and $dca < 0.16$ cm for both muon tracks, where Δt is the difference between the times measured by muon scintillator counters, and *dca* is the distance of the closest approach of the muon track to the beam spot position in the $r-\phi$ plane.
- Both muons are required to lie within the geometrical acceptance of the muon chamber as defined in section 7.3.1, i.e., $|\eta| < 1.8$.
- Muons are required to be isolated in both the calorimeter and central detector, satisfying the standard isolation criteria:

  1. $\Sigma_{cone0.5}(p_T) < 2.5$ GeV, where $\Sigma_{cone0.5}(p_T)$ is the sum of p_T of tracks contained in a cone around the muon of width $R=\sqrt{(\Delta\eta)^2+(\Delta\phi)^2}=0.5$.
  2. $\Sigma_{halo}(E_T) = \Sigma_{cone0.4}(E_T) - \Sigma_{cone0.1}(E_T) < 2.5$ GeV, where $\Sigma_{cone0.1}(E_T)$ and $\Sigma_{cone0.4}(E_T)$ are sums of the E_T of calorimeter clusters in cones around the muon of widths $\Delta R<0.1$ and $\Delta R<0.4$, respectively. In forming these sums, cells in the electromagnetic and fine hadronic calorimeter are considered, but not those in the coarse hadronic calorimeter.

- $p_T > 15$ GeV for both muons, where p_T is the momentum of the matched central detector track measured in the plane transverse to the $p\bar{p}$ beam direction.

- To further reduce background from QCD processes and fake muons, the dimuon invariant mass $M_{\mu\mu} > 60$ GeV is required.

7.4.2 Jet Selection

Calorimeter jets are reconstructed from the energy deposited in the calorimeter cells. In this analysis, jets with a cone size of $R = \sqrt{(\Delta\eta)^2 + (\Delta\phi)^2} = 0.5$ are used. All jets are required to meet the quality criteria described in section 6.2. The energies of all jets are corrected with JES accounting for fragmentation energy outside the jet cone, calorimeter noise and underlying event energy within the jet cone. The associated uncertainty is obtained by varying the error of jet energy correction by $\pm\sigma$. The event selection requires at least two 0.5 cone jets with $E_T > 25$ GeV and within $|\eta| < 2.4$, where E_T is the transverse energy of the jet.

7.4.3 Di-Muon + Di-Jet Events

Figure 7.3 shows the $\mu\mu$+j(j) event comparison between data and Monte Carlo samples. Only events with 2 muons with $p_T > 15$ GeV and at least 1 (for upper plots) or 2 (for lower plots) jet(s) with $E_T > 25$ GeV enter the distributions. There are two possibilities to combine the muons with the jets; only the combination with smaller μj mass difference is chosen, and the reconstructed μj mass is the average of the two μj systems. In order to further separate the signal from remaining Standard Model background, a variety of kinematic distributions of the $\mu\mu + jj$ system were studied, such as the dimuon mass $M_{\mu\mu}$, the reconstructed leptoquark mass $M_{\mu j}$, the invariant mass of the $\mu\mu + jj$ system $M_{\mu\mu jj}$ and the scalar sum of the transverse energies of the $\mu\mu + jj$ system S_T. Figure 7.4 shows the distribution of these variables. As it turns out, the highest sensitivity for the cut-based analysis is a combination of the scalar transverse energy sum S_T and the dimuon mass $M_{\mu\mu}$. Thus two additional

cuts on the dimuon mass, $M_{\mu\mu} > 125$ GeV, and on the scalar sum of the transverse energy of the $\mu\mu jj$ system, $S_T > 370$ GeV, have been applied. The choice of the values of these cuts is based on Monte Carlo information only, and is determined by the theory of the Limit Setting Significance [70] which is defined as:

$$M^{95\%CL}_{expected}(C) = \sum_{n=0}^{\infty} P(n,N) \cdot M^{95\%CL}(n,N) \tag{7.12}$$

where $P(n,N)$ is the Poisson probability $P(n,N) = e^{-N}\frac{N^n}{n!}$ denotes the probability of observing n events passing the set of cuts C, and $M^{95\%CL}$ is the 95% confidence level mass limit for the set of cut C assuming n events observed. Figure 7.5 shows the limit sensitivities of dimuon mass and S_T cuts, the optimized values of these two cuts are 125 GeV and 370 GeV, respectively, and the expected leptoquark mass limit is 243 GeV. Note that these two optimized values are not obtained independently; instead they are obtained recursively. Starting from dimuon mass $M_{\mu\mu}$=100 GeV and S_T=300 GeV, increase S_T by 10 GeV until S_T reaches 400 GeV, then repeat the procedure by increase $M_{\mu\mu}$ by 5 GeV until $M_{\mu\mu}$ reaches 150 GeV.

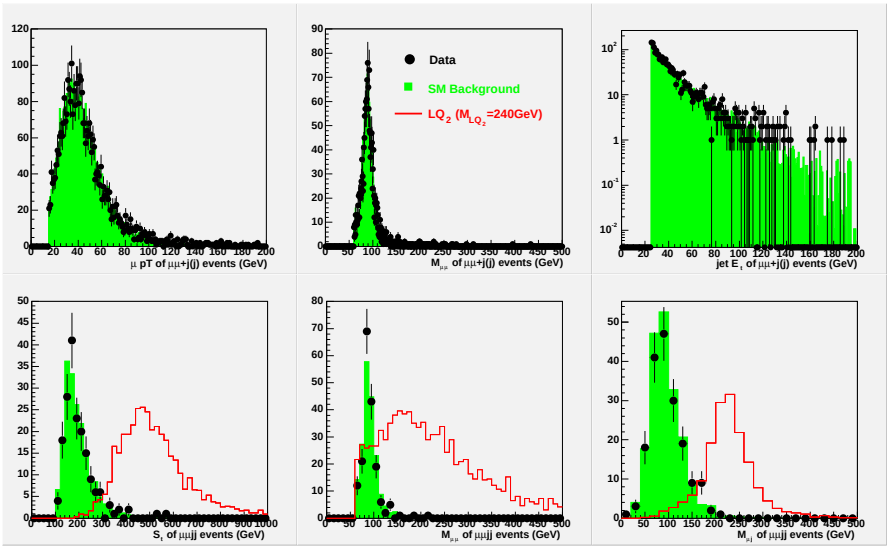

Figure 7.3. $\mu\mu$+j(j) Event comparison between data and Monte Carlo samples.

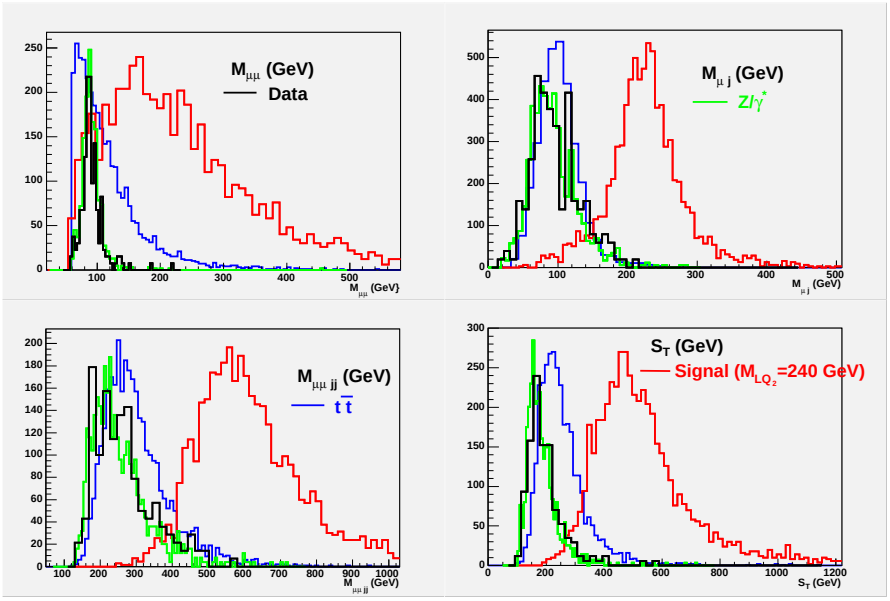

Figure 7.4. Kinematic distributions of the $\mu\mu + jj$ system for data, Standard Model background and signal ($M_{LQ_2} = 240$ GeV).

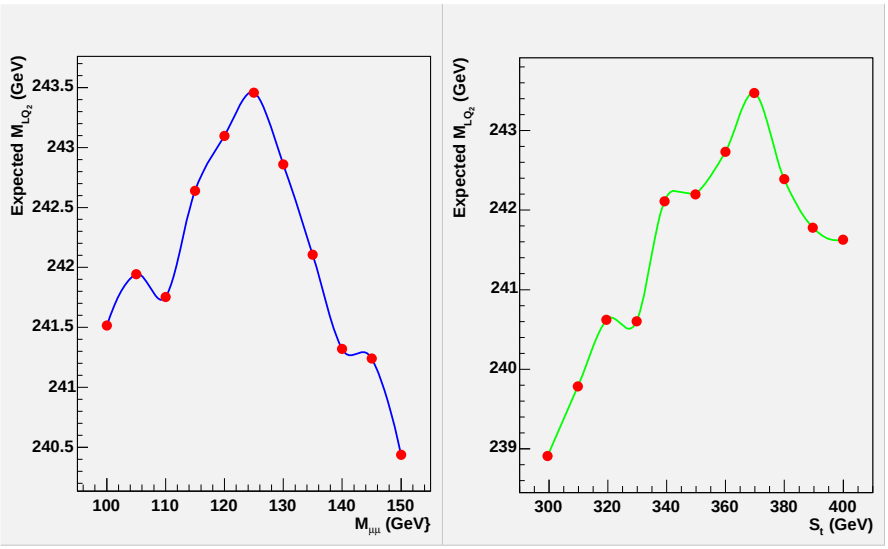

Figure 7.5. Limit sensitivity of $M_{\mu\mu}$ (left) and S_T (right) cut. The optimized values of these two cuts are 125 GeV and 370 GeV, respectively, and the expected leptoquark mass limit is 243 GeV.

7.5 A Neural Network Analysis

In parallel to the cut-based analysis, another approach to optimize the separation of signal and background events was studied. Basde on the preselection of highly energetic $\mu j + \mu j$ events with a dimuon mass greater than 125 GeV, a neural network (NN) [71] is used as a discriminant. The network's output variable reflects a "likelihood" of whether an event is background-like or signal-like.

7.5.1 The Multi-Layer Perceptron

The Multi-Layer Perceptron (MLP) is a simple feed-forward network made of neurons characterized by a bias and weighted links in between. The input neurons receive the inputs and forward them to the first hidden layer. Each neuron in any subsequent layer computes a linear combination of the outputs of the previous layer. The output of the neuron is then a function of that combination with f being linear for output neurons or a sigmoid for hidden layers. Figure 7.6 shows the structure of the MLP.

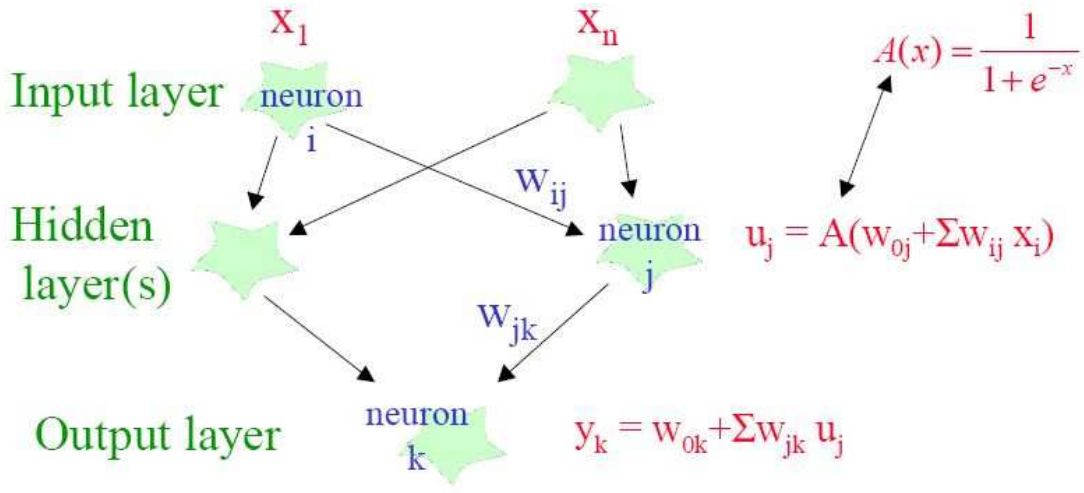

Figure 7.6. A Schematic diagram of the structure of the Multi-Layer Perceptron.

7.5.2 Neural Network Analysis

The input neurons used in this analysis are dimuon mass $M_{\mu\mu}$, scalar sum of transverse momentum of two muons, scalar sum of transverse energy of two jets, scalar sum of transverse energy of the $\mu\mu jj$ system S_T, event mass $M_{\mu j\mu j}$, and relative μj mass difference $\Delta M_{\mu j}/< M_{\mu j} >$. The neural networks contain 1 hidden layer and 6 hidden neurons; the number of training epochs is 100. The training of the neural networks is performed with Monte Carlo events. The sample events in the training of the network are simulated Drell-Yan $Z/\gamma^* + jets$, $WW + jets$, $t\bar{t} + jets$ events, and signal events with a leptoquark mass of $M_{LQ_2} = 240$ GeV, all samples are normalized to the same luminosity, and the Drell-Yan samples are weighted the same way as in the cut-based analysis. In order to enhance the statistics of the training samples, the cut $M_{\mu\mu} > 125$ GeV is not required in the training. Figures 7.7 and 7.8 show the Neural Network outputs for data, Standard Model background and signal.

In the Neural Network analysis, the cut on neural network output NN replaced the S_T cut in cut-based analysis. The optimized neural network output cut NN>0.3 was determined with the same principle as that of S_T cut. Figure 7.9 shows the limit sensitivities of the neural network output cut, and the expected leptoquark mass limit is 251 GeV. Table 7.2 shows the number of remaining events and the associated statistical errors after each cut in the event selection. The number of events in data after each cut is compatible with the expected Standard Model background.

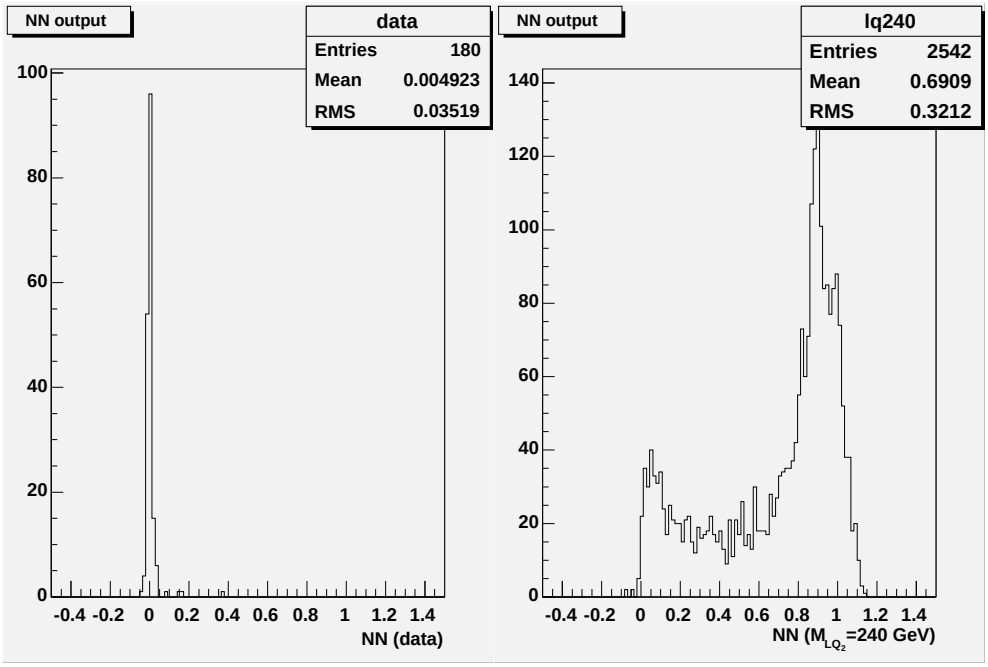

Figure 7.7. The Neural Network output for data and signal (M_{LQ_2} = 240 GeV).

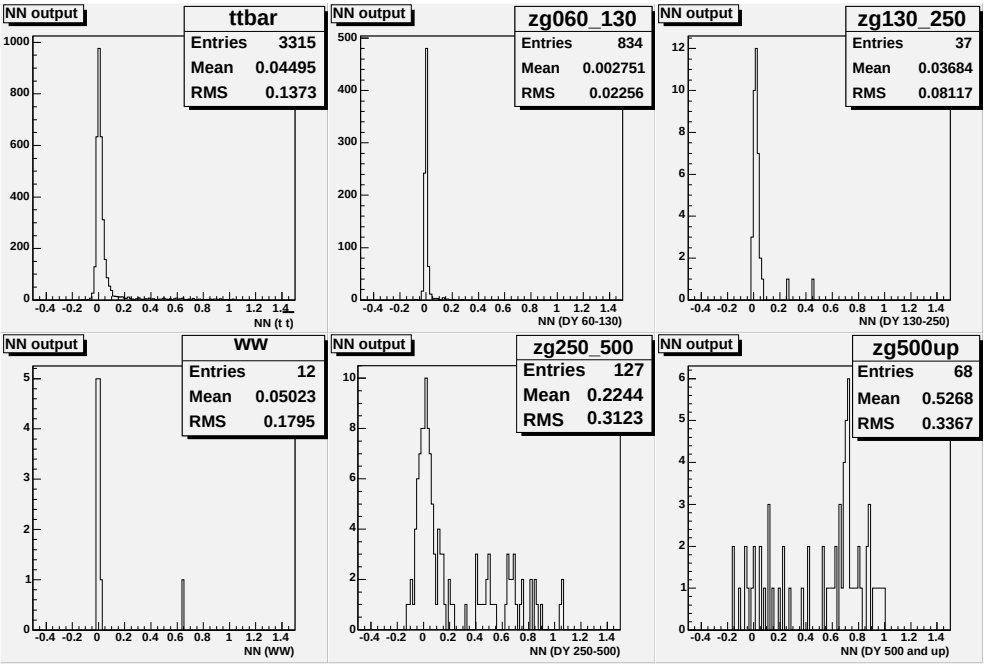

Figure 7.8. The Neural Network output for Standard Model background.

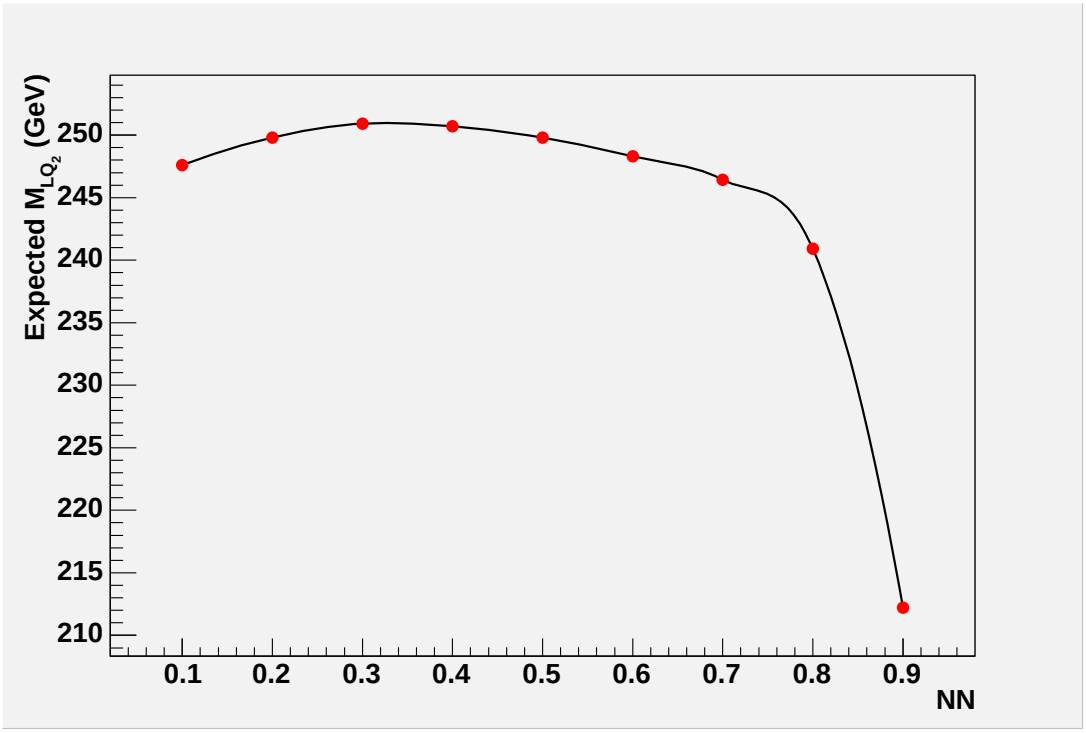

Figure 7.9. Limit Sensitivity of the Neural Network output cut NN. The optimized NN cut is NN>0.3, and the expected leptoquark mass limit is 251 GeV.

Table 7.2. Cut-Flow table of data, Standard Model background and signal (M_{LQ_2} =240 GeV), errors shown are statistical only.

$Z - Window$ Normalization

Cut	Data	Background	DY $Z/\gamma^* \to \mu\mu$	$t\bar{t} \to \mu\nu\mu\nu$	$WW \to \mu\nu\mu\nu$	$M_{LQ_2} = 240$ GeV
$2\mu\,(p_T > 15$ GeV)	21846	20690 ± 54	20674 ± 54	6.74 ± 0.08	8.99 ± 0.11	7.67 ± 0.14
$M_{\mu\mu} > 60$ GeV	19398	18778 ± 52	18768 ± 52	4.88 ± 0.06	5.82 ± 0.08	7.38 ± 0.13
≥ 1 jets ($E_T > 25$ GeV	1764	1749 ± 16	1744 ± 16	4.75 ± 0.06	0.45 ± 0.02	7.35 ± 0.13
≥ 2 jets ($E_T > 25$ GeV	180	162 ± 5	158 ± 5	3.41 ± 0.05	0.02 ± 0.01	6.45 ± 0.12
$M_{\mu\mu} > 125$ GeV	9	5.52 ± 0.89	4.63 ± 0.82	0.89 ± 0.03	0.01 ± 0.01	5.28 ± 0.12
$S_T > 370$ GeV	1	1.14 ± 0.40	0.96 ± 0.37	0.18 ± 0.01	0	4.66 ± 0.11
or						
$NN > 0.3$	0	0.25 ± 0.08	0.15 ± 0.06	0.10 ± 0.01	0	4.47 ± 0.11

Luminosity Normalization

Cut	Data	Background	DY $Z/\gamma^* \to \mu\mu$	$t\bar{t} \to \mu\nu\mu\nu$	$WW \to \mu\nu\mu\nu$	$M_{LQ_2} = 240$ GeV
$2\mu\,(p_T > 15$ GeV)	21846	20118 ± 52	20102 ± 52	6.56 ± 0.07	8.74 ± 0.10	7.46 ± 0.13
$M_{\mu\mu} > 60$ GeV	19398	18259 ± 51	18249 ± 51	4.75 ± 0.06	5.66 ± 0.08	7.17 ± 0.13
≥ 1 jets ($E_T > 25$ GeV	1764	1701 ± 15	1696 ± 15	4.62 ± 0.06	0.44 ± 0.02	7.15 ± 0.13
≥ 2 jets ($E_T > 25$ GeV	180	157 ± 5	154 ± 5	3.32 ± 0.05	0.02 ± 0.01	6.27 ± 0.12
$M_{\mu\mu} > 125$ GeV	9	5.37 ± 0.87	4.50 ± 0.79	0.86 ± 0.03	0.01 ± 0.01	5.13 ± 0.11
$S_T > 370$ GeV	1	1.11 ± 0.39	0.94 ± 0.36	0.17 ± 0.01	0	4.53 ± 0.11
or						
$NN > 0.3$	0	0.24 ± 0.07	0.14 ± 0.06	0.10 ± 0.01	0	4.35 ± 0.11

7.6 Uncertainties on Background and Signal Samples

The uncertainties on background and signal samples consist of statistical uncertainties and systematic uncertainties. The statistical uncertainties are obtained from the full Monte Carlo samples, while the systematic uncertainties will be described below.

7.6.1 Systematic Uncertainties on Backgrounds

The systematic uncertainties on backgrounds include the theoretical uncertainty of $Z \rightarrow \mu\mu$ cross section, luminosity measurement and Monte Carlo normalization, muon and jet identification [72], muon momentum smearing, jet energy scale (JES), and the uncertainty related to the Jet-Et shape of $Z \rightarrow \mu\mu + jets$ Monte Carlo events.

- Monte Carlo statistics: 35.6% (cut based) and 30.0% (NN based).
- Theoretic uncertainty of $Z \rightarrow \mu\mu$ cross section: 3.6%.
- Error on luminosity measurement is about 6.5%, and the uncertainty of Z-window normalization, as described in section 7.3.2.2, is 5.8%.
- Contribution of muon identification, which is 2.6%, has already been derived in section 7.3.1.5, the jet reconstruction uncertainty is about 3% per jet, and the error of muon momentum smearing is 1.8%.
- The jet energy scale error, as described in section 6.3, is 12.5%. Since the jet energy scale is not correlated for data and Monte Carlo events, JES errors of data and Monte Carlo samples were added in quadrature.
- The uncertainty related to the $Jet\ E_T$ shape of $Z \rightarrow \mu\mu + jets$ Monte Carlo events, as described in section 7.2.3, contribute 25.6% to the total error. The

ALPGEN $Z+jj$ Monte Carlo sample has been normalized to the same number of dimuon+dijet events of weighted PYTHIA Drell-Yan samples in the dimuon mass window between 60 GeV and 125 GeV; the difference of the number of expected events after final cut between ALPGEN and weighted PYTHIA Monte Carlo samples is taken as the systematic uncertainty due to the *jet* E_T shape.

Adding all uncertainty sources in quadrature yields 46.1% (cut based), 41.9% (NN based) for $Z-window$ normalization and 46.5% (cut based), 42.4% (NN based) for *Luminosity* normalization.

7.6.2 Systematic Uncertainties on Signal Acceptance

The systematic uncertainties on signal acceptance arise from muon and jet identification, muon momentum smearing, jet energy scale, the uncertainty related to the *Jet* E_T shape of $Z \rightarrow \mu\mu + jets$ Monte Carlo events, and the PDF uncertainty [73]. The PDF uncertainty on the signal efficiency has been studied by varying the dominated error, the error of CTEQ6.1M PDF eigen vector 15, with the signal sample M_{LQ_2} = 240 GeV within $\pm\sigma$. The result turned out to be 1.5%, considering the other errors; this should be multiplied by a factor of 2, and becomes 3.0%. The uncertainties on signal acceptance of $M_{LQ_2} = 240$ GeV are listed below.

- Monte Carlo statistics: 2.3% (cut based), 2.4% (NN based).
- Muon identification: 2.6%.
- Muon momentum smearing: 0.5%.
- Jet reconstruction: 3% per jet.
- Jet energy scale: 0.4%.

- PDF uncertainty: 3.0%.
- Total: 6.3% (for both cut and NN based).

7.7 Limit on the Cross Section of Scalar Leptoquarks

One (cut based)/zero (NN based) event remains from the data after the final cut, the expected background events are 1.1 (cut based)/0.2 (NN based), and the expected signal (M_{LQ_2} =240 GeV) events are about $\sim$4.5, respectively. The number of events in data after the final cut is compatible with the expected Standard Model background. No excess of data over background was found. Assuming a branching ratio $\beta = 100\%$ for the scalar second generation leptoquark decaying into charged leptons, 95% confidence level upper limit on the production cross section σ_{LQ_2} is calculated based on the results shown in the last row of the cut flow table in section 7.4.3 and on the uncertainties discussed in section 7.6. The calculation constructs confidence limits by using the Bayesian technique [74], which is described below.

For a given set of signal cross section σ, the signal efficiency ε, the integrated luminosity $\mathcal{L}$, and the expected background b, the number of expected events k is given by:

$$k = b + \mathcal{L}\varepsilon\sigma, \tag{7.13}$$

the probability density for observing n events for a given set of $\sigma,\ \varepsilon,\ \mathcal{L}$ and b becomes

$$P\left(k|\sigma, \mathcal{L}, \varepsilon, b\right) = \frac{e^{-(b+\mathcal{L}\varepsilon\sigma)} \cdot \left(b + \mathcal{L}\varepsilon\sigma\right)^k}{k}, \tag{7.14}$$

and the specified $100 \times \beta\%$ confidence level upper limit on the cross section σ_{UL} is

defined by:

$$\beta = \int_0^{\sigma_{UL}} d\sigma P\left(k|\sigma, \mathcal{L}, \varepsilon, b\right). \tag{7.15}$$

Including the uncertainty information, the probability density becomes

$$P\left(\sigma|k, I\right) = \frac{P\left(k|\sigma, I\right) \cdot P\left(\sigma|I\right)}{P\left(k|I\right)}, \tag{7.16}$$

where I represents all the information used to build k, the denominator is determined by the normalization condition:

$$\int_0^{\infty} d\sigma P\left(\sigma|k, I\right) = 1 \quad and \quad P(\sigma|I) \rightarrow P(\sigma, \mathcal{L}, \varepsilon, b|I) = P(\sigma|I)P(\mathcal{L}, \varepsilon, b|I). \tag{7.17}$$

Assuming the errors are uncorrelated, $P\left(\mathcal{L}, \varepsilon, b|I\right)$ is factorized as:

$$P\left(\mathcal{L}, \varepsilon, b|I\right) = P\left(\mathcal{L}|I\right) P\left(\varepsilon|I\right) P\left(b|I\right) = G\left(\mathcal{L}, \delta\mathcal{L}\right) G\left(\varepsilon, \delta\varepsilon\right) G\left(b, \delta b\right), \tag{7.18}$$

where $G\left(x, \delta x\right)$ is a Gaussian distribution with mean x and width δx. The Bayesian limit for the cross section with uncertainties is calculated by the integration:

$$P(\sigma|k, I) \propto \int_0^{\infty} d\mathcal{L} \int_0^{1} d\varepsilon \int_0^{\infty} db P(k|\sigma, \mathcal{L}, \varepsilon, b) G(\mathcal{L}, \delta\mathcal{L}) G(\varepsilon, \delta\varepsilon) G(b, \delta b), \tag{7.19}$$

the constant of proportionality is determined by the condition $\int_0^{\infty} d\sigma P\left(\sigma|k, I\right) = 1$. Then the specified $100 \times \beta\%$ confidence level upper limit on the cross section σ_{UL}

becomes:

$$\beta = \int_0^{\sigma_{UL}} d\sigma P\left(\sigma|k, I\right). \tag{7.20}$$

Table 7.3 shows the signal efficiencies and 95% confidence level upper limits on the cross section σ_{UL}. These efficiencies for Z-window normalization are the fraction of events left from the full sample of simulated events after the final cut, the trigger inefficiencies and the differences in the construction efficiencies between data and Monte Carlo samples are not included because they are already accounted in the calculation of the effective luminosity. However, for Luminosity normalization, the signal acceptances are multiplied by the correction factor derived in section 7.3.1.5 to take into account the trigger inefficiencies and the differences in the construction efficiencies between data and Monte Carlo samples. The error band is obtained by varying the renormalization and factorization scale of CTEQ6.1M between $1/2\mathrm{M_{LQ_2}}$ and $2\mathrm{M_{LQ_2}}$, as well as the CTEQ6.1M PDF error, added in quardrature:

$$\mathrm{ErrorBand\,(up)} = \sqrt{\left(\sigma_{1/2\mathrm{M_{LQ_2}}}\,(\mathrm{NLO}) - \sigma_{\mathrm{M_{LQ_2}}}\,(\mathrm{NLO})\right)^2 + (\mathrm{Error_{PDF+}})^2}, \tag{7.21}$$

$$\mathrm{ErrorBand\,(down)} = \sqrt{\left(\sigma_{2\mathrm{M_{LQ_2}}}\,(\mathrm{NLO}) - \sigma_{\mathrm{M_{LQ_2}}}\,(\mathrm{NLO})\right)^2 + (\mathrm{Error_{PDF-}})^2}. \tag{7.22}$$

The parameters input to the limit calculator [75] are listed below:

- Number of data events after the final cut: 1 (cut based)/0 (NN based).
- Number of background after the final cut: 1.14 ± 0.52 (cut based), 0.25 ± 0.10 (NN based) for $Z-window$ normalization, and 1.11 ± 0.52 (cut based), 0.24 ± 0.10 (NN based) for *Luminosity* normalization.

Table 7.3. Signal efficiencies and 95% confidence level upper limit on σ_{LQ_2}. *Z.N.* and *L.N.* denote $Z - Window$ and *Luminosity* normalization.

M_{LQ_2}(GeV)	140	160	180	200	220	240	260	280	300
Accept.(cut Z.N.) (%)	5.8±0.5	9.6±0.7	12.9±0.9	16.9±1.1	18.5±1.2	22.2±1.4	22.8±1.4	20.5±1.3	21.8±1.4
Accept.(NN Z.N.) (%)	4.6±0.4	7.9±0.6	11.2±0.8	15.6±1.0	16.3±1.1	21.3±1.4	22.1±1.4	20.1±1.3	21.3±1.3
Accept.(cut L.N.) (%)	4.2±0.3	6.9±0.5	9.3±0.6	12.2±0.8	13.3±0.9	16.1±1.0	16.5±1.0	14.8±0.9	15.8±1.0
Accept.(NN L.N.) (%)	3.3±0.3	5.7±0.4	8.1±0.6	11.3±0.7	11.8±0.8	15.4±1.0	16.0±1.0	14.5±0.9	15.4±0.9
$\sigma_{NLO}(M_{LQ_2}/2)$	2.63	1.19	0.577	0.293	0.154	0.0832	0.0457	0.0256	0.0144
$\sigma_{NLO}(M_{LQ_2})$	2.38	1.08	0.525	0.268	0.141	0.0762	0.0419	0.0233	0.0131
$\sigma_{NLO}(2M_{LQ_2})$	2.07	0.947	0.460	0.235	0.124	0.0664	0.0364	0.0202	0.0113
Err.Band(up)	2.87	1.30	0.634	0.325	0.171	0.0929	0.0512	0.0287	0.0162
Err.Band(down)	1.93	0.880	0.429	0.219	0.116	0.0624	0.0343	0.0191	0.0106
$\sigma_{95\%C.L.}$(cut Z.N.)	0.267	0.162	0.119	0.0909	0.0834	0.0691	0.0673	0.0748	0.0704
$\sigma_{95\%C.L.}$(NN Z.N.)	0.246	0.142	0.0997	0.0711	0.0681	0.0520	0.0502	0.0553	0.0521
$\sigma_{95\%C.L.}$(cut L.N.)	0.277	0.167	0.123	0.0940	0.0862	0.0715	0.0696	0.0774	0.0729
$\sigma_{95\%C.L.}$(NN L.N.)	0.254	0.146	0.103	0.0732	0.0702	0.0537	0.0517	0.0570	0.0538

- Signal acceptances after the final cut are shown in Table 7.3.

- Effective luminosity (for Z-window normalization: 275 ± 16 pb^{-1}),
  Integrated luminosity (for Luminosity normalization: 370 ± 24 pb^{-1}).

and the resulting limits on the cross section are shown in Table 7.3. For branching ratio $\beta < 1$, the cross section can be obtained by multiplying the cross section for $\beta = 1$ with the factor $1/\beta^2$. Comparing these limits with theoretical calculations of the leptoquark cross section, the lower bound of the scalar second generation leptoquark mass is set to M_{LQ_2}>247 GeV (NN based), 236 GeV (cut based) for $\beta = 1$, and M_{LQ_2}>184 GeV (NN based), 174 GeV (cut based) for $\beta = 1/2$, as shown in the figure 7.10. The mass limit is extracted from the intersection of the lower edge of the NLO cross section error band with the 95% confidence level upper limit on the production cross section of the scalar second generation leptoquark. The NN results shown in the figure are from $Z - Window$ normalization only because the results from *Luminosity* normalization are so close to that from Z-Window normalization.

In contrast to the cut-based analysis, the NN-based analysis reduces the background level significantly while keeping the signal efficiencies at a similar level, thus improving the upper limit cross section and mass limit of leptoquarks.

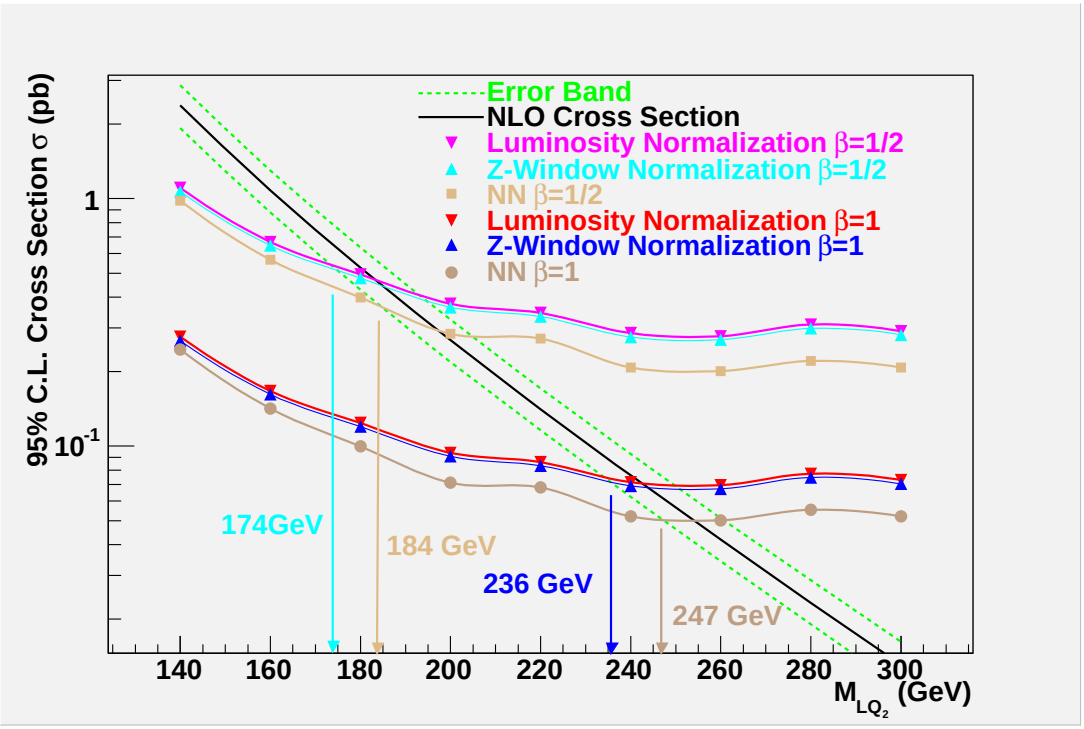

Figure 7.10. 95% cofidence level upper limits on the cross section as a function of the scalar second generation leptoquark mass.

CHAPTER 8

SUMMARY AND CONCLUSION

Althrough the Standard Model has been tested repeatedly and found to be in good agreement with experimental evidence for a variety of processes, it cannot explain the apparent symmetry between lepton and quark sectors of elementary particles. Many theories beyond the Standard Model of elementary particle physics attempt to solve this puzzle by introducing new hypothesized gauge bosons called leptoquarks which carry both lepton and baryon quantum numbers and fractional electric charge. By dividing leptoquarks into three generations and applying constraints on intra-generational interactions, i.e., each generation of leptoquarks only interacting within the same generation of leptons and quarks, the leptoquarks could have masses of the order of hundreds of GeV and make it possible to perform searches with the current experimental facilities.

In a proton-antiproton collider such as the Fermilab Tevatron which operates at a center-of-mass energy of $\sqrt{s} = 1.96$ TeV, leptoquarks would mainly be produced in pairs, and each leptoquark would decay into a highly energetic lepton and a highly energetic quark. For the search for the scalar second generation leptoquark pair which will decay into a pair of charged leptons and a pair of quarks, the evidence of a pair of oppositely charged, highly energetic muons and two highly energetic jets is required. This thesis provides a detailed description and a comprehensive study of the search for the scalar second generation leptoquarks in $\mu j + \mu j$ final state based

on an integrated luminosity of 370 pb^{-1} collected by DØ Run II detector between September 2002 and August 2004.

With the optimized cuts, the number of events in data is compatible with the Standard Model background which is dominated by the Drell-Yan $Z/\gamma^* + \text{jets} \rightarrow \mu\mu + \text{jets}$ process. Backgrounds from other sources such as WW and $t\bar{t}$ are also estimated. No evidence for leptoquark production is found. Based on this consistency of the data with the Standard Model background and estimated signal efficiencies, the 95% confidence level upper limits on the cross section for the scalar second generation leptoquark production σ_{LQ_2} is calculated assuming the branching fraction for a scalar second generation leptoquark decaying into a highly energetic muon and a highly energetic jet is $\beta = Br(LQ_2 \rightarrow \mu j) = 100\%$. These limits have been compared with theoretical cross section of the leptoquark production, and a lower bound to the mass of the scalar second generation leptoquarks of $M_{LQ_2}^{\beta=1} > 247$ GeV (NN based), 236 GeV (cut Based) is extracted. The corresponding mass limit for $\beta = 1/2$ is $M_{LQ_2}^{\beta=1/2} > 184$ GeV (NN based), 174 GeV (cut based), obtained by multiplying the cross section for $\beta = 1$ with the factor $1/\beta^2$.

In contrast to the cut-based analysis, the NN-based analysis reduces the background level significantly while keeping the signal efficiencies at a similar level, thus improving the upper limit cross section and mass limit of leptoquarks.

As an outlook, this study provides efficient tools for the search for the scalar second generation leptoquarks, and can be easily applied to future searches with enhanced integrated luminosity without major modification.

REFERENCES

[1] I. Mendeleev, *Annalen der Chemie und Pharmacie VIII,* Supplementary Volume for 1872.

[2] J. J. Thompson, Philos. Mag. 44, 293 (1897)

[3] E. Rutherford, *The Scattering of the α & β rays and the Structure of the Atom,* Proceedings of the Manchester Literary and Philosophical Society, IV (1911)

[4] G. Kane, *Modern Elementary Particle Physics,* Addison-Wesley (1993);
D. J. Griffiths, *Introduction to Elementary Particles,* New York Wiley (1987)

[5] J. Goldstone, S. Weinberg, Phys. Rev. 127, 965 (1962)

[6] P. W. Higgs, Phys. Rev. Lett. 13, 508 (1964)

[7] UA1 Collaboration, Phys. Lett. B 122, 103 (1983);
UA2 Collaboration, Phys. Lett. B 122, 476 (1983)

[8] DØ Collaboration, Phys. Rev. Lett. 74, 2632 (1995);
CDF Collaboration, Phys. Rev. Lett. 74, 2626 (1995)

[9] G. Ross, *Grand Unified Theories*, Benjamin-Cummings Publishing Co. (1995);
P. D. B. Collins et al., *Particle Physics and Cosmology*, John Wiley & Sons (1989)

[10] J. Wess and J. Bagger, *Supersymmetry and Supergravity*, Princeton University Press (1983);
Y. A. Gol'fand and E. P. Likhtam, JETP Lett. 13, 323 (1971);
D. V. Volkov and V. P. Akulov, Phys. Lett. B 46, 109 (1973);
J. Wess and B. Zumino, Nucl. Phys. B 70, 39 (1974)

[11] M. Kuze and Y. Sirois, *Search for Particles and Forces Beyond the Standard Model at HERA ep and Tevatron $p\bar{p}$ Colliders,* hep-ex/0211048 (2002)

[12] J. C. Pati and A. Salam, Phys. Rev. D 10, 275 (1974);
E. Eichten et al., Phys. Rev. D 34, 1547 (1986);
W. Buchmüller and D. Wyler, Phys. Lett. B 177, 377 (1986);
E. Eichten et al., Phys. Rev. Lett. 50, 811 (1983);
H. Georgi and S. Glashow, Phys. Rev. Lett. 32, 438 (1974)

[13] M. Leurer, Phys. Rev. D 39 333 (1994);
J. L. Hewett and S. Pakvasa, Phys. Rev. D 37, 3165 (1988)

[14] J. C. Pati and A. Salam, Phys. Rev. D 10, 275 (1974)

[15] J. L. Hewett and T. G. Rizzo, Phys. Rept. 183, 193 (1989)

[16] M. M. Boyce, et al., Phys. Rev. D 55, 68 (1977);
M. Drees and A. Yamada, Phys. Rev. D 53, 1586 (1996)

[17] J. L. Hewett and S. Pakvasa, Phys. Rev. D 37, 3165 (1988)

[18] M. Krämer et al., Phys. Rev. Lett. 79, 341 (1997)

[19] M. Leurer, Phys. Rev. Lett. 71, 1324 (1993);
M. Leurer, Phys. Rev. D 39 333 (1994)

[20] DØ Collaboration, Phys. Rev. Lett. 81, 38 (1998);
DØ Collaboration, Phys. Rev. Lett. 84, 2088 (2000);
DØ Collaboration, Phys. Rev. D 64, 092004 (2001);
DØ Collaboration, Phys. Rev. Lett. 88, 191801 (2002)

[21] CDF Collaboration, Phys. Rev. Lett. 79, 4327 (1997);
CDF Collaboration, Phys. Rev. Lett. 85, 2056 (2000)

[22] P. B. Straub, *Minireview of Leptoquark Searches,* hep-ex/0212023(2002)

[23] http://nobelprize.org/physics/laureates/1938/fermi-bio.html

[24] http://www.fnal.gov/pub/about/whatis/history.html

[25] http://www-bd.fnal.gov/runII/index.html

[26] DØ Collaboration, NIM, A338, 185 (1994);
DØ Collaboration, FERMILAB-PUB-96/375-E (1996);
T. LeCompte and H. T. Diehl. Ann. Rev. Nucl. Part. Sci. 50, 71 (2000)

[27] DØ Upgrade Collaboration, DØ note 2169 (1994)

[28] DØ Upgrade Collaboration, DØ note 4164 (1999)

[29] J. Brzenziak et al., DØ note 2167 (1994)

[30] DØ Upgrade Collaboration, DØ note 3014 (1996)

[31] DØ Upgrade Collaboration, DØ note 3445 (1998)

[32] DØ Upgrade Collaboration, DØ note 4240 (2000)

[33] R. Jayanti et al., DØ note 2780 (1996)

[34] T. Diehl et al., DØ note 3365 (1998)

[35] T. Diehl et al., DØ note 3366 (1998)

[36] T. Diehl et al., DØ note 3237 (1997)

[37] B. S. Acharya et al., Nucl. Instr. Meth. A 401, 45 (1997)

[38] V. Abramov et al., Nucl. Instr. Meth. A 419, 660 (1998)

[39] A. Lo et al., DØ note 3320 (1997)

[40] http://www-d0.fnal.gov/computing/algorithms

[41] G. Hesketh, DØ note 4079 (2003)

[42] http://www-d0.fnal.gov/computing/algorithms/muon/muon_algo.html

[43] J. Butler, DØ note 4002 (2002)

[44] S. Hagopian, *The Run II DØ Muon System at the Fermilab Tevatron,* 7th International Conference on Advanced Technology and Particle Physics, Como, Italy (2002)

[45] http://www-d0.fnal.gov/computing/MonteCarlo/MonteCarlo.html

[46] T. Sjostrand et al., Computer Physics Commun. 135 238 (2001)

[47] M. Mangano et al., JHEP 0307 001 (2003)

[48] R. Brun, *GEANT 3 Users Guide,* Technical Report CERN/DD/EE/84-1, CERN (1984)

[49] http://www-d0.fnal.gov/d0dist/dist/packages/muo_hit/devel/doc/

[50] O. Peters, DØ note 3901 (2002)

[51] F. Deliot, *The Fit Algorithm in muo_trackreco,* DØ private documentation (2002)

[52] L. Chevalier et al., *Track Parameter Error Matrix Propagation in Matter and Magnetic Field, Error Matrices Combination,* DØ Preliminary (2001)

[53] http://www-d0.fnal.gov/phys_id/muon_id/d0_private/muonid_dh.html

[54] DØ Muon ID group, DØ note 4350 (2004)

[55] http://www-d0.fnal.gov/d0dist/dist/releases/
http://www-d0.fnal.gov/d0dist/dist/packages/

[56] L. Duflot, DØ note 3749 (2000)

[57] http://www-d0.fnal.gov/phys_id/jets/jetID_p14_pass2.html

[58] http://www-d0.fnal.gov/phys_id/jes/d0_private/certified/certified.html

[59] http://www-d0.fnal.gov/Run2Physics/cs/skimming/pass1.html

[60] http://d0db-prd.fnal.gov/run/runQuery.html

[61] H. L. Lai et al., CTEQ Collaboration, Eur. Phys. J. C 2 375 (2000)

[62] T. Nunnemann, DØ note 4476 (2004)

[63] R. Hooper, G. Landsberg, DØ note 4230 (2003)

[64] DØ trigger group, *DØ Global Trigger List Descriptions,*
http://www-d0.fnal.gov/trigger_meister/private/www/tl_desc/global.html

[65] D. Whiteson, M. Kado, DØ note 4070 (2003)

[66] T. Christiansen, DØ note 4190 (2003)

[67] J. Pumplin et al., JHEP 0207 012 (2002)

[68] E. Nurse, P. Telford, DØ note 4284 (2003)

[69] DØ Muon ID group, *MuoCandidate for p14,*
http://www-d0.fnal.gov/phys_id/muon_id/d0_private/certif/p14/index.html

[70] B. Knuteson, DØ note 3345 (1997)

[71] J. Schwindling et al.,
http://schwind.cern.ch/schwind/MLPfit.html

[72] M. Klute, DØ note 4185 (2003)

[73] T. Christiansen, R. Strähmer, DØ note 4679 (2005)

[74] I. Bertram et al., DØ note 3476 (1999)

[75] J. Hobbs, G. Landsberg,
http://www-d0.fnal.gov/ hobbs/limit_calc.html